Transition from Mach Reflection to Regular Reflection over a Concave Cylindrical Wedge

Peter Wilk

Department of Mechanical Engineering
McGill University
Montreal, Canada

December 2021

Supervised by:
Prof. Evgeny Timofeev

Abstract

When a moving shock wave reflects from a concave cylindrical surface, transition from an Inverse Mach Reflection (InMR) to a Transitioned Regular Reflection (TRR) takes place. The triple point of a Mach Reflection approaches the reflecting surface in a tangential manner, resulting in minute Mach stems and, hence, significant difficulties in the prediction of the transition point location. In the present work, the location of the transition point is found using a high-resolution finite-volume Computational Fluid Dynamics (CFD) solver based on the Euler equations and an approximate Geometrical Shock Dynamics (GSD) finite-difference solver. The GSD model is governed by the relationship between the local geometry (area) of the shock and its local velocity (Mach number). It has previously been shown to provide, in a very efficient manner, accurate estimates of the shock front for various reflections but was not yet applied to analysis of the InMR-to-TRR transition. Thorough grid-convergence studies are performed both for the CFD and GSD solvers. The CFD and GSD results are compared to historical and recent experimental results as well as to various analytical predictions available in the literature.

Sommaire

Lorsqu'une onde de choc en mouvement se réfléchit à partir d'une surface cylindrique concave, la transition d'une réflexion de Mach inverse (InMR) à une réflexion régulière transitionnée (TRR) se déroule. À cause de la trajectoire du point triple, qui s'approche la surface réfléchissante de manière tangentielle, la tige de Mach juste avant transition devient très petite. Par consequence, la prédiction du point de transition devient difficile. Dans ce travail, le point de transition est trouvé à l'aide d'un solveur de Mécanique des fluides numérique (CFD) et par un solveur approximatif de dynamique de choc géométrique (GSD). Le modèle GSD est régi par la relation entre la géométrie locale (l'aire) du choc et sa vitesse locale (nombre de Mach). GSD a déjà été démontré qu'il fournit, de manière très efficace, des estimations précises de l'onde de choc pour plusieurs réflexions, mais n'a pas encore été appliqué à l'analyse de la transition InMR-TRR. Des analyzes de convergences sont effectuées pour le solver CFD et le solver GSD. Les résultats obtenus par CFD et GSD sont comparés avec des résultats expérimentaux et avec des prédictions analytiques disponibles dans la littérature.

Acknowledgments

This work has been made possible thanks to the help of my amazing supervisor, Prof. Evgeny Timofeev. His help and guidance throughout this process have been instrumental in helping me complete this thesis.

I would like to acknowledge my parents for being my inspiration to pursue this thesis and I would like to thank my girlfiriend, Anne-Marie, for her loving support.

Contents

List of Figures

Chapter 1

Introduction

1.1 Shock Wave Definition and Formation

A shock wave is a propagating disturbance with a near instantaneous change in pressure, temperature and density. A shock wave propagates into a medium with supersonic speed $M_s > 1$. Similarly, a sound wave is a propagating disturbance which travels at the local speed of sound $c = \sqrt{\gamma RT}$.

To understand the formation of a shock wave, consider Figure 1.1. An initial sound wave, c_1, is created resulting in a small but instantaneous increase in pressure, temperature and density. This is followed by consecutive sound waves c_2, c_3, etc. Because each sound wave travels at the local speed of sound, based on the medium it is propagating into, each successive sound wave is faster then its predecessor (i.e. $c_3 > c_2 > c_1$) due to the small increase in temperature after each sound wave. The merging of all sound waves results in a shock wave with a finite amplitude. A normal shock wave is shown in Figure 1.2.

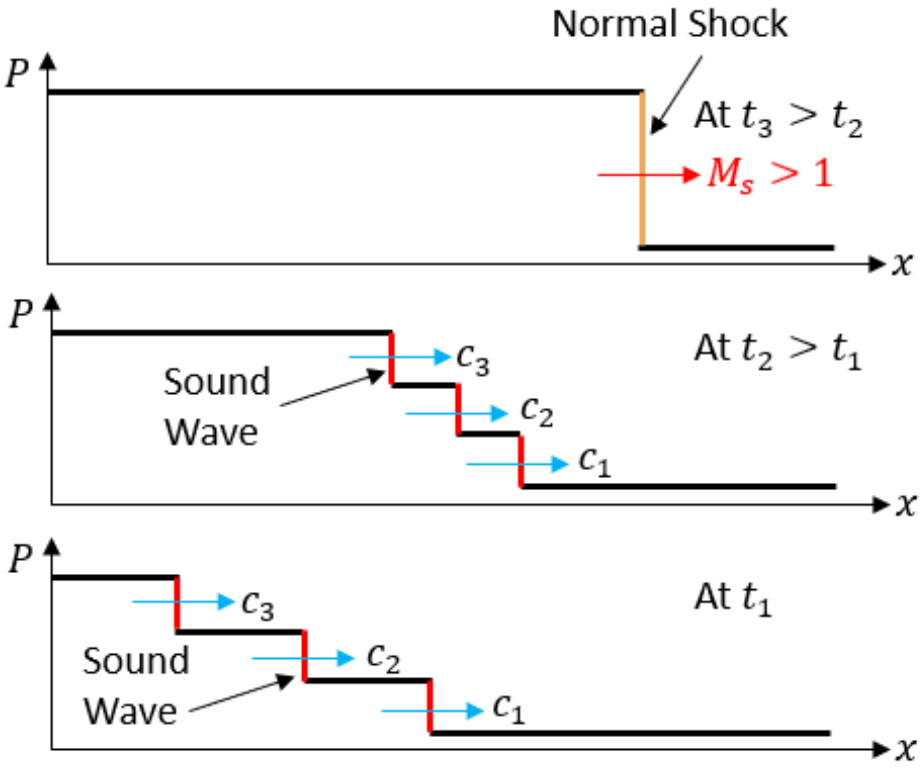

Fig. 1.1 Pressure profile for consecutive sound waves resulting in a shock wave. Reproduced from [1].

1.2 Normal Shock Waves

A normal shock wave propagates at supersonic speed $M_s > 1$. If a normal shock wave propagates into a gas at rest, as seen in Figure 1.2 (Left), then a simple change in the frame of reference, from that of the observer on ground, to that of the shock wave, would result in a resting normal shock wave. This can be seen in Figure 1.2 (Right).

The relations between the flow characteristics between the two states, both ahead and behind the normal shock wave, can be obtained from conservation laws. These relations are known as the Rankine-Hugoniot relations [1], which are the following:

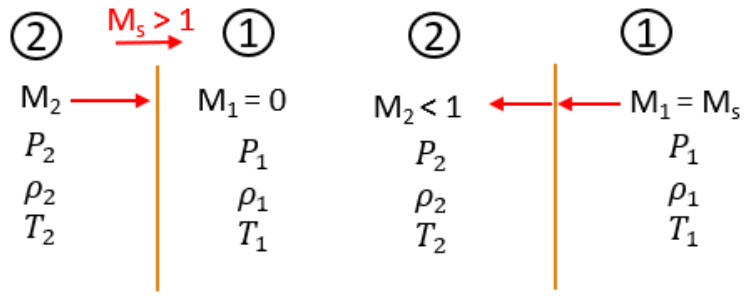

Fig. 1.2 **Left:** Normal Shock Wave in the laboratory frame of reference. **Right:** Normal Shock Wave in the shock frame of reference.

$$M_2^2 = \frac{2 + (\gamma - 1)M_1^2}{2\gamma M_1^2 - (\gamma - 1)} \tag{1.1}$$

$$\frac{p_2}{p_1} = \frac{2\gamma M_1^2 - (\gamma - 1)}{\gamma + 1} \tag{1.2}$$

$$\frac{\rho_2}{\rho_1} = \frac{(\gamma + 1)M_1^2}{(\gamma - 1)M_1^2 + 2} \tag{1.3}$$

$$\frac{T_2}{T_1} = \frac{[2\gamma M_1^2 - (\gamma - 1)][2 + (\gamma - 1)M_1^2]}{(\gamma + 1)^2 M_1^2} \tag{1.4}$$

1.3 Shock Wave Reflections

When a shock wave propagates into a medium and obliquely encounters another medium, it experiences a reflection known as an oblique shock reflection [2]. These shock wave reflections were first discovered by Ernst Mach, who recorded two different shock wave configurations. These experiments were re-conducted by Krehl and van der Geest [3] after being re-examined by Reichenbach [4].

The two initial main shock wave configurations are known as Regular Reflection (RR), a two-shock wave configuration, and as Mach Reflection (MR), a three-shock wave configuration. These wave configurations are displayed in Figure 1.3. The governing equations for these two main reflection configurations are provided in Section 1.3.1.

More recent work has led to the conclusion that more than two wave configurations exist. These shock wave configurations are described in Section 1.4.

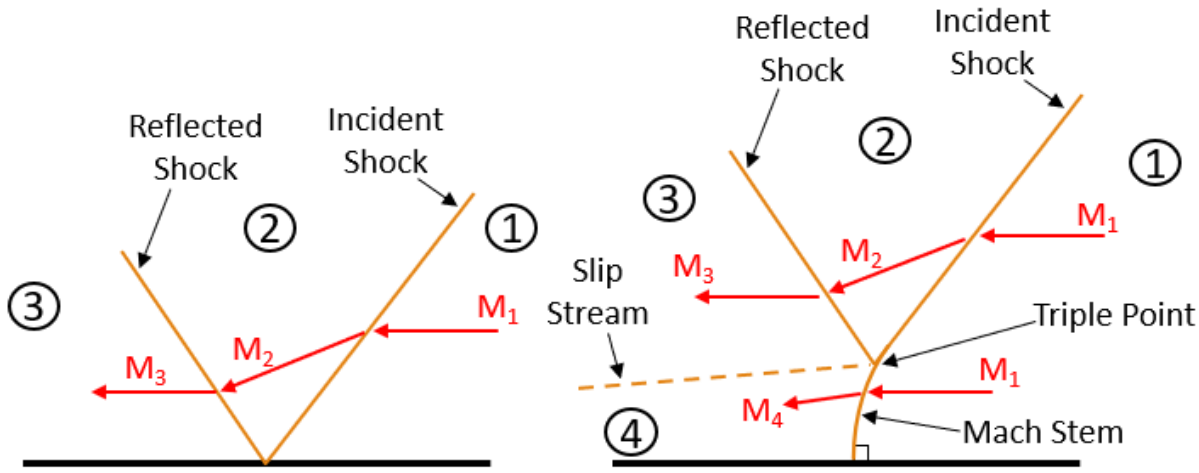

Fig. 1.3 Schematic of Regular Reflection (Left) and Mach Reflection (Right).

1.3.1 Governing Equations of Two- and Three-Shock Theories

Two-Shock Theory (2ST) and Three-Shock Theory (3ST) were first proposed by von Neumann and are described by Ben-Dor [2]. In order to find an analytical solution to the RR and MR wave configurations in Figure 1.3, the governing equations across an oblique shock need to be defined.

Consider a general oblique shock, pictured in Figure 1.4. The flow states ahead of the oblique shock are defined with i, while behind the shock, the flow states are defined with j. Angle ϕ_j is defined as the angle of incidence between the incoming flow and oblique shock

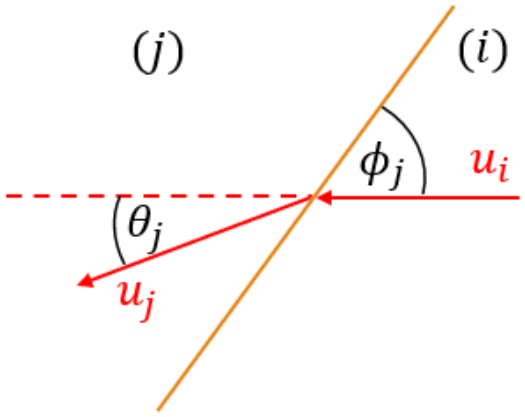

Fig. 1.4 Schematic of oblique shock with flow states ahead (i) and behind (j) the shock.

wave while angle θ_j is the deflection angle of the flow behind the oblique shock.

The conservation equations, for mass, momentum and energy, are written across the oblique shock to relate state i with state j.

The Conservation of Mass:

$$\rho_i u_i \sin\phi_j = \rho_j u_j \sin(\phi_j - \theta_j) \tag{1.5}$$

The Conservation of Momentum in the normal direction:

$$p_i + \rho_i u_i^2 \sin^2\theta_j = p_j + \rho_j u_j^2 \sin^2(\phi_j - \theta_j) \tag{1.6}$$

The Conservation of Momentum in the tangential direction:

$$\rho_i \tan\phi_j = \rho_j \tan(\phi_j - \theta_j) \tag{1.7}$$

The Conservation of Energy:

$$h_i + \frac{1}{2}u_i^2 \sin^2 \phi_j = h_j + \frac{1}{2}u_j^2 \sin^2(\phi_j - \theta_j) \tag{1.8}$$

In equations 1.5 to 1.8, u is the flow velocity (in the oblique shock frame of reference), ρ is density, p is pressure and h is enthalpy. If thermodynamic equilibrium on either side of the oblique shock is assumed, then knowing any four of the eight parameters (u_i, u_j, p_i, p_j, T_i, T_j, ϕ_j, θ_j), will allow for the equations to be solved.

These Equations 1.5 to 1.8 are the basis of the Two-Shock and Three-Shock theories.

1.3.2 Two-Shock Theory (2ST)

The Two-Shock Theory (2ST) is an analytical model for solving for flow parameters near the reflection point of a Regular Reflection. The 2ST is provided by Ben-Dor [2]. Figure 1.5 provides a schematic for the 2ST applied on a Regular Reflection.

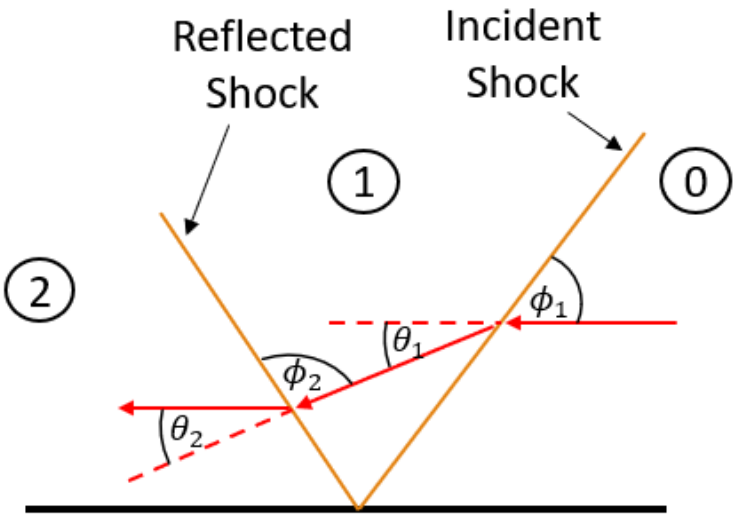

Fig. 1.5 Schematic for the Two-Shock Theory (2ST). Reproduced from [2].

Applying Equations 1.5 to 1.8 for oblique shocks onto both the incident wave i and the

reflected wave r, yields the following eight equations:

- 4 Equations across Incident shock, i:

$$\rho_0 u_0 \sin\phi_1 = \rho_1 u_1 \sin(\phi_1 - \theta_1) \tag{1.9}$$

$$p_0 + \rho_0 u_0^2 \sin^2\phi_1 = p_1 + \rho_1 u_1^2 \sin^2(\phi_1 - \theta_1) \tag{1.10}$$

$$\rho_0 \tan\phi_1 = \rho_1 \tan(\phi_1 - \theta_1) \tag{1.11}$$

$$h_0 + \frac{1}{2}u_0^2 \sin^2\phi_1 = h_1 + \frac{1}{2}u_1^2 \sin^2(\phi_1 - \theta_1) \tag{1.12}$$

- 4 Equations across Reflected shock, r:

$$\rho_1 u_1 \sin\phi_2 = \rho_2 u_2 \sin(\phi_2 - \theta_2) \tag{1.13}$$

$$p_1 + \rho_1 u_1^2 \sin^2\phi_2 = p_2 + \rho_2 u_2^2 \sin^2(\phi_2 - \theta_2) \tag{1.14}$$

$$\rho_1 \tan\phi_2 = \rho_2 \tan(\phi_2 - \theta_2) \tag{1.15}$$

$$h_1 + \frac{1}{2}u_1^2 \sin^2\phi_2 = h_2 + \frac{1}{2}u_2^2 \sin^2(\phi_2 - \theta_2) \tag{1.16}$$

Because the flow behind the shock wave, in region 2, must be parallel to the reflecting surface, an additional equation equation for inviscid flow is found:

$$\theta_1 - \theta_2 = 0 \tag{1.17}$$

With the assumption of thermodynamic equilibrium in all three states, the nine 2ST equations can be expressed with 13 parameters (u_0, u_1, u_2, p_0, p_1, p_2, T_0, T_1, T_2, ϕ_1, ϕ_2, θ_1, θ_2), meaning four of these parameters need to be known in order to solve 2ST.

1.3.3 Three-Shock Theory (3ST)

The Three-Shock Theory (3ST) is an analytical model for solving for flow parameters near the triple point of a Mach Reflection. The 3ST is provided by Ben-Dor [2].

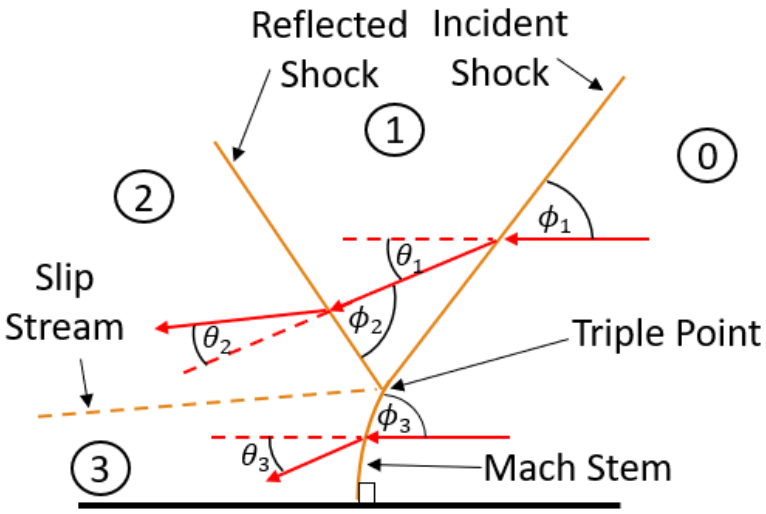

Fig. 1.6 Schematic for the Three-Shock Theory (3ST). Reproduced from [2].

Applying Equations 1.5 to 1.8 for oblique shocks onto both the incident wave i, the reflected wave r, and the Mach stem m, yields the following 12 equations:

- 4 Equations across Incident shock, i:

$$\rho_0 u_0 \sin\phi_1 = \rho_1 u_1 \sin(\phi_1 - \theta_1) \tag{1.18}$$

$$p_0 + \rho_0 u_0^2 \sin^2\phi_1 = p_1 + \rho_1 u_1^2 \sin^2(\phi_1 - \theta_1) \tag{1.19}$$

$$\rho_0 \tan\phi_1 = \rho_1 \tan(\phi_1 - \theta_1) \tag{1.20}$$

$$h_0 + \frac{1}{2}u_0^2 \sin^2\phi_1 = h_1 + \frac{1}{2}u_1^2 \sin^2(\phi_1 - \theta_1) \tag{1.21}$$

- 4 Equations across Reflected shock, r:

$$\rho_1 u_1 \sin\phi_2 = \rho_2 u_2 \sin(\phi_2 - \theta_2) \tag{1.22}$$

$$p_1 + \rho_1 u_1^2 \sin^2\phi_2 = p_2 + \rho_2 u_2^2 \sin^2(\phi_2 - \theta_2) \tag{1.23}$$

$$\rho_1 \tan\phi_2 = \rho_2 \tan(\phi_2 - \theta_2) \tag{1.24}$$

$$h_1 + \frac{1}{2}u_1^2 \sin^2\phi_2 = h_2 + \frac{1}{2}u_2^2 \sin^2(\phi_2 - \theta_2) \tag{1.25}$$

- 4 Equations across Mach stem, m:

$$\rho_0 u_0 \sin\phi_3 = \rho_3 u_3 \sin(\phi_3 - \theta_3) \tag{1.26}$$

$$p_0 + \rho_0 u_0^2 \sin^2\phi_3 = p_3 + \rho_3 u_3^2 \sin^2(\phi_3 - \theta_3) \tag{1.27}$$

$$\rho_0 \tan\phi_3 = \rho_3 \tan(\phi_3 - \theta_3) \tag{1.28}$$

$$h_0 + \frac{1}{2}u_0^2 \sin^2\phi_3 = h_3 + \frac{1}{2}u_3^2 \sin^2(\phi_3 - \theta_3) \tag{1.29}$$

Because the flow states of region (2) and (3) are only separated by a contact surface, or slipstream s, then the pressure across this surface is constant:

$$p_2 = p_3 \tag{1.30}$$

And with the assumption of inviscid flow, as well as a thin contact surface, s, with streamlines on both sides being parallel, the following equation applies:

$$\theta_1 \mp \theta_2 = \theta_3 \tag{1.31}$$

This gives rise to two possible solutions, which therefore means the solution is not unique.

- Standard Three-Shock Theory: $\theta_1 - \theta_2 = \theta_3$ (Mach Reflection)

- Nonstandard Three-Shock Theory: $\theta_1 + \theta_2 = \theta_3$ (von Neumann Reflection)

With the assumption of thermodynamic equilibrium in all four states, the 14 3ST equations can be expressed with 18 parameters (u_0, u_1, u_2, u_3, p_0, p_1, p_2, p_3, T_0, T_1, T_2, T_3, ϕ_1, ϕ_2, ϕ_3, θ_1, θ_2, θ_3), meaning four of these parameters need to be known in order to solve 3ST.

1.4 All Possible Shock Wave Reflections

Although there were initially just two shock wave reflection configurations discovered by Ernest Mach [3][4], newer research has suggested that there are many more unique shock wave configurations [5]. Currently, there are 13 known shock wave configurations, which are presented in Figure 1.7 [2] [5].

Based on current knowledge, the two main reflections are known as Regular Reflection (RR), shown in Figure 1.3 (Left) and the Irregular Reflection (IR). Irregular Reflections are subdivided into the categories of strong shock reflections called Mach Reflections (MR), as seen in Figure 1.3 (Right), and weak shock reflections called von Neumann Reflections (vNR), Guderley Reflections (GR) and Vasilev Reflections (VR) [2][6][7][8][9]. These wave configurations are portrayed in Figure 1.9.

1.4.1 vNR/GR/VR Configurations

The two-shock and three-shock theories, derived in Sections 1.3.2 and 1.3.3, describe the flow field behind both the Regular Reflection and the Mach Reflection with the assumption of shocks with negligible thickness and that all the shocks respect the Rankine-Hugoniot conditions, Equations 1.2, 1.3 and 1.4. The two-shock and three-shock theories provide good agreement with experimental data for strong shocks, but not for weak ones. Experimental

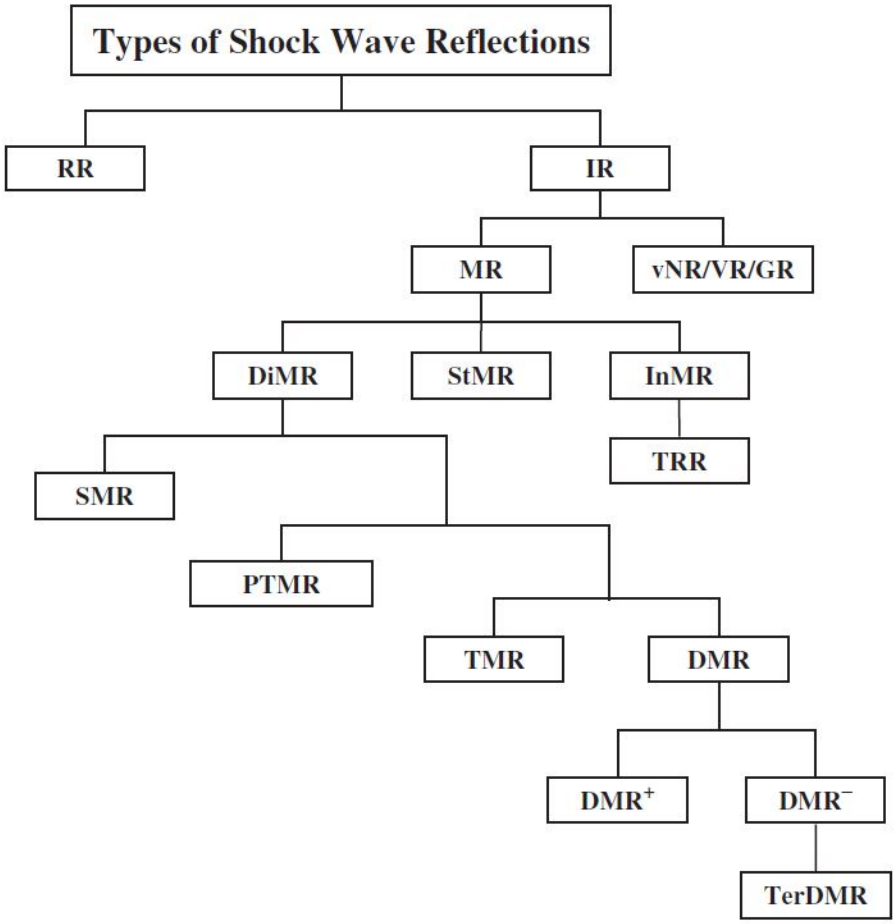

Fig. 1.7 13 Possible Shock Reflections taken from [5]

data showed a reflection flow pattern, similar to IR, also exists in a range where von Neumann theory predicts neither RR nor IR. This discrepancy between the theoretical and experimental results is known as the von Neumann paradox [2][6][9]. The von Neumann paradox shows that during experiments, the Regular Reflection exists under conditions to which no theoretical solution should exist.

The triple point paradox [10] is another discrepancy. This paradox shows a reflected shock wave with a similar configuration to the Mach Reflection (MR) for weak shocks, even though theoretical analysis would show no triple point should exist.

In order to solve the paradoxes, Guderley [7] [11] proposed a four-wave structure (Figure 1.8), in which the Mach stem (M), incident wave (I) and reflected wave (R) are featured as before but with the addition of a Prandtl-Meyer expansion fan, emanating from the triple point. This results in some of the flow near the triple point, behind the incident shock wave, to be supersonic.

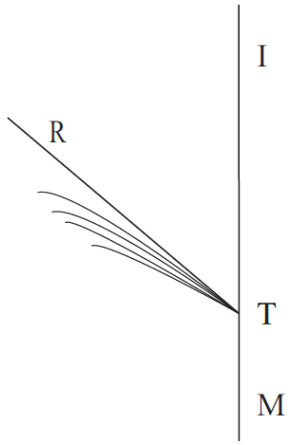

Fig. 1.8 The Guderley 4-wave structure taken from [5].

The work from Vasilev [8] resulted in a third possible configuration for these weak shocks, called Vasilev Reflection (VR).

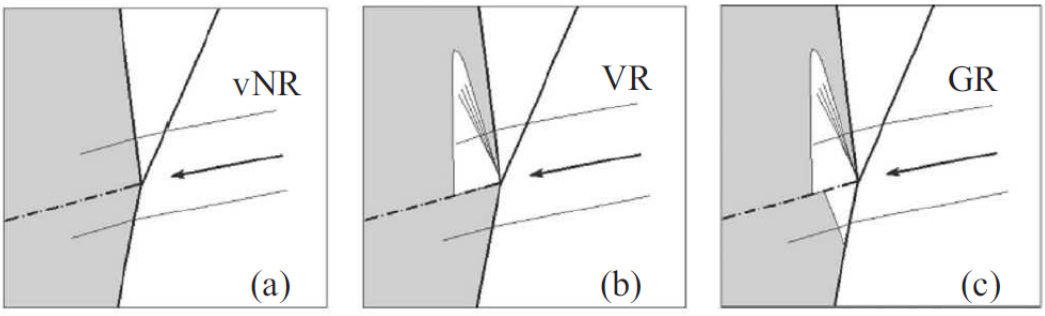

Fig. 1.9 (a) von Neumann Reflection (b) Vasilev Reflection (c) Guderley Reflection. (NOTE: Gray shaded regions denote subsonic flow). Figure taken from [8].

All three of these weak reflections are displayed in Figure 1.9 and are typical for weak

shocks and small reflecting wedge angles [2].

1.4.2 Mach Reflection (MR) Configurations

The MR Configurations are characterized by: an incident shock wave, a reflected shock wave, a Mach stem and a slip stream which all converge at the triple point [2]. These Mach Reflections can be subdivided into Direct Mach Reflection (DiMR), Stationary Mach Reflection (StMR) and Inverse Mach Reflection (InMR) [2] [12]:

- DiMR if the triple Point trajectory moves away from the reflecting surface.
- StMR if the triple Point trajectory moves parallel to the reflecting surface.
- InMR if the triple Point trajectory moves towards the reflecting surface.

These three MR sub-configurations are shown in Figure 1.10 [2].

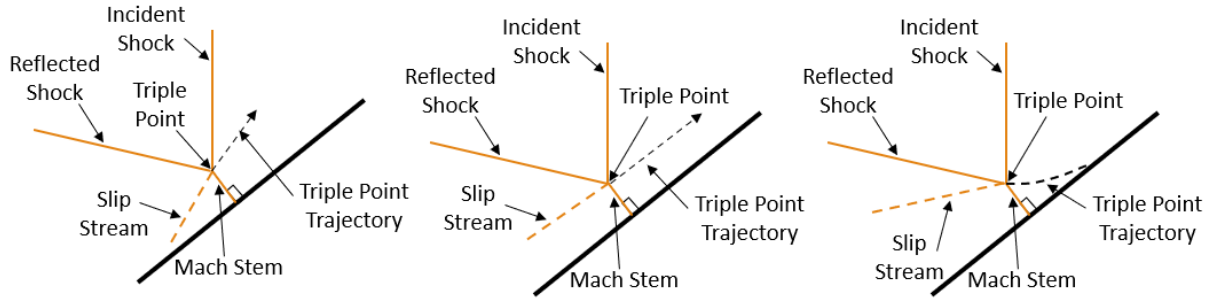

Fig. 1.10 **Left:** DiMR **Mid:** StMR **Right:** InMR

The DiMR is possible for both pseudo steady and unsteady flows while the StMR and InMR are only possible for unsteady flows.

1.4.3 Transitioned Regular Reflection (TRR) Configuration

Since the InMR is only possible for unsteady flows, and the path of the triple point leads to the reflecting surface, then the InMR must terminate once the triple point collides with

the reflecting surface, becoming a Regular Reflection. Because this RR is created following a transition from InMR, it is called a Transitioned Regular Reflection (TRR) [2] [12]. A schematic of the TRR is provided in Figure 1.11. The transition from InMR to TRR is the primary focus of this thesis.

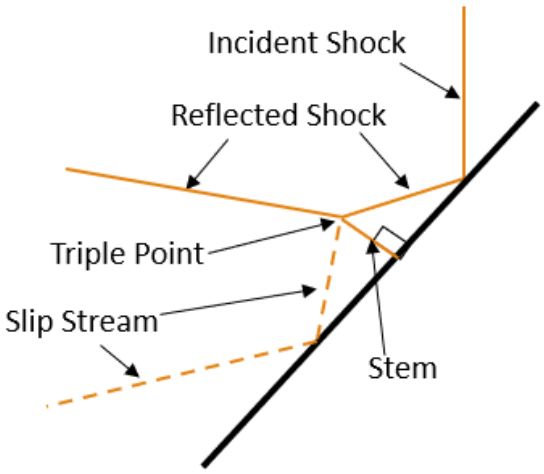

Fig. 1.11 Schematic of the Transitioned Regular Reflection (TRR). Reproduced from [2].

1.5 Problem Statement

The main objective of this thesis is to find the transition point between an Inverse Mach Reflection (InMR) and a Transitioned Regular Reflection (TRR) over a concave cylindrical surface. Figure 1.12 portrays this transition.

Initially, a normal shock propagates with $M_s > 1$ into a gas at rest on a flat surface up to $x = 0$ (Figure 1.12 - Left). Once the normal shock reaches the start of the concave reflecting surface at $x = 0$, with an initial wall angle of $\theta_w^0 = 0^o$, a triple point is generated resulting in an Irregular Reflection (IR). At low wall angles for sufficiently weak shocks, it is suggested by Vasilev [8] that this reflection may initially be a weak shock reflection, such

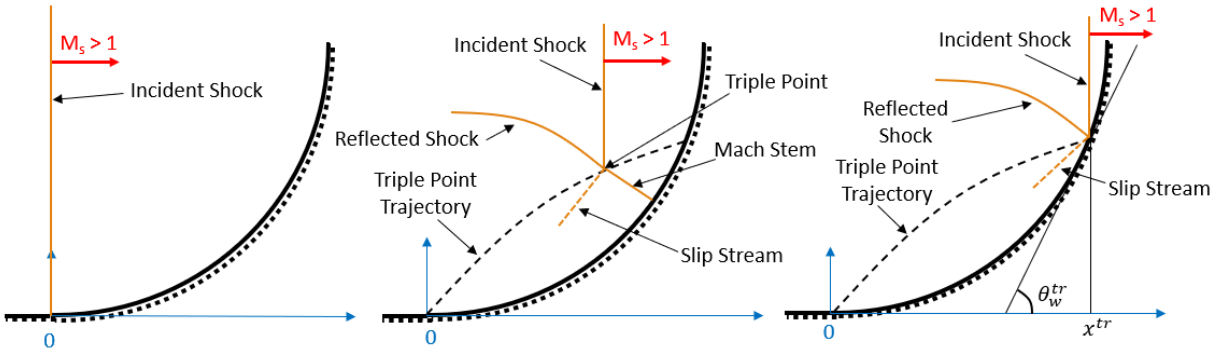

Fig. 1.12 **Left:** The initial normal shock wave. **Mid:** The Inverse Mach Reflection (InMR). **Right:** The Transition Point.

as vNR/VR/GR. Karzova [13] identified this weak reflection as when the incident shock develops a curvature normal to the reflecting surface, before a Mach stem is formed. Cohen [14] later called these reflections a Compressive Reflection (CR).

However, if the shock is sufficiently strong, then a DiMR would develop with the triple point moving away from the reflecting surface [15]. The shock configuration eventually becomes an InMR with a triple point trajectory towards the reflecting surface (Figure 1.12 - Mid). The triple point will eventually reach the reflecting surface (Figure 1.12 - Right) at $\theta_{\mathrm{w}}^{\mathrm{tr}}$ and x^{tr}. Finding $\theta_{\mathrm{w}}^{\mathrm{tr}}$ is the primary objective of this research. The wave then transitions into a Transitioned Regular Reflection (TRR), with a configuration as shown in Figure 1.11.

Cohen [14] suggests that for weak shocks, such as $M_{\mathrm{s}} < 1.1$, the transition between InMR and TRR is not direct. Instead, there is an intermediate RR configuration. In his experiments, he found both the InMR-to-RR and RR-to-TRR transition points. He suggests that at higher Mach numbers, the difference between the two transition points approaches zero resulting in a singular transition point, as stated earlier. These findings are further discussed in Section 3.4.

1.6 Objectives of the Present Research and Structure of the Thesis

In general, the results of shock wave reflections are expected to be important for virtually all practical areas of research involving shock waves, such as: supersonic flight, explosion safety, and medical applications.

The main objective of this thesis is to find the transition point between an Inverse Mach Reflection (InMR) and a Transitioned Regular Reflection (TRR) over a concave cylindrical surface. Finding this transition point is important because different reflection configurations result in different surface loads and temperatures experienced by the reflecting surface.

Previous studies to find the InMR-to-TRR transition point have not provided the most accurate solutions. This is mainly due not being able to visualize small Mach stem heights before reaching the transition point. This results in a significantly large error on the transition angle predicted, because the triple point trajectory is nearly tangent to the reflecting surface just before transition. Therefore, it is important to revisit this problem using newer methods.

This thesis will first outline analytical methods used to predict the InMR-to-TRR transition point in Chapter 2. These methods will include using the transition criteria developed by von Neumann and Hormung [2] which is based on two- and three-shock theory. Other analytical predictions, including those proposed by Ben-Dor [16] [17], where three different pathways for the corner-generated signals are selected, and those described by Itoh [18], which are the Classical and Modified CCW equations, are also described. These analytical solutions are plotted over a range of incident shock Mach numbers of $M_s > 1$ up to $M_s = 4$.

Chapter 3 discusses the previous experiments used to find the transition point. First,

older experiments by Ben-Dor and Takayama (1980) [19] and Takayama and Sasaki (1983) [20] are presented. Then the recent experiments by Kleine [21][22], which directly address some of the faults of these early experiments, are discussed. Finally, the results from weak shock ($M_s < 1.1$) experiments by Gruber [23] and Cohen [14] are shown.

Chapter 4 focuses on the Computational Fluid Dynamics (CFD) predictions. First, numerical predictions by Taieb [24], using an in-house WENO method, and Koronio [15], using a commercial solver ANSYS FLUENT, are shown. Then the CFD predictions using our in-house flow solver, Masterix [25], are described. A grid convergence study is included to ensure the results obtained are independent from the mesh size.

Chapter 5 describes using Geometric Shock Dynamics (GSD) as a numerical technique to find the transition angle. The governing equation, known as the $A - M$ rule, and the numerical scheme used are both derived. Then the results obtained using GSD are presented along with a grid convergence study.

A general comparison of the results is performed in Chapter 6. While previous chapters mainly focused on finding the InMR-to-TRR transition point, this chapter also looks at the InMR wave configuration before the transition point, as predicted by each method. For instance, the triple point trajectory and Mach stem height evolution found using each method is plotted. This chapter will also provide a overall summary of all the methods used to find the InMR-to-TRR transition point. Some concluding remarks and future work are discussed in Chapter 7.

Chapter 2

Analytical Predictions

2.1 Introduction

Predicting the InMR-to-TRR transition point has been of interest for many researchers over the years. Early research in the 1940s was focused on finding the IR to RR transition. Based on the work done mainly by von Neumann [26], four transition criteria are proposed in Section 2.2 for finding the RR to MR transition point [2]. Continuous research has been done since this time due to the inconsistency in finding a singular transition criterion for all ranges of Mach numbers.

In 1981, Itoh [18] used Geometric Shock Dynamics (GSD) to predict the triple point trajectory of the MR over a concave cylindrical surface. This work is summarized in Section 2.4. Later, based on the length-scale concept by Hornung [27], Ben-Dor and Takayama developed their own theory based on the physical communication of the flow to the triple point [2][16][28]. This theory relied on selecting a pathway for the corner-generated signals to travel from the corner of the cylindrical wedge to the transtion point. This work is detailed in Section 2.3.

2.2 Transition Criteria

Early analytical predictions for finding the transition angle involved the transition criteria between 2ST (see Section 1.3.2) and 3ST (see Section 1.3.3). These transition criteria are known as the four suggested RR-to-IR transition criteria [2]. Figure 2.1 provides the schematic for the shock polar diagrams used to predict the transition angle between RR and MR.

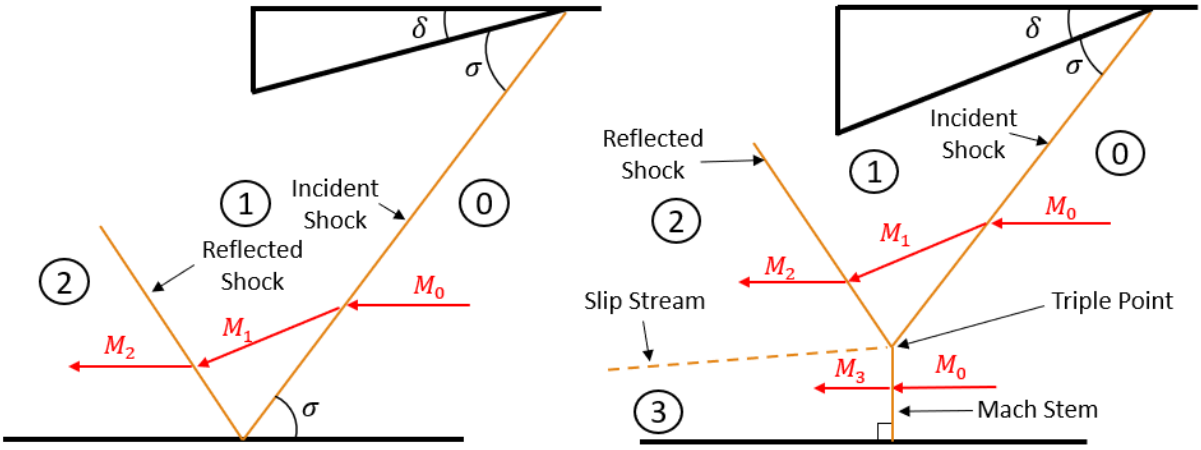

Fig. 2.1 The schematic used for the RR (Left) and MR (right) Shock Polar diagrams.

2.2.1 Shock Polars

In order to understand the transition criteria, shock polars must be defined. Shock polars, which were first proposed by Kawamura and Saito [2] [29] in order to help better understand the boundary conditions for MR and RR. These shock polars use a graphical representation to express the boundary conditions in terms of the flow direction angle, δ, and the flow static pressure, p.

An example of a shock polar is shown in Figure 2.2. In this example figure, point a indicates the location where the flow parameters on either side of the oblique shock are

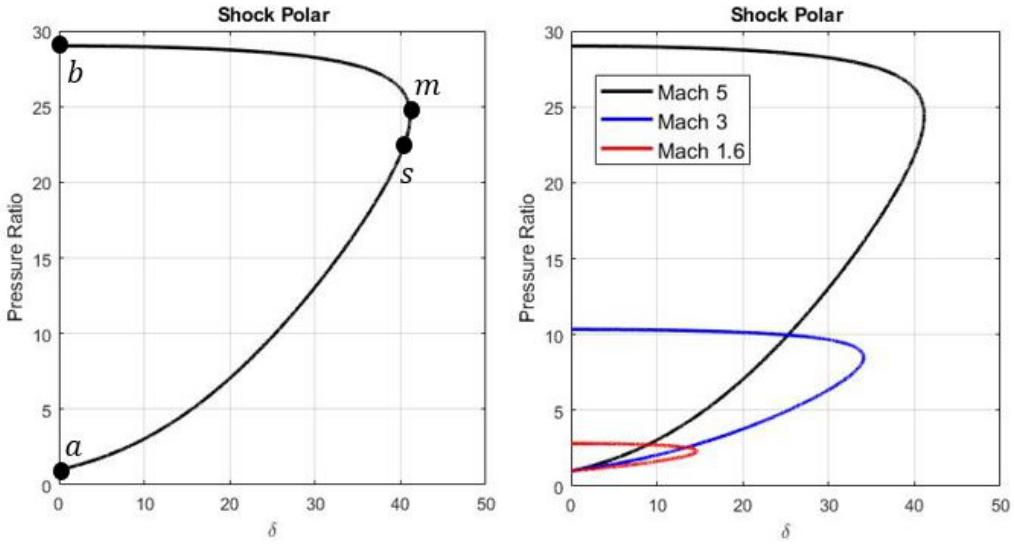

Fig. 2.2 **Left:** Example Shock Polar with $M_0 = 5$. **Right:** Example Shock Polars with $M_0 = 5$, $M_0 = 3$ and $M_0 = 1.6$.

identical. This occurs when ϕ_1 (ϕ_j from Figure 1.4) equals $\mu_0 = \sin^{-1}(1/M_0)$. Point b refers to the location where the oblique shock becomes a normal shock, and is thus the strongest shock configuration. Point m is the point of maximum deflection. Point s divides the diagram into 2 sections: Section $a - s$ for the weak shock portion, where $M_1 > 1$ and Section $s - b$ for the strong shock portion, where $M_1 < 1$. Figure 2.2 (Right) shows the effect of the initial Mach number M_0 on the shock polar configuration.

While Figure 2.2 provides a good example of a shock polar for the incident shock, Figure 2.3 provides a polar representation of both the incident shock wave and reflected shock wave. For the case on the left with $\delta = 25^o$, the intersecting point between the reflected shock polar and the strong shock portion of the incident shock wave represents the existence of a Mach Reflection (MR). For the case on the right with $\delta = 15^o$, the intersecting point between the reflected shock polar and the y-axis represents the existence of a Regular Reflection (RR).

Although Figure 2.3 shows two distinct cases, for MR and RR, Figure 2.4 represents a

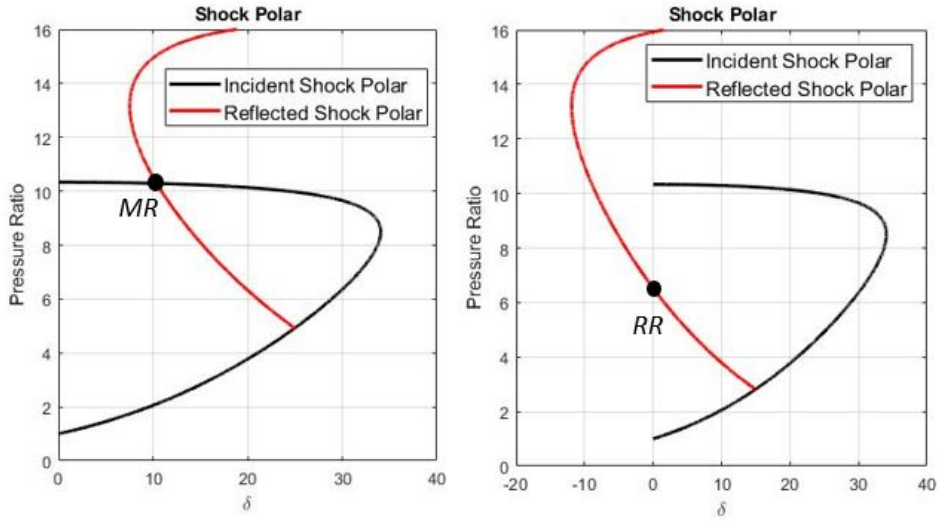

Fig. 2.3 **Left:** Example Shock Polar with $M_s = 3$ and a $\delta = 25^o$ resulting in a Mach Reflection. **Right:** Example Shock Polar with $M_s = 3$, and a $\delta = 15^o$ resulting in a Regular Reflection.

case where both solutions are possible. This is called the dual-solution domain. In order to find the transition point, four transition criteria were proposed [2] and these are described in Section 2.2.2.

2.2.2 Four Transition Criteria Description

The transition criteria between 2ST and 3ST has been studied for years and four transition criteria have been proposed, three of them by von Neumann [2] and one by Hornung [27].

Detachment Criterion

The Detachment Criterion states that from a Regular Reflection, once the reflected shock can no longer completely turn the incoming supersonic flow tangentially to the reflected surface, then a RR can no longer exist. This triggers the need for a Mach stem, which results in a Mach Reflection [2].

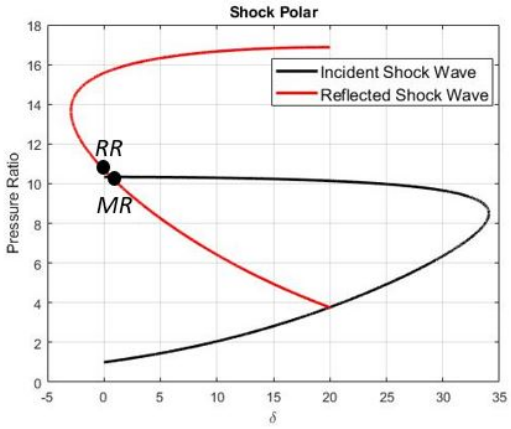

Fig. 2.4 Example Shock Polar with $M_s = 3$ and a $\delta = 20^o$ resulting in both possible solutions: MR and RR.

Mechanical Equilibrium Criterion

This criterion requires that both MR (using 3ST) and RR (using 2ST) configurations must result in identical post-shock pressures. This maintains mechanical equilibrium during the transition between the two wave configurations [2].

Sonic Criterion

The sonic criterion occurs when the flow behind the reflected shock reaches sonic speed (in the incident shock frame of reference) and therefore, when acoustic signals generated on the reflecting surface cannot catch up to the reflecting point and communicate this obstacle to the incident shock, there is a transition from RR to MR [2].

Length-Scale Criterion

The length-scale criterion, developed by Hormung [27], says that the Mach stem has a finite size. Therefore, pressure signals must be communicated to the reflection point for the transition from RR to MR to occur. This criterion happens to predict the same transition

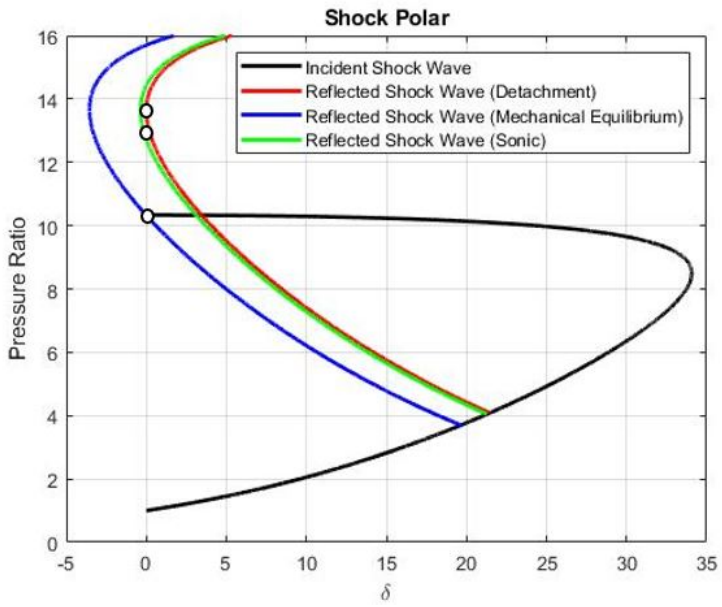

Fig. 2.5 Example Shock Polar with $M_0 = 3$ showing each of the transition criteria.

point as the sonic criterion for pseudo-steady flows and the mechanical equilibrium criterion of steady flows.

Shock Polar Representation of Each Transition Criteria

The Shock Polar representation of each of the four transition criteria is shown in Figure 2.5. The Detachment and sonic criterion provide nearly identical transition points and therefore will be referred to as the sonic/detachment criteria in future figures. In Figure 2.5, any shock polars to the left of the Mechanical Equilibrium criterion will be Regular Reflections while any shock polars to the right of the sonic/detachment criteria will be Mach Reflections. Shock polars in between are within the dual-solution domain.

2.2.3 Predictions

The predictions for the transition criteria are provided in Figure 2.6. The plot on the left uses the incident shock Mach number on the x-axis while the plot on the right uses the inverse pressure ratio of the incident shock on the x-axis. This ratio can be found using the Rankine-Hugoniot relation for a normal shock (equation 1.2).

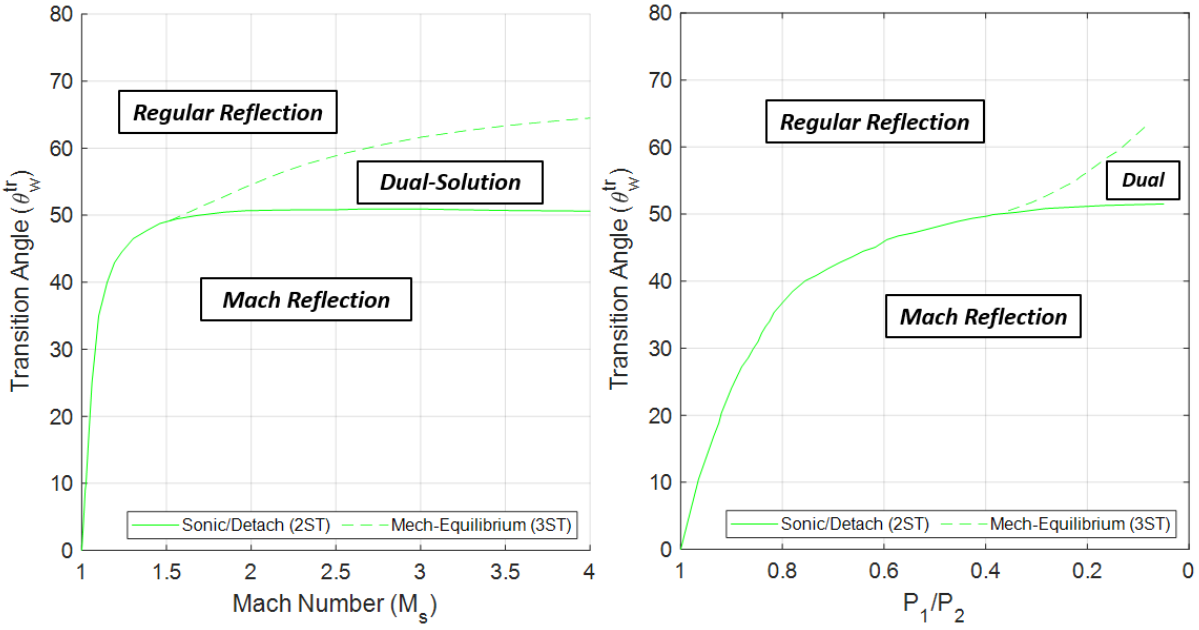

Fig. 2.6 The predicted Mach Reflection to Regular Reflection transition angle for the sonic/detachment criteria and the mechanical equilibrium criteria.

From Figure 2.6, it can be seen that the RR domain is shown as being above the mechanical equilibrium criteria while the MR domain is for wall angles below the sonic/detachment criteria. The domain in between is called the dual-solution domain.

2.3 Ben-Dor 3 Analytical Predictions

Ben-Dor provides three different predictions for the transition angle [2] [16] [28] [17]. All three predictions are based on the same assumption: That a Mach Reflection will exist

when corner-generated perturbation signals catch-up with the wave front, resulting in a Mach stem and that a Regular Reflection will exist once these signals fail to catch-up with the wave front.

This assumption is based on the length-scale concept of Hornung [27] which states that the wave configuration for Regular Reflection has no length scale since both the incident and reflected waves can extend towards infinity. However, the Mach Reflection includes a length scale due to the existence of the Mach stem connecting the reflected point to the triple point. Therefore, in order for a Mach Reflection to exist, a physical length scale must exist.

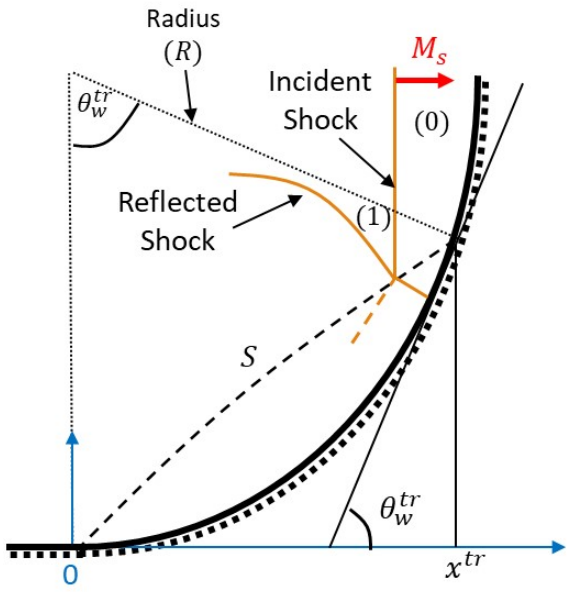

Fig. 2.7 Problem setup for Ben-Dor predictions. Reproduced from [2].

The governing equation of the Ben-Dor analytical predictions, based on the length-scale concept, is derived in Appendix A.1. It is given as:

$$R \sin \theta_{\mathrm{w}}^{\mathrm{tr}} = S \frac{M_{\mathrm{s}}}{V_{10} + C_{10}} \tag{2.1}$$

$$V_{10} = \frac{2(M_s^2 - 1)}{(\gamma + 1)M_s} \tag{2.2}$$

$$C_{10} = \frac{\gamma - 1}{\gamma + 1}\frac{1}{M_s}\sqrt{\left(\frac{2\gamma}{\gamma - 1}M_s^2 - 1\right)\left(M_s^2 + \frac{2}{\gamma - 1}\right)} \tag{2.3}$$

The path S needs to be selected. Three possible paths proposed by Ben-Dor are given in Figure 2.8.

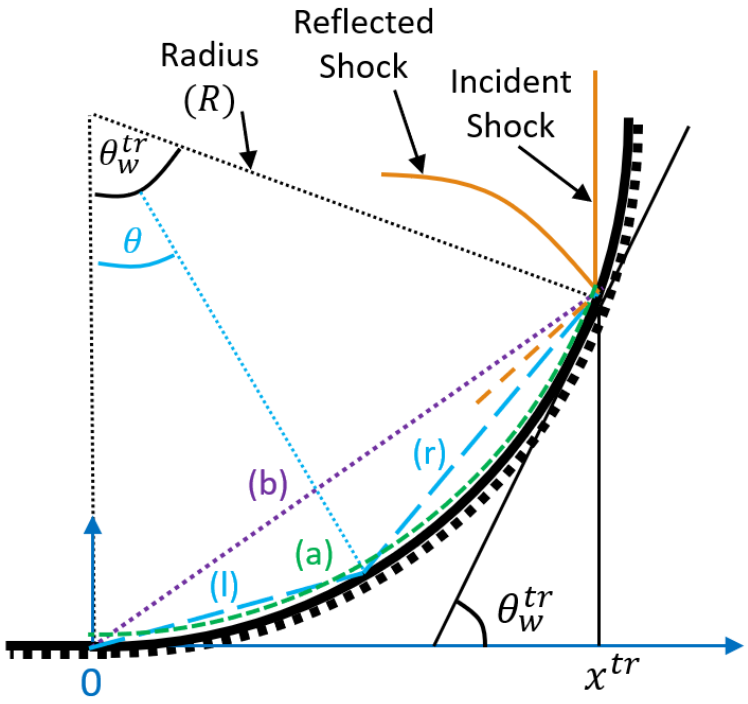

Fig. 2.8 Three pathways proposed by Ben-Dor [16][28].

Path (a): Propagation path is along reflecting surface

The first predicted path is that of a propagation path along the reflecting surface. This is seen in green in Figure 2.8. This implies a path S of:

$$S = R\theta_w^{tr} \tag{2.4}$$

Substituting the path S from Equation 2.4 into Equation 2.1, and rearranging the terms yields the following:

$$\frac{\sin \theta_{\mathrm{w}}^{\mathrm{tr}}}{\theta_{\mathrm{w}}^{\mathrm{tr}}} = \frac{M_{\mathrm{s}}}{V_{10} + C_{10}} \tag{2.5}$$

Path (b): Propagation path is a straight line

The second predicted path is that of a propagation path in a straight line from the corner to the transition point. This is seen in purple in Figure 2.8. This implies a path S of:

$$S = 2R \sin\left(\frac{\theta_{\mathrm{w}}^{\mathrm{tr}}}{2}\right) \tag{2.6}$$

Substituting the path S from Equation 2.6 into Equation 2.1, and rearranging the terms yields the following:

$$\cos\left(\frac{\theta_{\mathrm{w}}^{\mathrm{tr}}}{2}\right) = \frac{M_{\mathrm{s}}}{V_{10} + C_{10}} \tag{2.7}$$

Path ($l + r$): Propagation path is vector sum of particle path l and disturbance path r

The third predicted path is that of a vector sum of the particle path l, which considers the velocity V_1 and the disturbance path r, which considers the speed of sound, c_1. This path is seen in cyan in Figure 2.8. Path l and r are defined as follows:

$$l = R\theta = V_1 \Delta t \tag{2.8}$$

$$\theta = \frac{V_{10}}{M_{\mathrm{s}}} \sin \theta_{\mathrm{w}}^{\mathrm{tr}} \tag{2.9}$$

$$r = a_1 \Delta t \tag{2.10}$$

Substituting path $S = l + r$ from Equations 2.8 and 2.10 into Equation 2.1 and rearranging the terms yields:

$$\frac{2\sin\frac{\theta_{\mathrm{w}}^{\mathrm{tr}}-\theta}{2}}{\sin\theta_{\mathrm{w}}^{\mathrm{tr}}} = \frac{C_{10}}{M_{\mathrm{s}}} \tag{2.11}$$

Results

Figures 2.11 and 2.12 provide the predictions from the Ben-Dor analytical solutions with Mach numbers ranging from $M_{\mathrm{s}} > 1$ up to $M_{\mathrm{s}} = 4$. All three Ben-Dor solutions produce higher transition angle predictions than from the transition criteria of Section 2.2.2. Path (a) predicts the lowest transition angle while path (b) predicts the highest. The difference between path (a) and path (b) angles approaches 10^o when $M_{\mathrm{s}} > 1.5$. These predictions are also compared to the Classical and Modified CCW predictions, which are described in Section 2.4.

2.4 Itoh Classical and Modified CCW Predictions

Itoh [18] provides two analytical solution to track the Mach stem height as a function of initial Mach number, M_{s}, of the shock wave and of wall angle, θw. These analytical predictions also find the transition angle, $\theta_{\mathrm{w}}^{\mathrm{tr}}$, between Mach and Regular Reflection.

These two analytical predictions are based on Geometric Shock Dynamics (GSD), which directly relates the local geometry with the local Mach number along the shock front. The basis of the GSD is from the Chester [30], Chisnell [31] and Whitham [32] (CCW) theory. A schematic for the derivation of the Classical and Modified CCW Equations is shown in Figure 2.9.

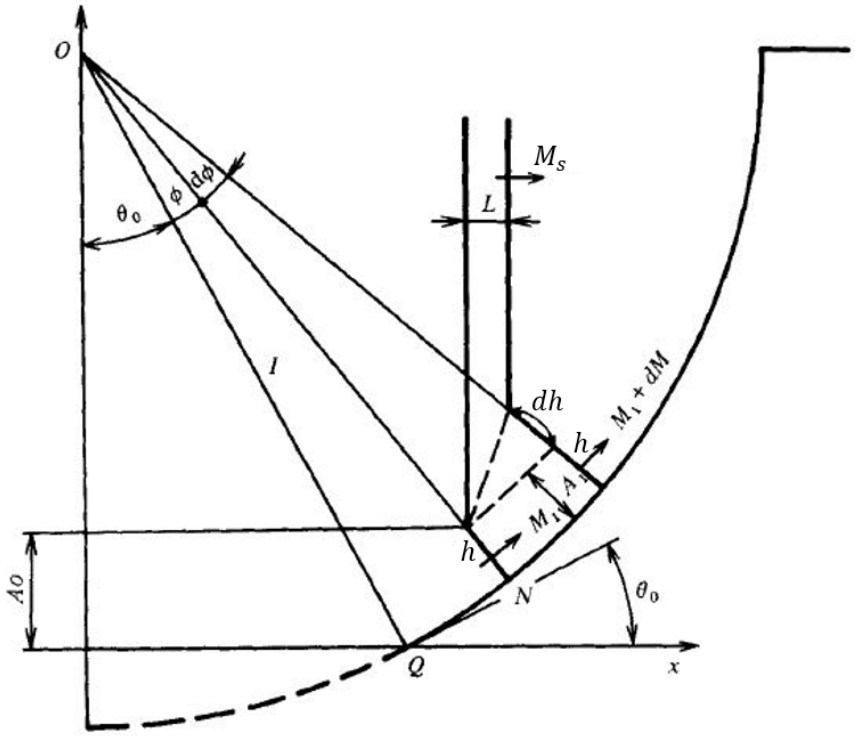

Fig. 2.9 Schematic for both CCW Equations taken from [18].

2.4.1 Classical CCW

Based on the work by Whitham [32] and Itoh [18], the analytical solution using Geometric Shock Dynamics, referred to as the CCW theory, can be found.

The $A-M$ rule [33], obtained from the 1D Euler system (with x in the axial direction), with all flow properties expressed in terms of area and Mach number, is:

$$\frac{1}{A}\frac{\mathrm{d}A}{\mathrm{d}x} + \frac{M\lambda(M)}{M^2-1}\frac{\mathrm{d}M}{\mathrm{d}x} = 0 \tag{2.12}$$

$$\lambda(M) = \left(1 + \frac{2}{\gamma+1}\frac{1-\mu^2}{\mu}\right)\left(1 + 2\mu + \frac{1}{M^2}\right) \tag{2.13}$$

$$\mu = \sqrt{\frac{(\gamma-1)M^2+2}{2\gamma M^2+1-\gamma}} \tag{2.14}$$

A coordinate transformation from Cartesian coordinates (x,y) to local coordinates (α, β) (see Figure 5.1) is expressed as follows:

$$\begin{aligned} \frac{\partial x}{\partial \alpha} &= M\cos\theta; & \frac{\partial y}{\partial \alpha} &= M\sin\theta; \\ \frac{\partial x}{\partial \beta} &= -A\sin\theta; & \frac{\partial y}{\partial \beta} &= A\cos\theta; \end{aligned} \tag{2.15}$$

Using these coordinate transformations, the $A-M$ Rule from Equation 2.12 becomes:

$$\frac{1}{A}\frac{\mathrm{d}A}{\mathrm{d}\alpha} + \frac{M\lambda(M)}{M^2-1}\frac{\mathrm{d}M}{\mathrm{d}\alpha} = 0 \tag{2.16}$$

Whitham [32] was able to use Equation 2.16 to relate the wall angle to the strength of the shock:

$$\theta\mathrm{w} = \int_{M_s}^{M}\left[\frac{\lambda(M)}{M^2-1}\right]^{1/2}\mathrm{d}M \tag{2.17}$$

Equation 2.17 is referred to as the Classical CCW Equation by Itoh [18]. Like GSD, the Classical CCW Equation is only dependent on the shock front, and not the flow properties behind the shock wave.

2.4.2 Modified CCW

Itoh [18] then proposed a modified version of Equation 2.17 by introducing a new term, η, to account for effects of the reflected shock and slip stream:

$$\theta\mathrm{w} = \int_{M_\mathrm{s}}^{M}\left[\frac{\lambda(M)}{M^2-1} + \frac{\eta}{M^2}\right]^{1/2}\mathrm{d}M \tag{2.18}$$

$$\eta = \left(1-\frac{M_s^2}{M^2}\right)\frac{(F+2B)E}{(M^2-1)BD} + \frac{1}{2}\ln\left(\frac{A_0}{A}\right)\frac{D^{3/2}(M^2+1)+4(M^2-1)^2F}{(M^2-1)DE} \tag{2.19}$$

$$A_0 = \cos\theta_0 - (1-h)\cos(\theta_0+\phi) \tag{2.20}$$

$$A_1 = h \tag{2.21}$$

$$B = 2\gamma M^2 - (\gamma - 1) \tag{2.22}$$

$$C = (\gamma - 1)M^2 + 2 \tag{2.23}$$

$$D = BC \tag{2.24}$$

$$E = 2(M^2 - 1) + \sqrt{D} \tag{2.25}$$

$$F = (\gamma - 1)(1 + \gamma M^4) \tag{2.26}$$

Equation 2.18 is referred to as the Modified CCW Equation. The Classical CCW Equation can be found by making $\eta = 0$ in the Modified CCW Equation. For the purposes of this problem, $\theta_0 = 0$, thus $\theta\mathrm{w} = \theta_0 + \phi = \phi$. Therefore, $A_0 = h\cos(\theta\mathrm{w})$ where h refers to the Mach stem height. Itoh [18] proposes using Equation 2.27 to relate Equation 2.18 to the Mach stem height for a shock propagating on a concave cylindrical surface.

$$\frac{\mathrm{d}h}{\mathrm{d}\phi} = \frac{1-h}{\tan(\theta_0 + \phi)} - \frac{1 - h/2}{\sin(\theta_0 + \phi)}\left(\frac{M_\mathrm{s}}{M_1}\right) \tag{2.27}$$

Simultaneously solving Equations 2.18 and 2.27 provides a Mach stem height for each wall angle $\theta\mathrm{w}$. The InMR-to-TRR transition angle $\theta_\mathrm{w}^\mathrm{tr}$ is found when $h = 0$ for Equations 2.18 and 2.27 [18].

2.4.3 Results

The results for the Mach stem height using $M_\mathrm{s} = 1.6$ as an example is shown in Figure 2.10. The solid red line is the solution for the Classical CCW (Equation 2.17) which predicts the transition point to be $\theta_\mathrm{w}^\mathrm{tr} = 68.0^o$. The dashed red line is the solution for the Modified CCW (Equation 2.18) predicts the transition point to be $\theta_\mathrm{w}^\mathrm{tr} = 64.8^o$. These transition

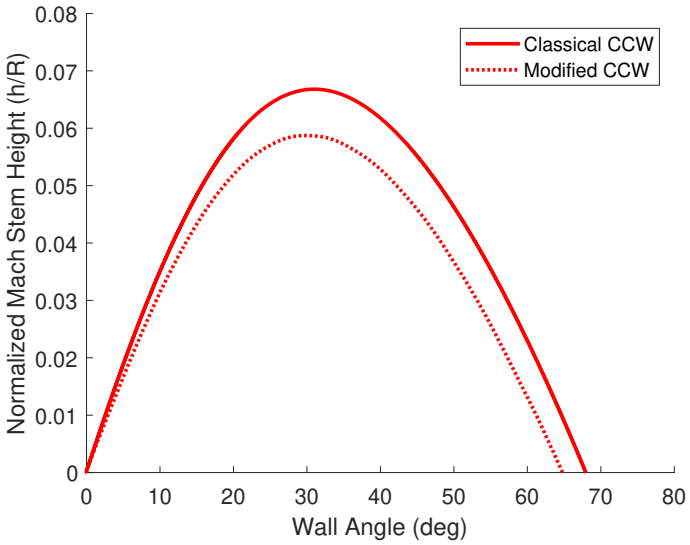

Fig. 2.10 The normalized Mach stem height $\tilde{h} = h/R$ for the InMR over a concave surface with $M_s = 1.6$ for both Classical and Modified CCW.

points are found when $\tilde{h} = h/R = 0$.

Results for the predicted Classical and Modified CCW transition angles ($1 < M_s \leq 4$) are shown in Figures 2.11 and 2.12 with the three analytical predictions from Ben-Dor, the sonic/detachment criteria and the mechanical equilibrium criteria included for reference.

The results from Figures 2.11 and 2.12 show the Modified CCW predicting a lower transition angle than the Classical CCW. However, both of these solutions are bounded by the Ben-Dor path (a) and path (b) solutions. Furthermore, the 2ST and 3ST transition criteria under-predict the InMR-to-TRR transition angle.

2.5 Conclusion

Chapter 2 mainly discussed the analytical methods used to predict the transition point from InMR-to-TRR. Section 2.2 provided details on the transition criteria proposed by Ben-Dor [2] and Hornung [27] and introduced the concept of shock polars. The results (Figure 2.6)

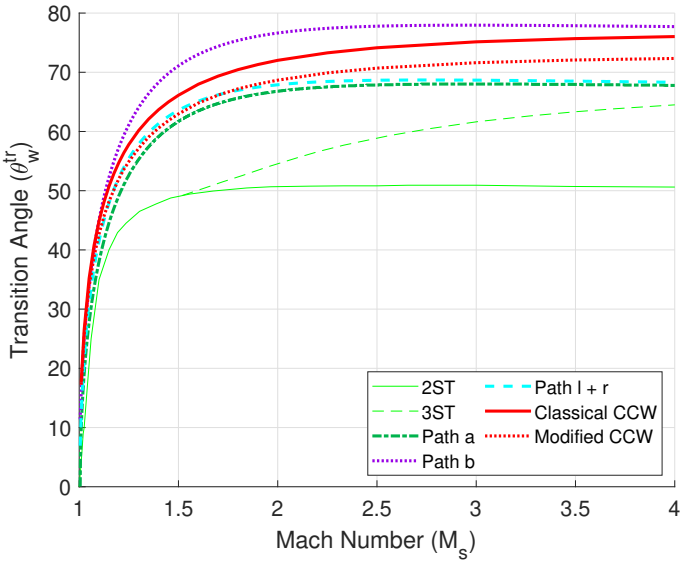

Fig. 2.11 The predicted transition angle, $\theta_{\mathrm{w}}^{\mathrm{tr}}$, plotted with M_{s} based on the on the three pathways proposed by Ben-Dor [2] and the CCW predictions described by Itoh [18].

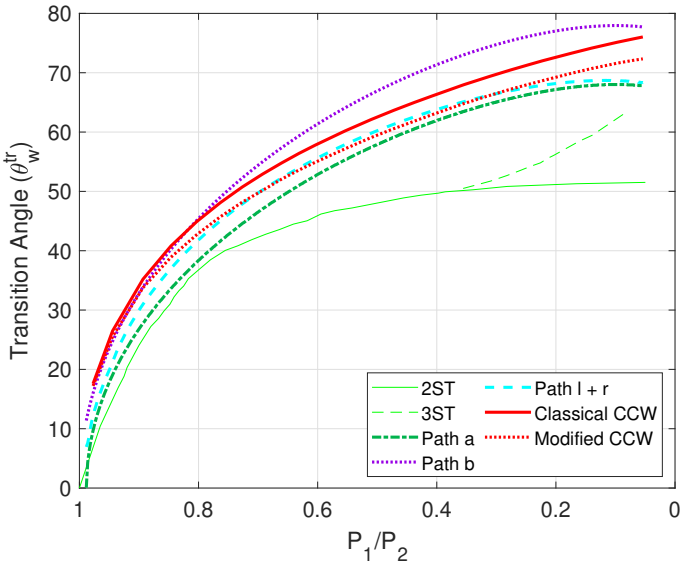

Fig. 2.12 The predicted transition angle, $\theta_{\mathrm{w}}^{\mathrm{tr}}$, plotted with the inverse pressure ratio, based on the on the three pathways proposed by Ben-Dor [2] and CCW predictions described by Itoh [18].

showed three regions of note: The Regular Reflection, the Mach Reflection and a dual-solution domain. Then Section 2.3 discussed the three analytical predictions proposed by Ben-Dor and Takayama [2][16][28] and the Classical and Modified CCW equations used by Itoh [18]. The results of these analytical predictions are seen in Figures 2.11 and 2.12, where all five predictions show transition angles greater than the transition criteria.

Further comparisons of the transition angle continue in Chapter 3 for experiment results, in Chapter 4 for Computational Fluid Dynamics (CFD) and in Chapter 5 for Geometric Shock Dynamics (GSD).

Chapter 3

Experimental Investigations

3.1 Introduction

Many experiments have been performed to find the InMR-to-TRR tansition angle, $\theta_{\mathrm{w}}^{\mathrm{tr}}$. Although older experiments by Ben-Dor and Takayama (1980) [19] and Takayama and Sasaki (1983) [20] have provided estimated transition points, more recent experiments were performed to improve the accuracy of the predicted InMR-to-TRR transition point [21][22]. Experiments were also conducted to find the transition point of weak shock ($M_{\mathrm{s}} < 1.1$) reflections [14][23]. The results of all these experiments are compared to the analytical predictions of Chapter 2.

3.2 Older Experiments

The experiment results by Ben-Dor and Takayama [19] were collected using streak camera photography with a radius of the cylindrical concave wedge of 40 mm. The results from Takayama and Sasaki (1983) [20] were similarly collected with a streak camera with curved slits. The data is collected and shown in Figures 3.5 and 3.6 as blue un-filled (Ben-Dor and

Takayama [19]) and filled (Takayama and Sasaki [20]) squares.

Timofeev and Previtali [21] suggest two main reasons for the low predictions of these early experimental results. The first is due to viscous effects, which present themselves in the shock thickness and therefore affect the local wall angle measured. The second reason is due to poor optical resolution, which is due to small Mach stems just prior to transition (see Figure 3.1). This results in a challenge to obtain accurate measurements.

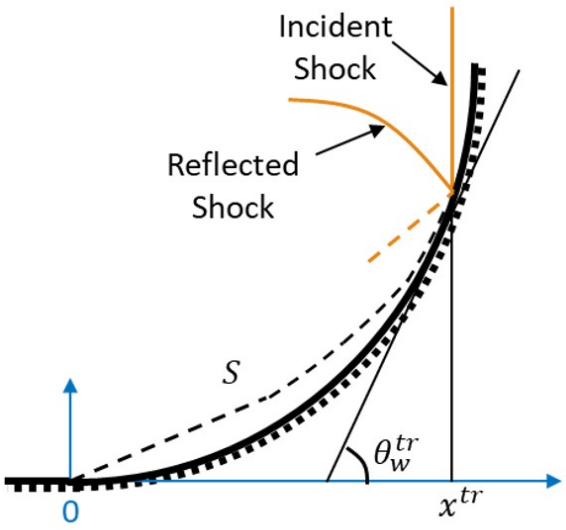

Fig. 3.1 Theoretical triple point trajectory which shows the trajectory S approaching the transition angle nearly tangential to the concave cylindrical surface.

The results from Kleine [21] [22] clarified the measured transition angle by addressing these issues: The viscous effects are alleviated by using a larger radius of curvature, thus increasing the Reynolds number and the size of the Mach stem (which is directly proportional to the radius). Using a larger radius of curvature (140 mm compared with 40 mm) also helps improve the optical visualization. These new experiments are discussed in Section 3.3.

3.3 Recent Experiments by Kleine

3.3.1 Setup

The experiments [22] were conducted using a diaphragm-operated shock tube in air ($\gamma = 1.4$) with temperatures ranging from 290 K to 293 K. In Figure 3.2, the cylindrical reflecting surface is shown with a radius of 140 mm, and goes from 0^o to 90^o. The incident Mach number, M_s, was found using two pressure transducers with an uncertainty of ± 0.008. The test section had optical access for a for a high-speed camera capable of 5,000,000 fps.

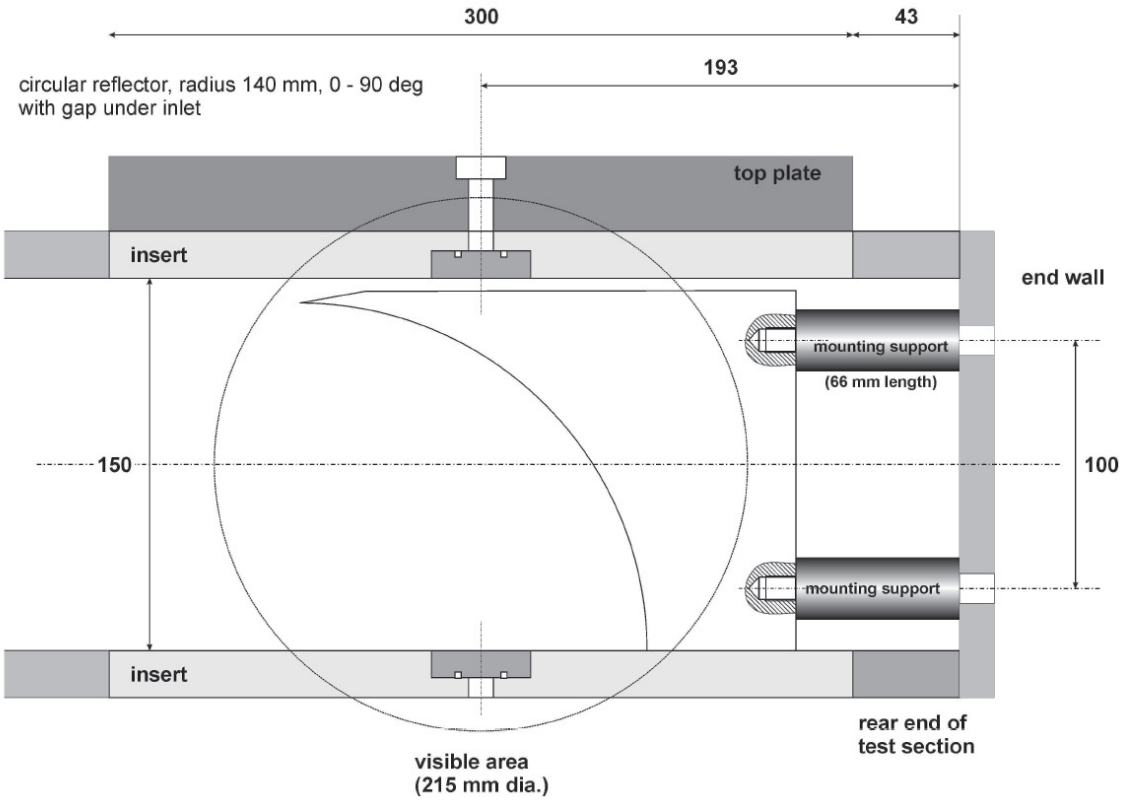

Fig. 3.2 Schematic of the test section for the experiments by Kleine [21].

3.3.2 Results

The results obtained had incident Mach numbers, M_s, ranging from $M_s = 1.03$ to $M_s = 3.17$. An example of the results is shown in Figure 3.3 for $M_s = 1.596 \pm 0.008$. The results are obtained from schlieren images, showing the change in density across each of the shocks (incident, reflected and Mach stem) and slip stream.

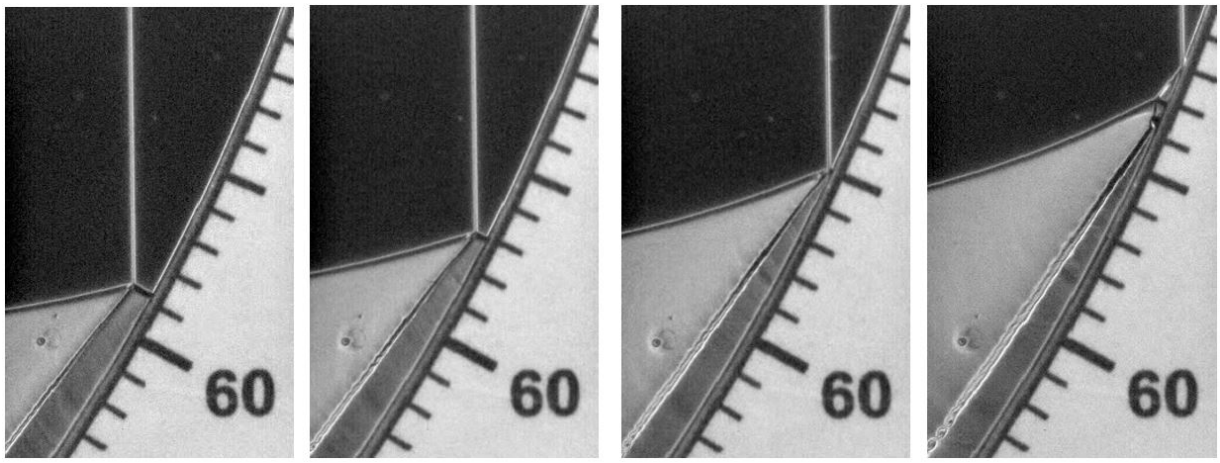

Fig. 3.3 The experiment results for $M_s = 1.596$ [22]. **Left:** Inverse Mach Reflection (InMR) with normalized Mach stem height of $\tilde{h} = h/R = 0.0106$. **Mid-Left:** InMR with normalized Mach stem height of $\tilde{h} = h/R = 0.0056$. **Mid-Right:** Transition Point $\theta_w^{tr} = 65.0^o$. **Right:** Transitioned Regular Reflection (TRR).

Figure 3.3 (Left) portrays the Mach Reflection at $\theta w = 60.0^o$. This wave configuration is evident due to the presence of the incident shock wave, the Mach stem, the reflected shock and the slip stream. At this moment, the normalized Mach stem height is $\tilde{h} = h/R = 0.0106$. The next image in Figure 3.3 (Mid-Left) shows the Mach reflection with $\tilde{h} = 0.0056$ at $\theta w = 62.0^o$. The decrease in Mach stem height indicates the presence of an Inverse Mach Stem (InMR). Figure 3.3 (Mid-Right) then shows the transition point at $\theta_w^{tr} = 65.0^o$. Figure 3.3 (Right) shows the Transitioned Regular Reflection (TRR) when $\theta w = 68.0^o$. The results for all the tests with different Mach numbers are plotted in Figures

3.5 and 3.6.

Overall, the new experiment results provide higher predictions for the transition angle $\theta_{\mathrm{w}}^{\mathrm{tr}}$, than from the earlier experiments. Previtali [22] suggests these results are more accurate than previous experiments due to the higher Reynolds number and better optical resolution. These results will be further compared with Computational Fluid Dynamics (CFD) results in Chapter 4 and with Geometric Shock Dynamics in Chapter 5.

3.4 Weak Shock Wave Experiments

Gruber and Skews [23] (2013) conducted experiments with weak shocks ($1.03 < M_{\mathrm{s}} < 1.1$). Weak shock reflections were found to provide a different wave configuration than the strong ones. As the weak shock develops, it becomes a vNR/GR/VR (later called a Compressive Reflection, CR, by Cohen [14]) before becoming a MR. It was hypothesized by Gruber [23] that an intermediary step would exist in the transition from InMR-to-TRR as M_{s} approaches the acoustic limit ($M_{\mathrm{s}} \to 1$). This intermediary step would be a RR. However, the results from these weak shock experiments had resolution constraints and therefore the exact configuration could not be distinguished [23].

Later, Cohen and Skews (2020) [14] provided experimental data with weaker shocks ranging from $1.007 < M_{\mathrm{s}} < 1.1$. For these weak shocks, Cohen [14] found an intermediate step between the transition from InMR-to-TRR. Experiments showed two-distinct transitions: An InMR-to-RR transition followed by a RR-to-TRR transition. The results for these two transition points are found in Figure 3.4. Based on these results, Cohen [14] suggests that the two transition points, InMR-to-RR and RR-to-TRR, converge at higher Mach numbers. This may have resulted in the assumption of a singular InMR-to-TRR transition point from earlier literature.

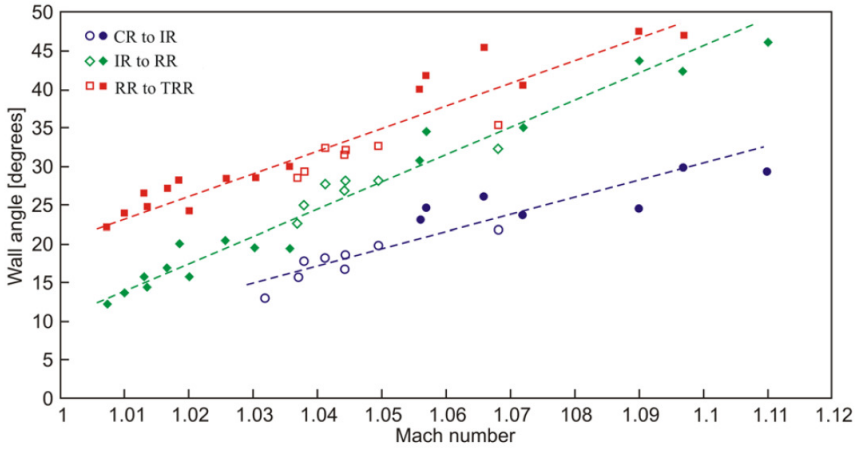

Fig. 3.4 The transition angles for CR-to-InMR (labelled as IR), InMR-to-RR and RR-to-TRR transition points found from experiments by Cohen [14].

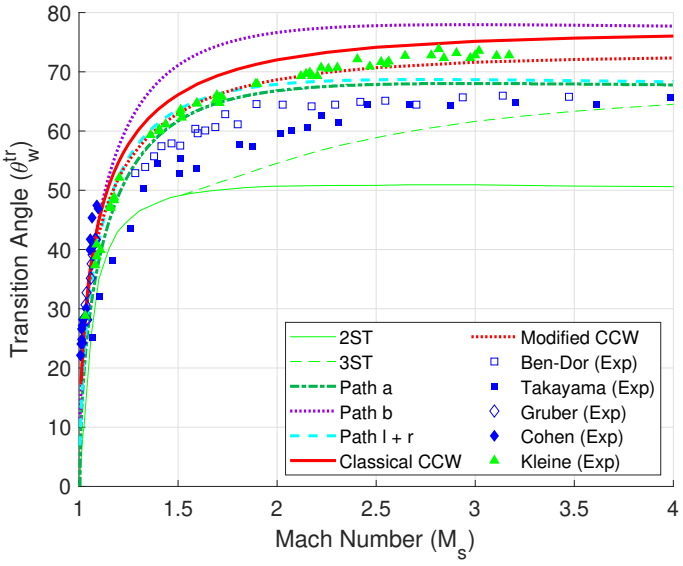

Fig. 3.5 The predicted transition angle, $\theta_{\mathrm{w}}^{\mathrm{tr}}$, plotted with M_{s}, based on the on the various experiment results obtained in this study [14][19][20][22][23] and previously obtained analytical predictions.

The data for the transition to TRR, the filled red squares in Figure 3.4, is compared with the previous methods used to find this transition point in Figures 3.5 and 3.6. For these weak shocks, the transition point to the TRR configuration produces data close to

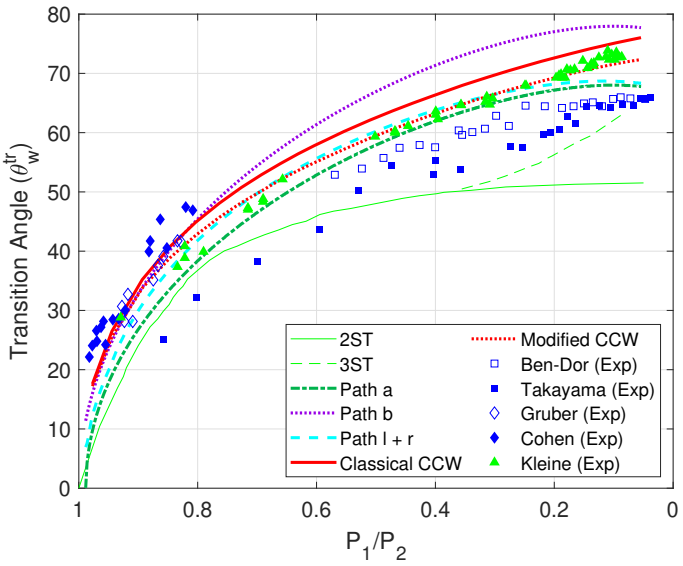

Fig. 3.6 The predicted transition angle, θ_w^{tr}, plotted with the inverse pressure ratio, based on the on the various experiment results obtained in this study [14][19][20][22][23] and previously obtained analytical predictions.

the data from Kleine [22]. It is important to note, however, that obtaining high accuracy experimental results of the transition points for weak shocks is still difficult due to poor optical resolution [14][23].

3.5 Conclusion

This chapter covered previous experiments used to predict the InMR-to-TRR transition point. Section 3.2 discussed two older experiments by Ben-Dor and Takayama (1980) [19] and Takayama and Sasaki [20]. These experiments provided results with poor accuracy due to low optical resolution. Therefore, small Mach stems could not be resolved. Section 3.3 discussed the results by Kleine (2018) [21] [22] which attempted to alleviate the issues from earlier experiments by using a larger radius of curvature in experiments and using better measurement devices. Finally, Section 3.4 presented some weak shock results by Gruber

[23] and Cohen [14]. These results are shown in Figures 3.5 and 3.6.

The experiment results from Kleine [22] predict higher transition angles than from the early experiments dealing with poor optical resolution. Furthermore, both weak shock experiment [14][23] results agree with the limited weak shock data from Kleine.

Further comparisons of the transition angle will continue in Chapter 4 for Computational Fluid Dynamics (CFD) and in Chapter 5 for Geometric Shock Dynamics (GSD).

Chapter 4

Computational Fluid Dynamics

While Chapter 2 focused on analytical predictions [16] [18] and Chapter 3 focused on experiments [14] [19] [20] [23] [21] [22], this Chapter 4 will focus on using Computational Fluid Dynamics (CFD) in order to predict the InMR-to-TRR transition angle $\theta_{\mathrm{w}}^{\mathrm{tr}}$. First, previous results obtained using numerical simulations will be discussed. Then the CFD results obtained using an in-house CFD solver called Masterix will be presented.

4.1 Previous Numerical Studies

Numerical studies performed by Taieb (2010) [24] and Koronio (2020) [15] are discussed in this section. Both numerical techniques, WENO and ANSYS FLUENT, are different than the Masterix flow solver used in this thesis. The results of both studies are included in Figures 4.6 and 4.7 as purple circles (Taieb) and stars (Koronio). Overall, the limited data collected by Taieb and Koronio corresponds quite well with the CFD results found using Masterix.

4.1.1 Taieb

Taieb [24] found the InMR-to-TRR transition angle with in-house code using the WENO method. The symmetric reflecting surface shown in Figure 4.1 is the shape used in this study. However, because of the symmetry, only half of the reflecting surface is needed for numerical calculations.

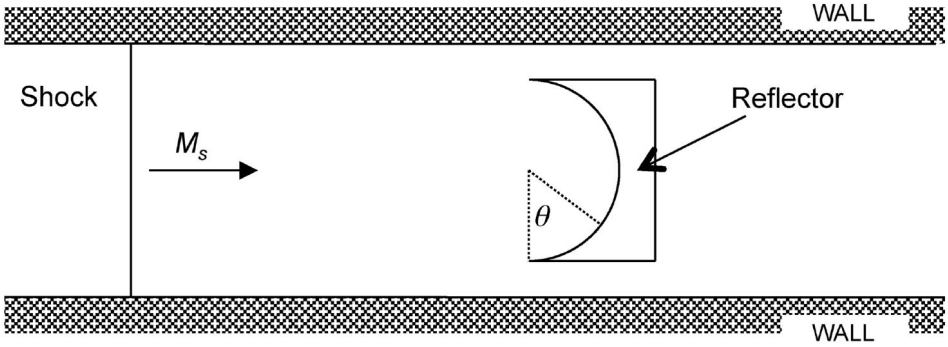

Fig. 4.1 A schematic of the reflecting surface analyzed in this numerical study. The schematic is taken from [24].

Taieb found the predicted transition angles (tabulated in Table 4.1) with accuracy of $\pm 1^o$ [24]. Figures 4.6 and 4.7 show the four data points from Table 4.1 plotted as purple circles to compare with other methods.

Table 4.1 Tabular data of the InMR-to-TRR transition point found using the in-house WENO code by Taeib [24].

$\theta_{\mathrm{w}}^{\mathrm{tr}}$	$M_{\mathrm{s}} = 1.38$	$M_{\mathrm{s}} = 1.8$	$M_{\mathrm{s}} = 2.0$	$M_{\mathrm{s}} = 3.0$
WENO	60.37^o	66.68^o	69.57^o	73.58^o

4.1.2 Koronio

Koronio [15] found the InmR-to-TRR transition angle using a commercial solver, ANSYS FLUENT technique. The scheme used to approximate the inviscid Euler equations was second-order in space and time. The numerical predictions were calculated with:

- Three different reflecting surface radii, R: 40 mm, 60.6 mm and 100 mm.
- Three different Mach numbers, M_s: 1.3, 1.4 and 1.5.
- Three different gases: Air ($\gamma = 1.4$), argon ($\gamma = 1.67$) and CO_2 ($\gamma = 1.28$).

This study confirmed the radius of curvature had no effect. The transition angle for each Mach number propagating through air is tabulated in Table 4.2. Koronio [15] was able to show good correlation between the numerical results and experiments. The three data points from Table 4.2 are plotted in Figures 4.6 and 4.7 as purple stars.

Table 4.2 Tabular data of the InMR-to-TRR transition point (in air) found using ANSYS FLUENT by Koronio [15].

θ_w^{tr}	$M_s = 1.3$	$M_s = 1.4$	$M_s = 1.5$
ANSYS	57.5^o	61.0^o	63.3^o

4.2 Introduction to Masterix

Masterix is an adaptive unstructured finite-volume Euler code. It uses a second-order in accuracy, for space and time, node-centered MUSCL-Hancock TVD flow solver [34]. For these CFD computations, it is assumed that the flow is inviscid and non-heat conducting. The governing equation for the conservation law is given as follows:

$$\frac{\partial \mathbf{U}}{\partial t} + \frac{\partial \mathbf{F}}{\partial x} + \frac{\partial \mathbf{G}}{\partial y} = 0 \tag{4.1}$$

Where $\mathbf{U}$ is a vector of conserved quantities, $\mathbf{F}$ is the flux in the $x-$direction direction and $\mathbf{G}$ is the flux in the $y-$direction. These three vectors are given by:

$$\mathbf{U} = \begin{bmatrix} \rho \\ \rho u \\ \rho v \\ \rho e \end{bmatrix} \qquad \mathbf{F} = \begin{bmatrix} \rho u \\ \rho u^2 + p \\ \rho uv \\ (\rho e + p)u \end{bmatrix} \qquad \mathbf{G} = \begin{bmatrix} \rho v \\ \rho uv \\ \rho v^2 + p \\ (\rho e + p)v \end{bmatrix} \tag{4.2}$$

Where ρ is density, u is velocity in the $x-$direction, v is the velocity in the $y-$direction, p is pressure and e is the energy.

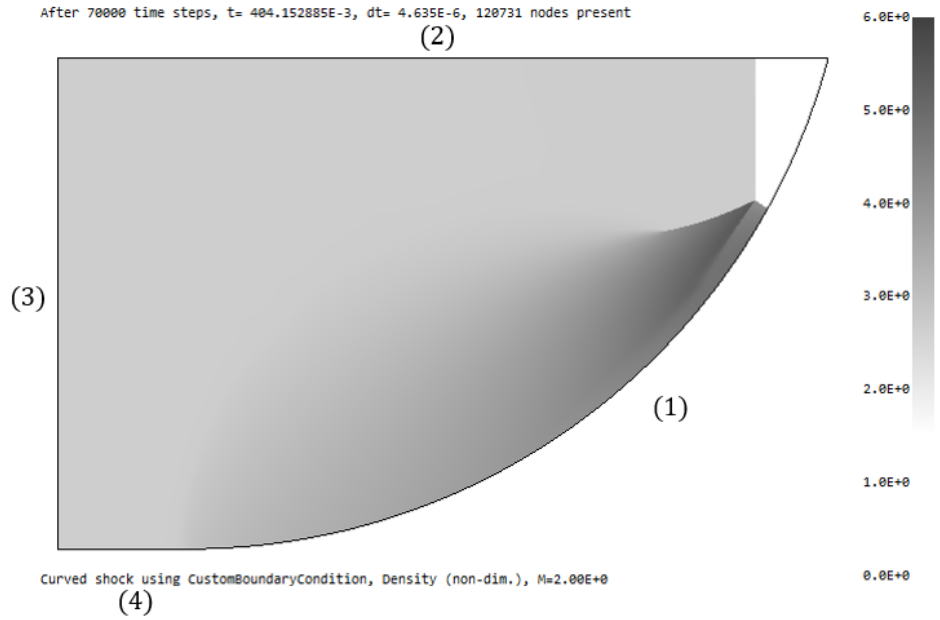

Fig. 4.2 The computational domain used in Masterix to find the InMR-to-TRR transition point. The Boundary Conditions are: (1) Concave Cylindrical Surface, (2) and (4) Walls and (3) Dirichlet B.C.s for the inflow.

An example visualization of the computational domain in Masterix is shown in Figure 4.2. In this example, the non-dimensional density is visualized, which allows for the incident shock, reflected shock, Mach stem and slip stream to be seen. The boundary conditions used for this CFD analysis are:

- (1) Concave cylindrical reflecting surface, acting as a wall.
- (2) and (4) Walls.
- (3) Dirichlet boundary conditions for the inflow.

Boundary (1) has a radius of curvature of $R = 1$ and spans from $\theta = 0^o$ to $\theta = 75^o$. The boundary was capped at 75^o to decrease the computational time, knowing the transition angle for the Mach numbers chosen to study would less than 75^o. Boundary (2) spans from $x = 0.966$ to $x = -0.1$. Boundary (3) spans from $y = 0.741$ to $y = 0$. Boundary (4) spans from $x = -0.1$ to $x = 0$. The computational domain is discretized using an unstructured mesh with triangular elements. A discussion on the mesh discretization is available in Section 4.4.

For the problem setup, the shock wave is initially placed at $x = -0.05$ and propagates with an initial Mach number M_s. Once the normal shock reaches $x = 0$, the reflection will begin to occur. A triple point will begin to form eventually resulting in an Inverse Mach Reflection (InMR) appearing. The shock will continue to propagate until the Mach stem disappears (at $\theta_\mathrm{w}^\mathrm{tr}$) and then a Transitioned Regular Reflection (TRR) will form.

4.3 CFD Example

As an example, the problem with $M_\mathrm{s} = 2$ is shown. Some screenshots of the computations in Masterix are shown in Figure 4.3. The colour coding refers to non-dimensional density.

Figure 4.3 (a) shows the initial shock wave with $M_\mathrm{s} = 2$. In this case, since reflection has not yet occurred, solving the flow parameters behind the shock wave would be simple. By changing the frame of reference and applying the Rankine-Hugoniot relations (Equations 1.1 to 1.4), the flow parameters behind the normal shock wave can be found.

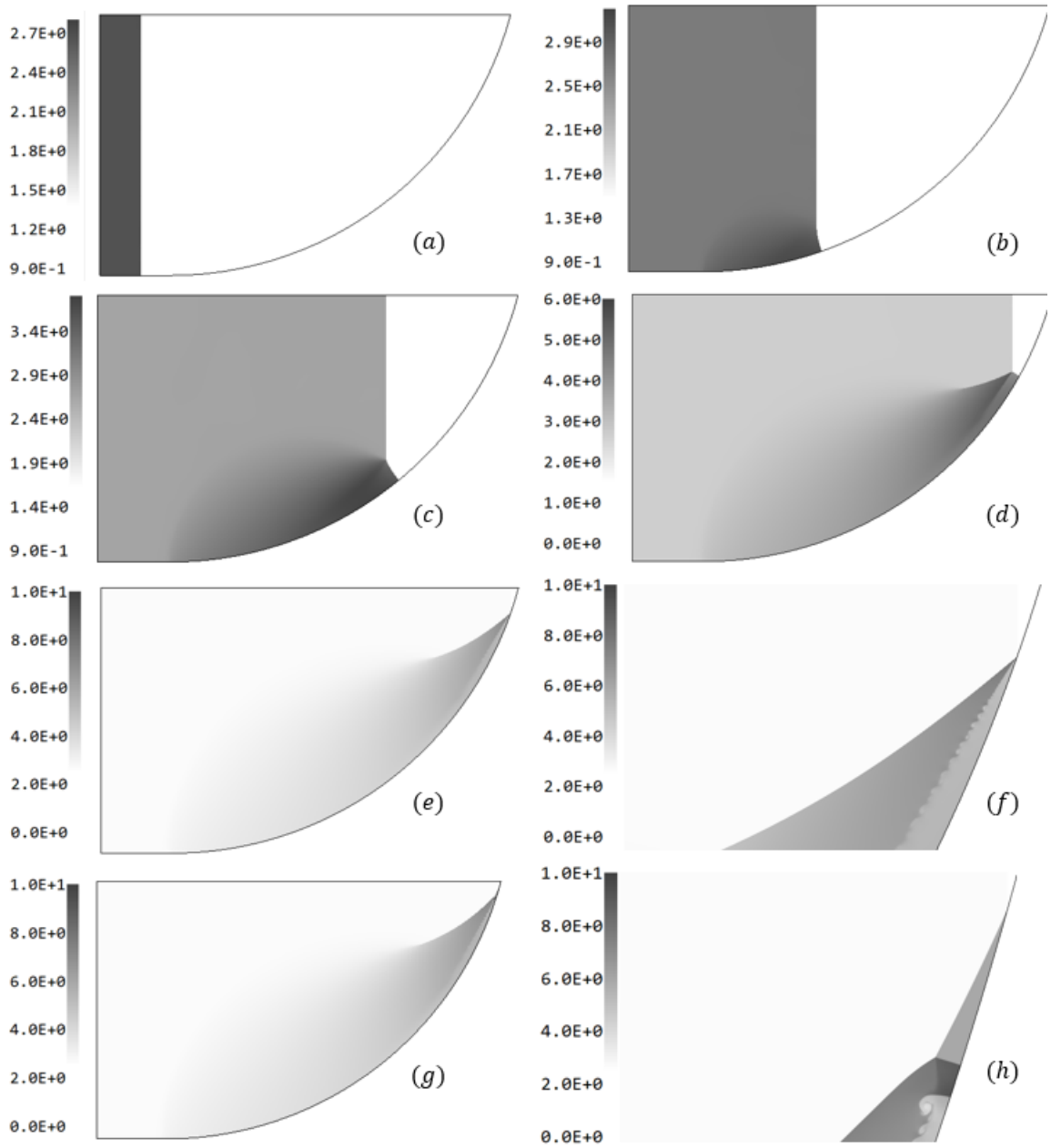

Fig. 4.3 Masterix Visualizations with density colour coded. (a) The initial normal shock wave ($M_s = 2$). (b) The IR without a well-defined triple point. (c) A MR with a well-defined Mach stem and reflected shock wave. (d) An InMR with a well-defined triple point and a visible slip stream. (e) The transition point from InMR-to-TRR. (f) A magnified view of the transition point. (g) Transitioned Regular Reflection (TRR). (h) Magnified view of TRR.

Some time later, an ill-defined triple point can be seen in Figure 4.3 (b). For the reflection at this low wedge angle, Vasilev [8] suggests that this may be a vNR/GR/VR. Cohen [14] later calls this configuration a Compressive Reflection (CR). In Figure 4.3 (c), the triple point becomes better defined as the shock continues to propagate. At this stage, the reflected wave and Mach stem are both easily discernible.

In Figure 4.3 (d), the Inverse Mach Reflection has all its characteristics visible. The 3 shocks (incident, reflected and Mach stem) and the slip stream can all be seen meeting at the triple point. Once the transition point is reached (Figure 4.3 (e) and (f)), $\theta_{\mathrm{w}}^{\mathrm{tr}}$ can be found. In this case for $M_{\mathrm{s}} = 2$, $\theta_{\mathrm{w}}^{\mathrm{tr}} = 70.8^{o}$. At this transition point, there is still a reflected shock wave and a slip stream, but the Mach stem has disappeared. After the transition point, the Transitioned Regular Reflection (TRR) forms (Figure 4.3 (g) and (h)).

The results shown in Figure 4.3 are based on the most refined mesh used for this study. A grid convergence study is demonstrated for $M_{\mathrm{s}} = 2$ in Section 4.4. Full results for various Mach numbers are provided in Section 4.5.

4.4 Grid Convergence

When using CFD, discretizing the domain is important because the mesh chosen to solve the problem will influence the solution. Therefore, there is a need to find a grid-independent solution for the transition angle.

The baseline mesh with zero refinement is a triangular mesh with grid spacing of $l_0 = 0.05$. Subsequent levels of grid refinement result in data point spacing of:

$$l = \frac{l_0}{2^{Level}}; \qquad l_0 = 0.05 \tag{4.3}$$

4.4.1 Mesh Selection

Each computation has two associated grid sizes, called Min Level and Max Level. The Max level is associated with the mesh at the shocks and slip stream. These locations are identified where there is a jump between the density of two data points of ±2% or more. The Min level corresponds to the region behind the reflected wave and Mach stem. The mesh behind the incident shock wave stays at level 0 as the flow parameters do not vary in this region. For the same reason, the mesh of the undisturbed flow stays at level 0 as well. Four example meshes are provided in Figure 4.4.

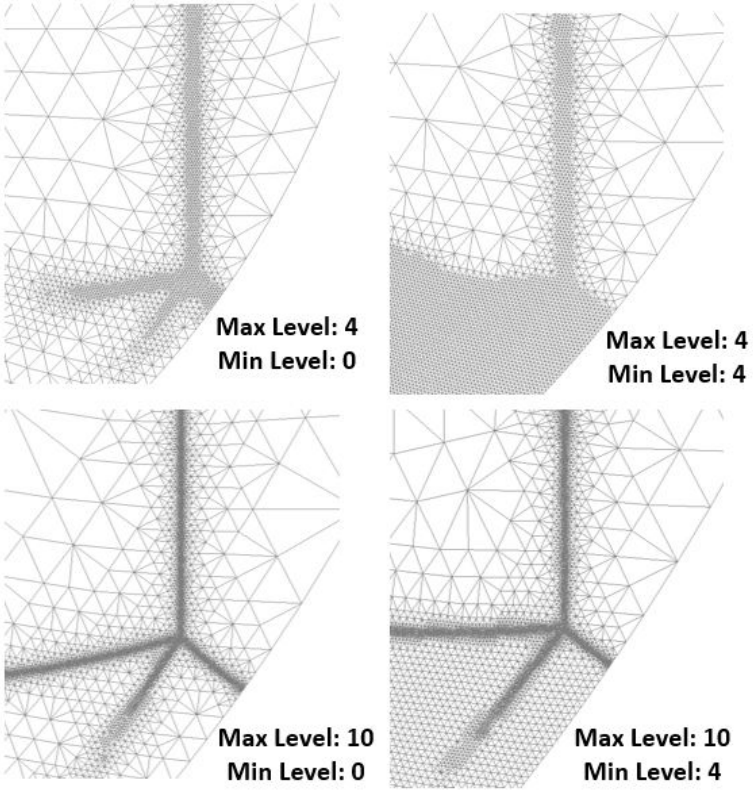

Fig. 4.4 Extremes of the meshes selected for the grid convergence study.

Different meshes have provided different result for the InMR-to-TRR transition angle. For instance, for the mesh with Max level of 4 and Min level 0 (with $M_s = 2.0$), the

transition angle is predicted to be $\theta_{\mathrm{w}}^{\mathrm{tr}} = 68.8^{o}$ while the transition angle predicted for Max level 10 and Min level 4 is $\theta_{\mathrm{w}}^{\mathrm{tr}} = 70.8^{o}$. In order to obtain a grid-independent solution, a grid-convergence study is performed.

4.4.2 Richardson Extrapolation

In order to find the grid-independent solution, various meshes are chosen for the same $M_{\mathrm{s}} = 2$. The meshes will vary from Max level of 4 up to 10 and Min level of 0 up to 4. A Max level of 10 is the limit selected due to excessive computational time and a Min level of 4 is the limit due to the limits on computer memory and computational power.

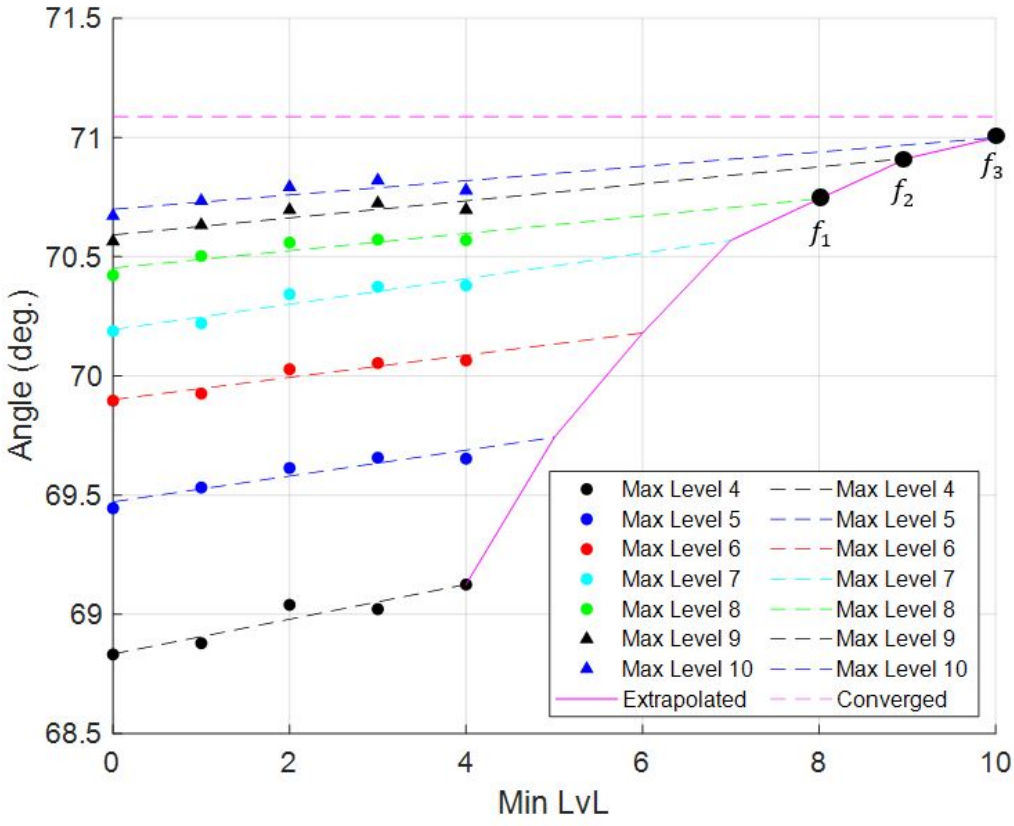

Fig. 4.5 Grid Convergence Study for $M_s = 2$.

The transition points for each mesh were found and plotted in Figure 4.5. For each

Max Level $4, 5, ..., 10$, the transition angle for the Min Level mesh ranging from 0 to 4 was obtained. A simple linear extrapolation was done up to Min Level equalling Max Level. Once each extrapolated value was calculated for Max Level 4 to 10, a Richardson extrapolation [35] was performed on the final three data points (i.e. Max Level 8, 9 and 10). The Richardson extrapolation is as follows:

$$\tilde{f}_{exact} = f_1 - \frac{\epsilon_{21}}{r_{12}^{\tilde{p}} - 1} \tag{4.4}$$

$$\tilde{p} = \frac{\ln(\epsilon_{32}/\epsilon_{21})}{\ln(r)} \tag{4.5}$$

$$r_{12} = \frac{l_2}{l_1} \tag{4.6}$$

$$\epsilon_{21} = f_2 - f_1 \tag{4.7}$$

$$\epsilon_{32} = f_3 - f_2 \tag{4.8}$$

Where $\tilde{f}_{exact}$ refers to grid-independent solution, f_1, f_2 and f_3 are the linear extrapolated values for Max level 8, 9 and 10 respectively and l is the grid spacing. By using exponents of 2, $r_{12} = 0.5$ in this case.

Using the data from Figure 4.5, the Richardson extrapolation gives $f_{exact} = \theta_{\mathrm{w}}^{\mathrm{tr}} = 71.1^o$. Considering a transition angle predicted from section 4.3 under-predicts the transition angle as 70.8^o, then the difference between the grid-independent solution and the most refined mesh chosen is 0.3^o.

4.5 CFD Results

The results using Masterix are provided in Figures 4.6 and 4.7. Some of these Masterix results came from this study, while others came from Previtali [21][22]. The solutions shown are not the grid-independent solutions as discussed in section 4.5. Instead, transition angles shown in magenta are the results of using Max level 10, and Min level 4. The error bars are not shown because they are smaller than the data points used to plot the figure.

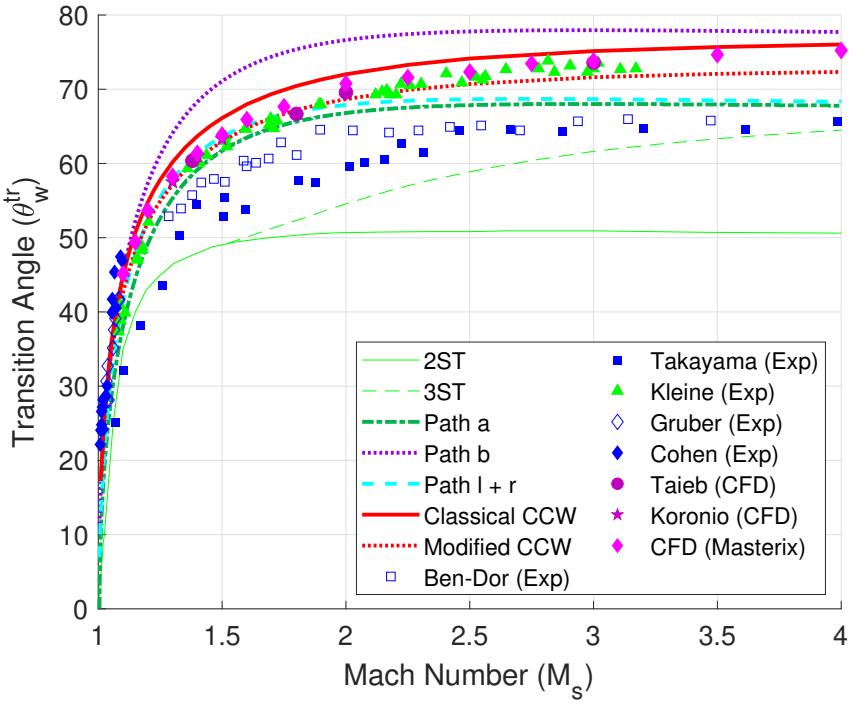

Fig. 4.6 The transition angles found using the current CFD from Masterix [25], and past numerical results from Taieb [24] and Koronio [15] with previously obtained analytical predictions and experiment results.

The Masterix CFD results in Figures 4.6 and 4.7 (magenta diamonds), in general, agree with the recent experiment results. On average, the CFD results predict about 1^o higher than the recent experiment results by Kleine [22]. Considering the new experiment results are still suggested to under-predict the transition point [21] due to insufficient optical

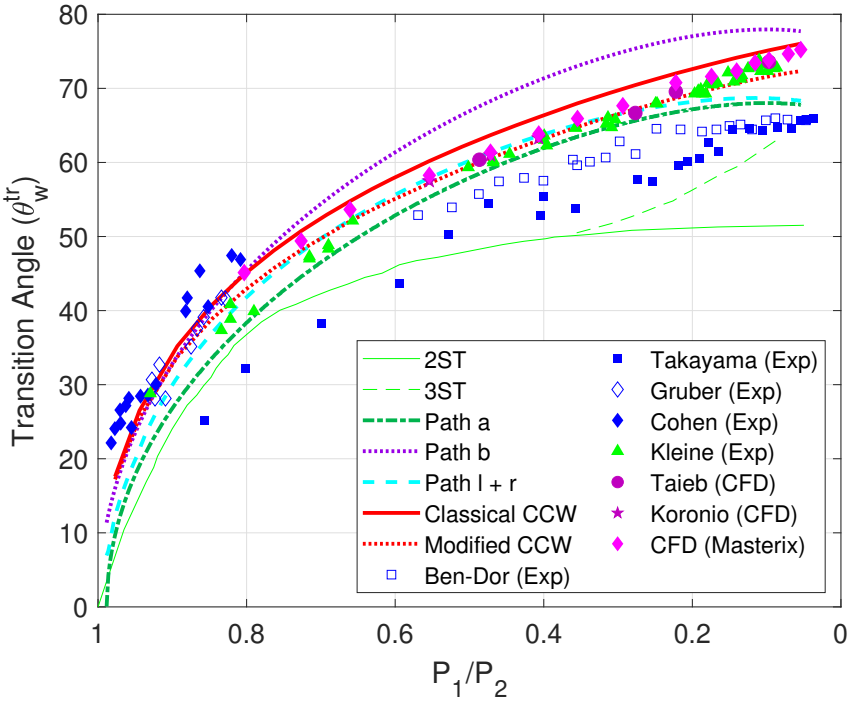

Fig. 4.7 The transition angles found using the current CFD from Masterix [25], and past numerical results from Taieb [24] and Koronio [15] with previously obtained analytical predictions and experiment results.

resolution and some lingering viscous effects, then the CFD predictions can now be seen as the most accurate results for finding the InMR-to-TRR transition point.

The CFD results with Masterix can also be compared with the numerical results from Taieb [24] and Koronio [15]. Table 4.3 tabulates the common Mach numbers studied. The current and previous numerical results compare favorably with each other.

Table 4.3 Tabular data of the InMR-to-TRR transition point found using numerical techniques by Taieb [24], Koronio [15] and Masterix [25].

θ_w^{tr}	$M_s = 1.3$	$M_s = 1.4$	$M_s = 1.5$	$M_s = 2.0$	$M_s = 3.0$
Masterix	58.3^o	61.4^o	63.9^o	70.8^o	73.8^o
Taieb	-	-	-	69.6^o	73.6^o
Koronio	57.5^o	61.0^o	63.3^o	-	-

4.6 Conclusion

This chapter focused on using Computational Fluid Dynamics (CFD) to find the InMR-to-TRR transition point over a concave cylindrical surface. First, the results obtained by Taeib [24] using an in-house WENO method and the results obtained by Koronio [15] using a commercial software, ANSYS FLUENT, are described in Section 4.1. Then, the in-house CFD flow solver Masterix [25] is introduced in Section 4.2. An example using $M_s = 2$ was shown in Section 4.3 showing each aspect of the problem statement, from the initial normal shock to the formation of the InMR, to the transition point and finally becoming a TRR. A grid-convergence study is performed in Section 4.4 to obtain a grid-independent solution for the transition point.

The results from the CFD solver for Mach numbers ranging from $M_s = 1.1$ to $M_s = 4$ with the most refined mesh are shown in Figures 4.6 and 4.7. Overall, the results obtained using CFD techniques correspond quite well with the most recent experiment results (section 3.3).

Chapter 5 discusses the use of Geometric Shock Dynamics (GSD) to find the InMR-to-TRR transition angle. Chapter 6 provides further comparisons of the various methods used to predict the transition point.

Chapter 5

Geometric Shock Dynamics

5.1 Introduction to Geometric Shock Dynamics (GSD)

While Chapter 4 focused on using Computational Fluid Dynamics (CFD) as a numerical method for finding the InMR-to-TRR transition angle, this chapter focuses on a different numerical method - Geometric Shock Dynamics (GSD). GSD was first described by Whitham [32][36][37] in 1957. Based on his work, GSD was capable of estimating the shock reflections of various geometries with lower computational time, compared to CFD techniques, while still maintaining accuracy [33].

Unlike CFD, where the gasdynamic equations are solved directly based on flow properties (see Chapter 4), in GSD, the motion of the shock is found by directly relating the local geometry with the local Mach number [38]. The geometry of the shock front is estimated without calculating the flow field behind. This decreases the computational time when compared with CFD techniques with similar grid sizes. The decrease in time would become even more evident when solving 3-D problems. It is for this reason that GSD must be studied despite knowing CFD techniques can provide accurate predictions for the

InMR-to-TRR transition point.

For sustained shock propagation problems, GSD has been shown to be accurate [33] [39] [40]. In these examples, the geometry was converging, just like the problem statement of this thesis. However, the original GSD has limitations. For convex geometries with sufficiently weak shocks, there is no solution for the entire shock front up to the reflecting surface. Ridoux [33] proposes an additional transverse term for these expansive waves to resolve the entire shock front. Ridoux refers to this as GSDT (GSD Transverse). Because this transverse term only exists for convex geometries, and the problem statement for InMR-to-TRR transition is a concave geometry, the numerical scheme will simply be referred to as GSD.

The basis of GSD is to introduce rays (orthogonal trajectories for successive positions of the shock) based on the geometry the shock encounters. Figure 5.1 shows how these rays are built. The change in area of each ray tube, caused by the local curvature, links with the shock wave velocity in what is known as the $A - M$ rule. The scheme used for this research is based on the work done by Ridoux [33].

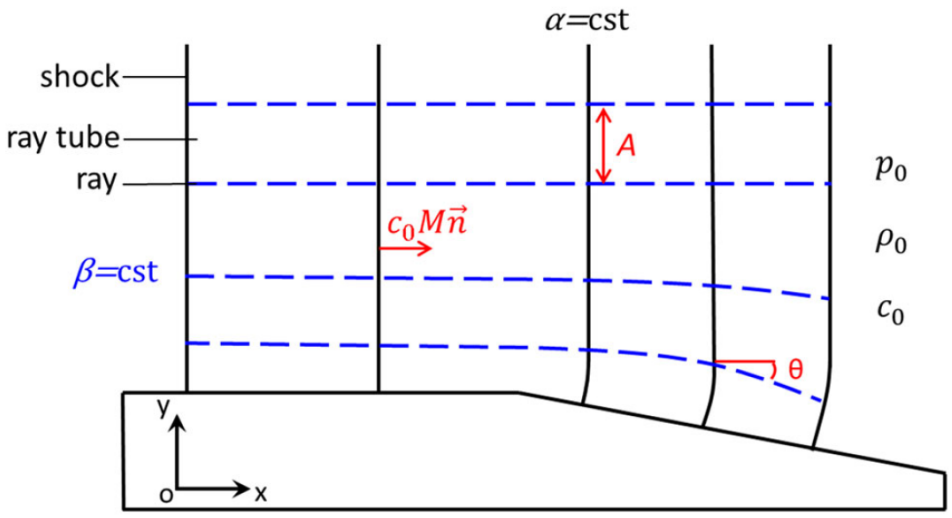

Fig. 5.1 Schematic for 2D shock propagation using GSD taken from [33].

Section 5.2 derives the $A - M$ Rule used in GSD. Section 5.3 provides a very detailed description of the numerical scheme used in these studies. This numerical scheme is based on the work done by Ridoux [33]. The results for finding the InMR-to-TRR transition angle with GSD are presented in Sections 5.4 and 5.6.

5.2 Derivation of GSD

GSD [33] is based on splitting the shock front into elementary areas, A, using rays as seen in Figure 5.1. The method of creating these areas allows for cross flow to be neglected which reduces the problem to a quasi-1D problem of a planar shock with varying area propagating through a channel. Each successive shock front location is provided by the $\alpha = cst$ lines while the $\beta = cst$ are perpendicular to the shock front as seen in Figure 5.1.

The coordinate α and time t are related using $\alpha = c_0 t$ where $c_0 = \sqrt{\frac{\gamma p_0}{\rho_0}}$. The following geometric relations are for the local coordinates of the shock front.

$$\frac{\partial \theta}{\partial \beta} - \frac{1}{M}\frac{\partial A}{\partial \alpha} = 0 \tag{5.1}$$

$$\frac{\partial \theta}{\partial \alpha} + \frac{1}{A}\frac{\partial M}{\partial \beta} = 0 \tag{5.2}$$

The curvilinear abscissa along the shock s is given by:

$$\mathrm{d}s = A\mathrm{d}\beta \tag{5.3}$$

By assuming each ray tube to be a channel with solid walls, the $A - M$ rule can be used to link the area and Mach number. This $A - M$ rule is derived from the 1D Euler System

with varying cross-section and was described by Best [41]:

$$\frac{1}{A}\frac{\mathrm{d}A}{\mathrm{d}\alpha} + \frac{M\lambda(M)}{M^2-1}\frac{\mathrm{d}M}{\mathrm{d}\alpha} + h(M)Q = 0 \tag{5.4}$$

$$\lambda(M) = \left(1 + \frac{2}{\gamma+1}\frac{1-\mu^2}{\mu}\right)\left(1 + 2\mu + \frac{1}{M^2}\right) \tag{5.5}$$

$$\mu = \sqrt{\frac{(\gamma-1)M^2+2}{2\gamma M^2+1-\gamma}} \tag{5.6}$$

$$h(M) = \frac{\gamma+1}{2}\frac{\mu(\mu-1)}{M^2-1} \tag{5.7}$$

$$Q = \frac{(\partial_t p + \rho c \partial_t v)_-}{p_0 c_0^3} \tag{5.8}$$

Whitman neglected $h(M)$ in Equation 5.4 which results in the following modification:

$$\frac{1}{A}\frac{\mathrm{d}A}{\mathrm{d}\alpha} + \frac{M\lambda(M)}{M^2-1}\frac{\mathrm{d}M}{\mathrm{d}\alpha} = 0 \tag{5.9}$$

Equation 5.9 is known as the $A-M$ Rule. It has been shown that neglecting the term $h(M)$ still provides accurate predictions for certain shock wave reflections [33][42]. Area A is only a function of M:

$$A(M) = \exp\left(-\int_{M_0}^{M}\frac{m\lambda(m)}{m^2-1}\mathrm{d}m\right) \tag{5.10}$$

Due to the fact that GSD is a hyperbolic system, based on the geometric relations for the local coordinates in Equation 5.1 and 5.2, some waves may develop along the shock front. These perturbations travel with velocity:

$$\frac{A\mathrm{d}\beta}{\mathrm{d}\alpha} = \pm Au(M) = \pm A(M)u(M) = \sqrt{\frac{M^2-1}{\lambda(M)}} \tag{5.11}$$

These perturbations are responsible for the modification of the shock front. The equations to express the Cartesian coordinates (x, y) from the local coordinates (α, β) is:

$$\begin{aligned} \frac{\partial x}{\partial \alpha} &= M\cos\theta; & \frac{\partial y}{\partial \alpha} &= M\sin\theta; \\ \frac{\partial x}{\partial \beta} &= -A\sin\theta; & \frac{\partial y}{\partial \beta} &= A\cos\theta; \end{aligned} \tag{5.12}$$

Ridoux [33] studied GSD and discovered a limitation in the GSD model for expansive waves over convex surfaces. In order to take into account the transverse flow in Whitham's $A-M$ Rule, a modification is proposed in order to remove the limitation of the GSD model for all expansive shocks over convex surfaces while not affecting compressive waves over concave surfaces. Ridoux [33] proposed the following ad hoc modification to Whitham's $A-M$ relation by taking into account the variation of the Mach number along the shock front with respect to the curvilinear abscissa s. Equation 5.9 can be modified to:

$$\frac{1}{A}\frac{\mathrm{d}A}{\mathrm{d}\alpha} + \frac{M\lambda(M)}{M^2-1}\frac{\mathrm{d}M}{\mathrm{d}\alpha} + H(\kappa)f(M)\left|\frac{\partial M}{A\partial\beta}\right| = 0 \tag{5.13}$$

The function f is defined as the following:

$$f(M) = \frac{k\lambda(M)}{2} - \frac{2M^2}{k(M^2-1)}, k = 0.985 \tag{5.14}$$

κ is the curvature of the shock front. Because this ad hoc modification is only required for expansive waves, the function H is used:

$$H(\kappa) = \begin{cases} 0 & \text{if } \kappa \leq 0 \\ 1 & \text{if } \kappa > 0 \end{cases} \tag{5.15}$$

Therefore, for finding the InMR-to-TRR transition point, $H(\kappa \leq 0) = 0$. Thus the extra transverse term can be ignored and simply using GSD with the $A - M$ rule of Equation 5.9 would be sufficient. However, for the purpose of completeness, to be able to apply the developed GSD code to any geometry, the full GSDT $A - M$ rule of Equation 5.13 will be used to write the numerical scheme in Section 5.3.

5.3 GSD Numerical Scheme

The numerical scheme used to solve for the shock front is based on the work provided by Ridoux [33]. The GSD model improves on that of Henshaw [38] by managing the number of data points on the shock front by adding points for expansive waves to maintain a fine mesh and removing points from compressive waves to avoid intersecting rays. Furthermore, in the original scheme, the shock front was interpolated using a cubic spline to estimate the unit normal vectors. But Ridoux has suggested to use a local monotone cubic spline [43] to avoid oscillations. The final major change to the GSD model by Ridoux is the use of a total variation diminishing (TVD) third-order Runge-Kutta scheme to propagate the shock wave to each subsequent time step.

Consider an initial shock front, at time α_0, often taken to be equal to 0. The shock front has the following Cartesian coordinates where the variable X is two-dimensional:

$$X(\alpha_0, \beta) = \begin{bmatrix} x(\alpha_0, \beta) \\ y(\alpha_0, \beta) \end{bmatrix} \tag{5.16}$$

The Mach number along the shock front is initialized:

$$M_0 = M(\alpha_0, \beta) \tag{5.17}$$

Let N be the number of points in the initial shock front such that $(\beta)_{i=1,...,N}$ is the discretization of the β coordinate. The shock front at any time $\alpha \geq \alpha_0$ is approximated using a finite set of points:

$$X(\alpha, \beta_i) = X_i(\alpha) = \begin{bmatrix} x_i \\ y_i \end{bmatrix}_{i=1,...,N} \tag{5.18}$$

Equation 5.3 links the the curvilinear abscissa s and the β coordinate. Discretizing s along the shock:

$$s_i = \begin{cases} 0 & \text{if i = 1} \\ s_{i-1} + \|X_i - X_{i-1}\| & \text{if i = 2,...,N} \end{cases} \tag{5.19}$$

With $\|X\| = \sqrt{x^2 + y^2}$. Also, $\Delta s_i = s_i - s_{i-1}$ for $i = 2, ..., N$ and its initial shock discretization will be uniform:

$$\Delta s = \frac{1}{N} \sum_{i=2}^{N} (s_i(\alpha_0) - s_{i-1}(\alpha_0)) = \frac{s_N \alpha_0}{N} \tag{5.20}$$

Using Figure 5.2, it can be seen that each point $X_i(\alpha)$ has an associated ray tube area A_i and a local Mach number $M_i(\alpha)$. The unit normal vector, outwards from point X_i is labelled as $n_i(\alpha)$. The position of the shock front is the solution to the following ODE:

$$\frac{\mathrm{d}X}{\mathrm{d}t} = c_0 M n \tag{5.21}$$

Using this information, the data points, X_i are moved one time step further by integrating Equation 5.21 in the α coordinate system, remembering $\alpha = c_0 t$:

$$\frac{\mathrm{d}X_i}{\mathrm{d}\alpha} = M_i n_i \quad \text{for } i = 1, ..., N \tag{5.22}$$

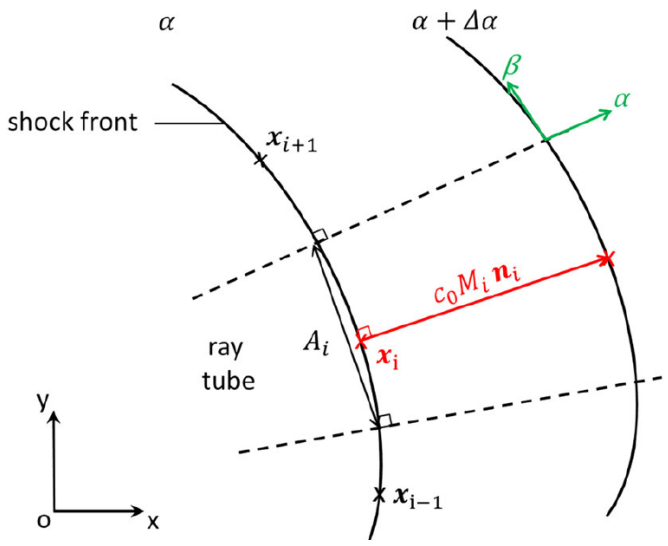

Fig. 5.2 Schematic of the shock front discretization for GSD taken from [33].

The ODE 5.22 is integrated using a TVD third-order Runge-Kutta scheme with the following three steps:

$$X_i^{(1)} = X_i(\alpha) + \Delta\alpha M_i(\alpha) n_i(\alpha) \tag{5.23}$$

$$X_i^{(2)} = \frac{3}{4} X_i(\alpha) + + \frac{1}{4} X_i^{(1)} + \frac{\Delta\alpha}{4} M_i^{(1)} n_i^{(1)} \tag{5.24}$$

$$X_i(\alpha + \Delta\alpha) = \frac{1}{3} X_i(\alpha) + \frac{2}{3} X_i^{(2)} + \frac{2\Delta\alpha}{3} M_i^{(2)} n_i^{(2)} \tag{5.25}$$

The values for M_i and n_i are evaluated between each of these three steps. The details of this numerical scheme are described in Appendix A.2.

5.4 GSD Example Result

Using the GSD numerical scheme presented in section 5.3 with $M_\mathrm{s} = 1.6$, a visualization of the propagating shock wave is shown in Figure 5.3. Figure 5.4 (Left) shows a magnified shock front allowing each individual data point to be seen. From this figure, the incident shock wave, triple point and Mach stem can each be seen. The reflected shock wave is not

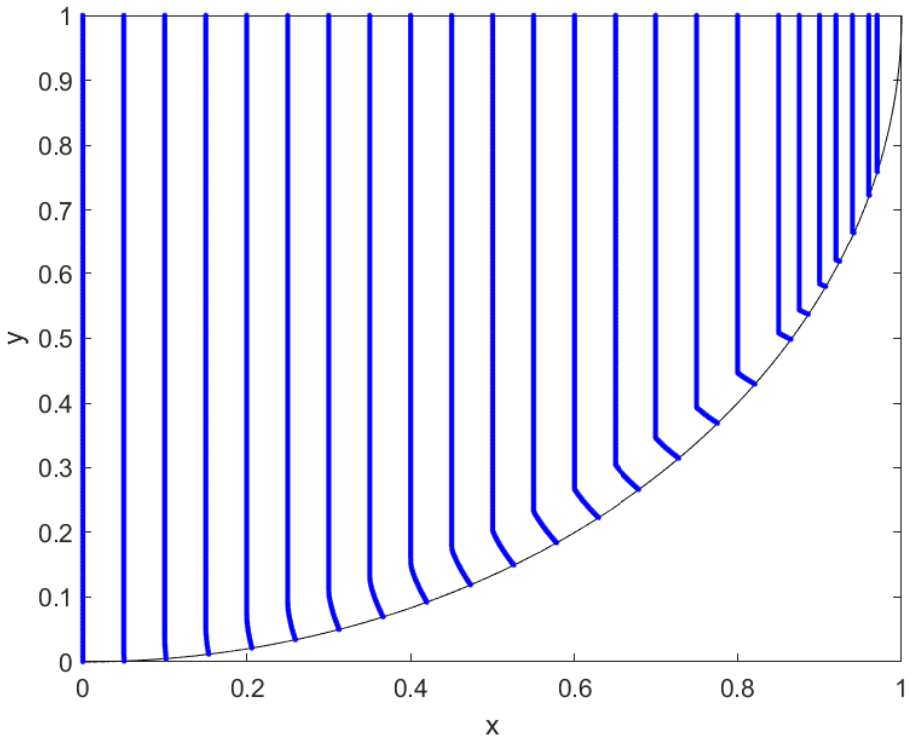

Fig. 5.3 A plot of the propagating shock using Geometric Shock Dynamics with $M_s = 1.6$ and an initial grid spacing of $dy = 0.0002$.

seen because GSD only calculates the shock front, and not the flow behind the shock.

The transition point, θ_w^{tr} with the GSD solution is found from Figure 5.4 (right). As can be seen, the transition point is determined when the Mach stem has just two data points remaining: the triple point and the foot of the Mach stem. This assumption is made because early numerical results showed that the Mach stem would never fully disappear along the concave reflecting surface. This observation was also noted by Peton [44] performing similar work.

Based on the data seen in Figure 5.4 (right), the transition point is found to be $\theta_w^{tr} = 76.0^o$ for $M_s = 1.6$ and $dy = 0.0002$. However, using a different mesh size resulted in a different solution. Therefore, a grid convergence study for GSD is shown in Section 5.5.

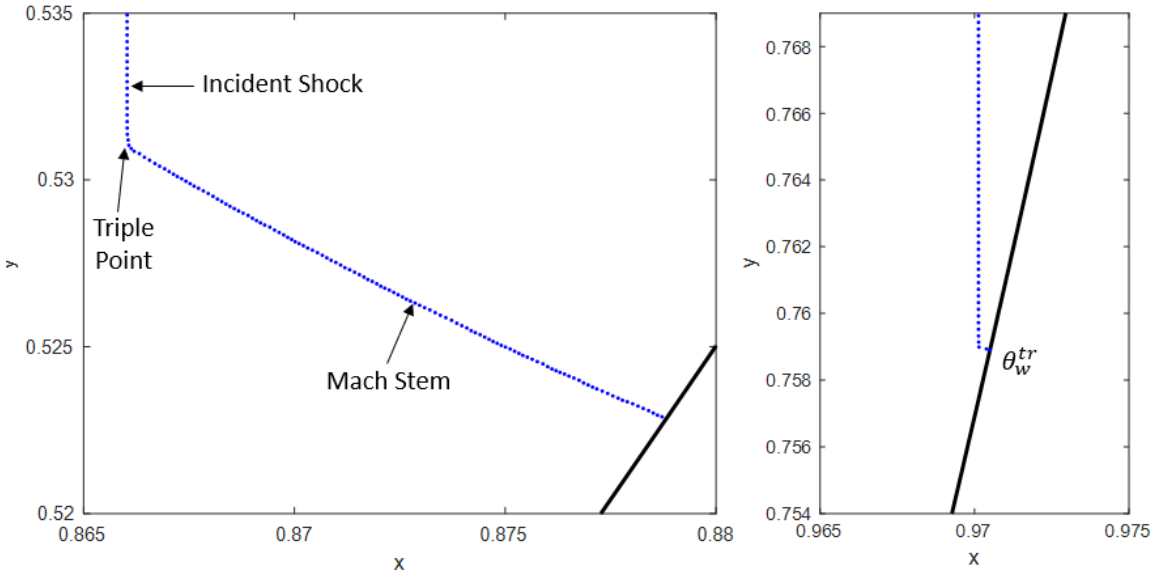

Fig. 5.4 **Left:** A magnified view of the InMR using GSD with θw $= 60^o$ ($x = 0.866$) for $M_\mathrm{s} = 1.6$ and d$y = 0.0002$. **Right:** The GSD solution for $\theta_\mathrm{w}^\mathrm{tr}$ with $M_\mathrm{s} = 1.6$ and d$y = 0.0002$.

5.5 GSD Grid Convergence

A grid convergence study was undertaken for finding the InMR-to-TRR transition angle using GSD. As can be seen in Figure 5.5, changing the mesh size significantly changes the transition angle. For example, using $M_\mathrm{s} = 1.6$, $\theta_\mathrm{w}^\mathrm{tr} = 71.3^o$ with d$y = 0.002$ and $\theta_\mathrm{w}^\mathrm{tr} = 76.0^o$ with d$y = 0.0002$. However, unlike the grid convergence for the CFD predictions (see section 4.4), a realistic converged value could not be found. Attempting Richardson extrapolations [35] at larger Mach numbers, $M_\mathrm{s} > 1.5$ provided a near constant transition angle of about $\theta_\mathrm{w}^\mathrm{tr} \approx 80^o$. Meanwhile, Richardson extrapolation for lower Mach numbers, $M_\mathrm{s} \leq 1.5$ resulted in a wide range of predictions with $\theta_\mathrm{w}^\mathrm{tr} > 80^o$. These extrapolated predictions, especially for lower Mach numbers, are significantly higher than all previously obtained transition points. Due to the lack of grid-independent GSD predictions, the data is Figure 5.7 is presented with three different mesh sizes is included.

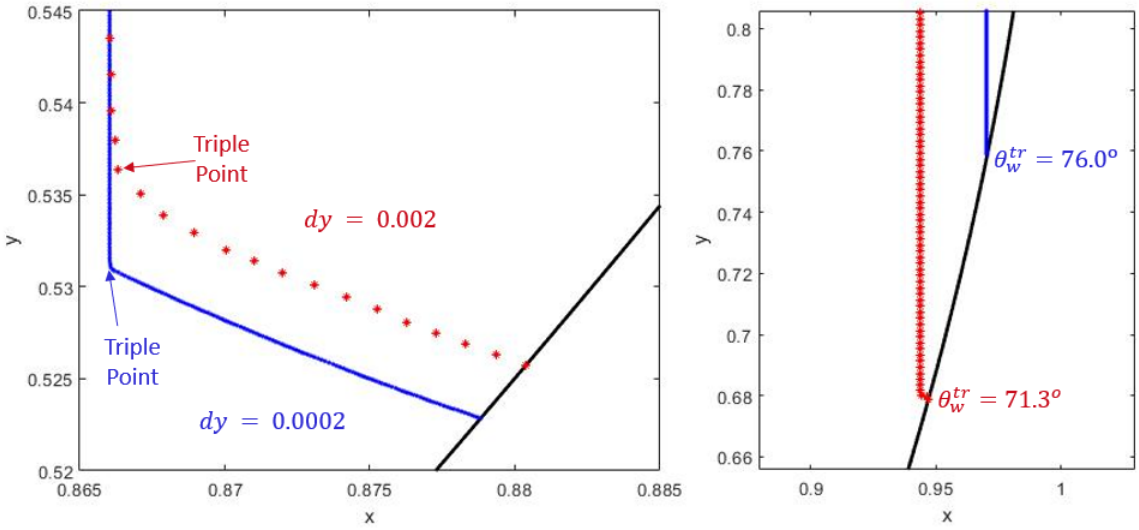

Fig. 5.5 **Left:** The InMR using GSD with θw $= 60^o$ ($x = 0.866$) for $M_\mathrm{s} = 1.6$ with d$y = 0.0002$ and d$y = 0.002$. **Right:** The GSD InMR-to-TRR transition point solution for for $M_\mathrm{s} = 1.6$ with $\theta_\mathrm{w}^\mathrm{tr} = 76.0^o$ with d$y = 0.0002$ and $\theta_\mathrm{w}^\mathrm{tr} = 71.3^o$ with d$y = 0.002$.

One possible reason for the inability of Geometric Shock Dynamics (GSD) to accurately predict the InMR-to-TRR transition point can be explained using Figure 5.6. In this figure, the Mach number at the foot of the Mach stem, M_st, is plotted for all wall angles, θw, up to $\theta_\mathrm{w}^\mathrm{tr}$.

M_st can be calculated for the analytical predictions. In the case for the three analytical solutions proposed by Ben-Dor [2] [16], a constant velocity was assumed. This velocity, in terms of a Mach number, can be found by simply adding V_{10} and C_{10} (adding equations A.8 and A.9). This gives $M_\mathrm{st} = V_{10} + C_{10} = 1.99$ when $M_\mathrm{s} = 1.6$. For the Classical CCW equation [18], at every θw, the value of M in equation 2.17 is found.

All the predictions (except for the Ben-Dor constant velocity prediction) correspond quite well with each other when $\theta\mathrm{w} < 45^o$. After this point, the CCW prediction continues to predict a linear increase in M_{st} while the CFD and GSD predictions begin to show an exponential increase in M_{st}.

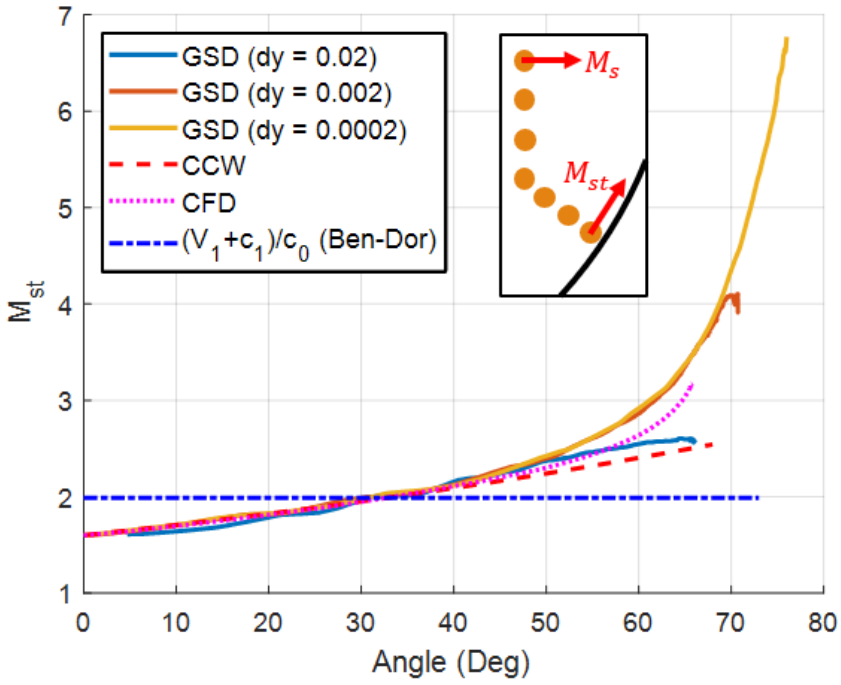

Fig. 5.6 The Mach number at the foot of the Mach stem, M_{st} for various GSD meshes, the CFD prediction, and the CCW and Ben-Dor analytical solutions for $M_s = 1.6$.

The magenta dotted line for CFD in Figure 5.6 shows an exponential increase up to the transition point with a max value of $M_{\text{st}} = 3.2$. However, the GSD solutions, with higher grid refinement, continue to show an increasing M_{st}. For GSD, the grid spacing of $\mathrm{d}y = 0.002$ and $\mathrm{d}y = 0.0002$, the value of M_{st} is the same up to the transition angle for $\mathrm{d}y = 0.002$. Beyond this angle, for GSD with $\mathrm{d}y = 0.0002$, M_{st} continues to increase exponentially up to $M_{\text{st}} = 6.8$. This indicates that for GSD, because of the $A - M$ Rule (Equation 5.13) as the grid size decrease, $\mathrm{d}y \to 0$, then the area also decreases, $A \to 0$, then M_{st} must increase to infinity, $M_{\text{st}} \to \infty$. Therefore, as seen with the results, continually decreasing $\mathrm{d}y$ does not result in a converged solution.

Because the CFD results, experiment results and analytical predictions each indicate a finite Mach number for the velocity of the Mach stem, then it can be concluded that

Geometric Shock Dynamics cannot be used to predict the InMR-to-TRR transition point.

5.6 GSD Overall Results

The results for the InMR-to-TRR transition point predictions using GSD for a range of Mach numbers from $M_s > 1$ to $M_s = 4$ are shown in Figure 5.7. The GSD predictions with $dy = 0.02$, $dy = 0.002$ and $dy = 0.0002$ are compared with some of the previous results.

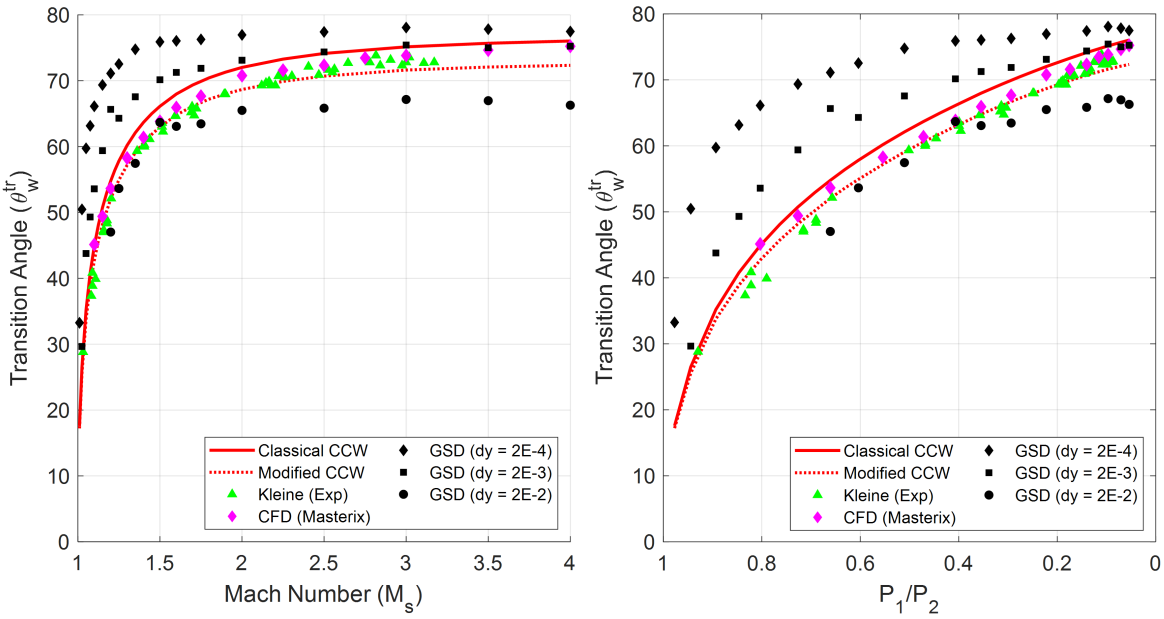

Fig. 5.7 The InMR-to-TRR transition point predictions using Geometric Shock Dynamics (GSD) with mesh sizes of $dy = 0.02$, $dy = 0.002$ and $dy = 0.0002$ compared with the CCW analytical predictions [18], the recent experiments by Kleine [22] and the CFD predictions using Masterix [25].

These predictions show that there is no reasonable grid-independent solution for finding the InMR-to-TRR transition point using Geometric Shock Dynamics. The results for GSD with $dy = 0.02$ seem to correspond with the experiment results [22] for $M_s \leq 1.5$, but for $M_s > 1.5$, $dy = 0.02$ under-predicts the transition point. Furthermore, the results using $dy = 0.002$ seem to compare similarly with the CFD results for $M_s > 3$ but over-predicts

the transition point for $M_s \leq 3$. The further refined mesh of $dy = 0.0002$ over-predicts for all Mach numbers shown.

5.7 Conclusion

This chapter focused on using Geometric Shock Dynamics to predict the InMR-to-TRR transition point over a concave cylindrical surface. A derivation of the governing equations ($A-M$ Rule) is shown in Section 5.2 while the detailed numerical scheme used is presented in Section 5.3. Results showing the shock propagation at various time steps are shown in Section 5.4 while a discussion on the lack of grid-independent solution using GSD is discussed in Section 5.5. Finally, the results using GSD with Mach numbers ranging from $M_s > 1$ to $M_s = 4$ are shown in Figure 5.7.

Based on the analysis of the results, GSD is not a reliable numerical method to predict the InMR-to-TRR transition point. Although GSD had previously been shown to be capable of providing an accurate prediction for the geometry of the shock front [33] [39] [40], GSD failed at converging to a grid-independent prediction for the transition point. This conclusion is backed up by Peton [44] who explicitly states that a triple point (called a shock-shock in his paper) will always appear in GSD, but with a small Mach stem height for cases in which a Regular Reflection is expected. Furthermore, Figure 5.6 shows $M_{st} \to \infty$ as the grid spacing decreases, indicating that the Mach stem will not disappear using GSD.

Chapter 6 provides direct comparisons of the various methods used to predict the transition point.

Chapter 6

Comparison of Results

Previous chapters focused on the methodology used to obtain the transition point. Chapter 2 focused on finding the transition point using, the MR-to-RR transition criteria [2], the three pathways proposed by Ben-Dor [16], the two analytical solutions described by Itoh [18]. Chapter 3 discussed older experiments by Ben-Dor and Takayama [19] and Takayama and Sasaki [20], weak-shock experiments by Gruber [23] and Cohen [14] and the recent experiments by Kleine [22]. Chapter 4 discussed CFD techniques, including Masterix [25] as a CFD flow solver, to find the transition point while Chapter 5 focused on using Geometric Shock Dynamics (GSD) to find the InMR-to-TRR transition point.

In Section 6.1, a direct comparison between the various methods used will be shown, going beyond just finding the transition point. This will include comparing the wave configurations of the experiments by Kleine [22], the CFD solution using Masterix [25] and the GSD solution at θw = 60^o. Furthermore, the triple point trajectory and Mach stem height for each method are plotted and discussed in Sections 6.1.3 and 6.1.4.

Section 6.2 provides the plots for the transition angles obtained from all the methods studied in this thesis.

6.1 Comparison for $M_s = 1.6$

6.1.1 Comparison at $\theta w = 60^o$

Figure 6.1 shows the results from the recent experiment [22], the CFD solver [25] and from GSD on the same scale and superimposed on each other at the moment when the triple point is at $\theta w = 60^o$.

These results are super-imposed onto each other to allow for a better comparison of the InMR configuration seen. The CFD and experiment results are nearly identical as they

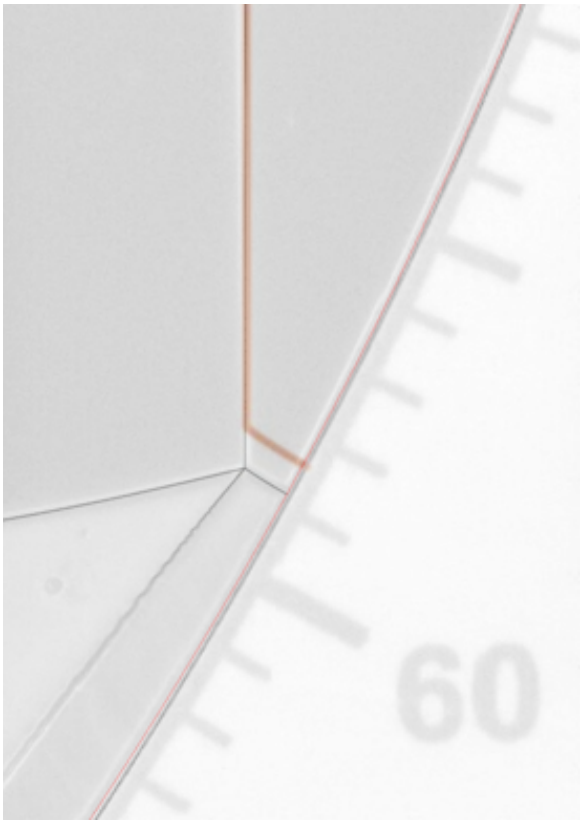

Fig. 6.1 Comparing the InMR experiment, CFD and GSD results with $M_s = 1.6$ at $\theta w = 60^o$ with super-imposed images. The experiment shows the InMR with Mach stem height $\tilde{h} = h/R = 0.0106$. CFD shows the InMR with Mach stem height $\tilde{h} = 0.0110$. GSD shows the InMR with Mach stem height $\tilde{h} = 0.0151$ using $dy = 0.0002$.

seamlessly super-impose one another. Each of the three shocks, incident, reflected, and Mach stem, as well as the slip stream, align almost perfectly. However, the GSD solution with $\mathrm{d}y = 0.0002$ clearly shows a longer Mach stem than the other methods.

The Mach stem height for the experiments with $M_\mathrm{s} = 1.6$ and $\theta\mathrm{w} = 60^o$ is $\tilde{h} = h/R = 0.0106$. The CFD solution had a similar Mach stem height of $\tilde{h} = 0.00110$ with the most refined mesh of Max Level 10 and Min Level 4. The Mach stem height using GSD with $\mathrm{d}y = 0.0002$ is $\tilde{h} = 0.0151$.

6.1.2 Comparison at $\theta_\mathrm{w}^\mathrm{tr}$

Figure 6.2 shows the visualization of the InMR-to-TRR transition point found from experiments (Left), using the CFD solver Masterix (Middle) and using Geometric Shock Dynamics (Right).

Both the experiment and CFD results show the incident shock, reflected shock and the slip stream with no Mach stem as expected. The transition angles with $M_\mathrm{s} = 1.6$ are found to be $\theta_\mathrm{w}^\mathrm{tr} = 65.0^o$ for the experiment and $\theta_\mathrm{w}^\mathrm{tr} = 65.9^o$ for CFD. The similarity between the experiment result by Kleine [22] and the inviscid CFD solver, at both $\theta\mathrm{w} = 60^o$ in Figure 6.1 and in the 0.9^o difference seen in Figure 6.2 for the transition angle, demonstrates the good comparison between these results. The small difference may be simply due to insufficient optical resolution and some viscous effects from the experiment.

The GSD solution, however, over-predicts the transition point with continuous mesh refinement as no grid-independent solution can be found.

6.1.3 Comparison of Triple Point Trajectory

Figure 6.3 shows the triple point trajectories of each of the methods used to find the transition point: The three pathways proposed by Ben-Dor [16], the Classical and Modified

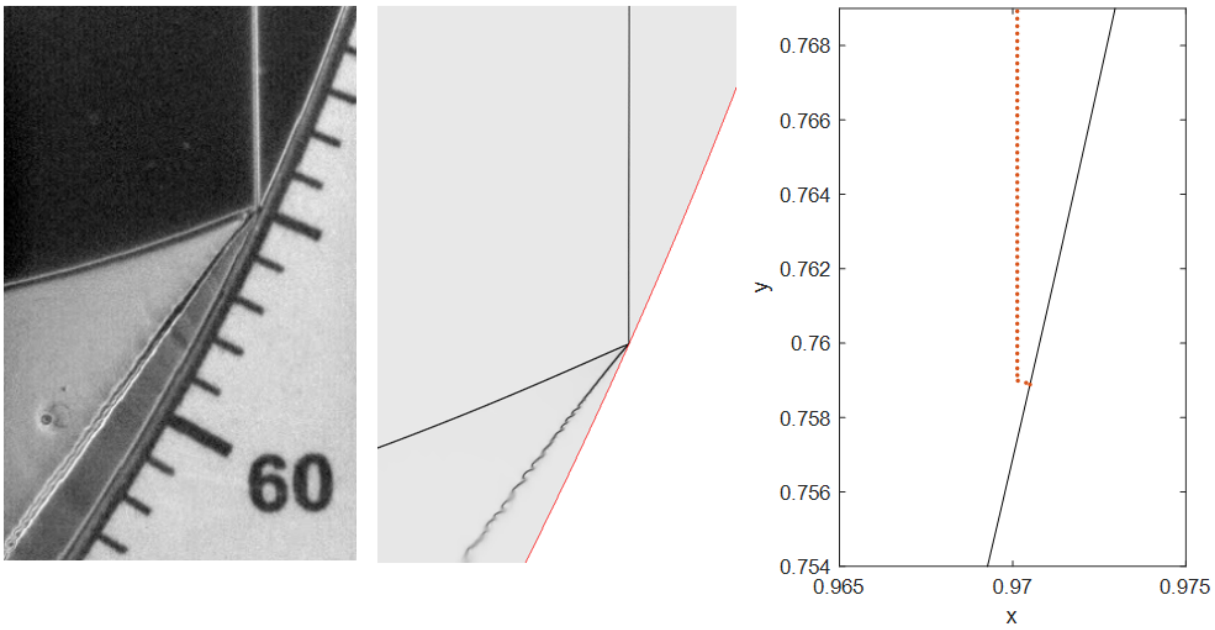

Fig. 6.2 Comparing the InMR experiment, CFD and GSD results with $M_s = 1.6$ at θ_w^{tr}. **Left:** Experiment Results showing transition point at $\theta_w^{tr} = 65.0^o$. **Mid:** CFD schlieren visualization of transition point at $\theta_w^{tr} = 65.9^o$. **Right:** GSD results showing transition point at $\theta_w^{tr} = 76.0^o$ using $dy = 0.0002$.

CCW [18], two grid sizes from GSD, the CFD solution and the experiments by Kleine [22].

From Figure 6.3, it can be easily seen that the pathways proposed by Ben-Dor for the corner-generated signals are not the actual triple point pathways. However, path (a) and path (b) provide boundaries for the likely triple point trajectory - since path (a) is already along the reflecting surface and based on experiment results, the triple point does not exceed the boundary of path (b). To analyze the other pathways, the magnified Figure 6.4 is used.

Each triple-point trajectory reaches the reflecting surface at a low angle (i.e. almost tangentially) as predicted. Because of this characteristic, early experiments were unable to visualize the small Mach stem near the transition point and thus under-predicted the transition point. This effect can be shown when comparing the triple point trajectory of the

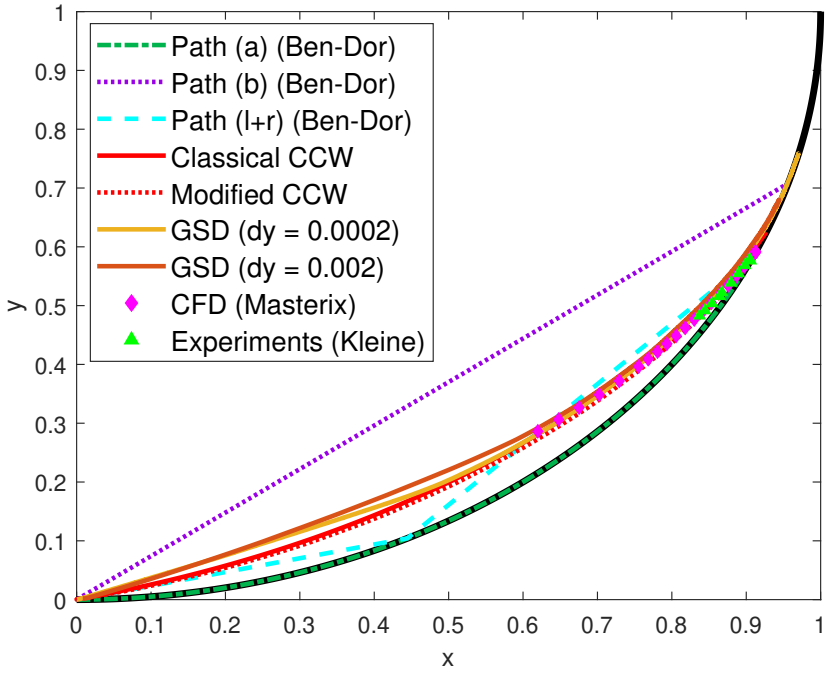

Fig. 6.3 The triple point trajectories of each method with $M_s = 1.6$ for the InMR on a concave cylindrical surface.

CFD solver with the recent experiments. Based on Figure 6.4, the CFD and experiments show a nearly identical triple point trajectory until the final experiment data point before transition. The transition point is then found to be $\theta_w^{tr} = 65.0^o$ for the experiments while the CFD solver continues to find even smaller Mach stems up until $\theta_w^{tr} = 65.9^o$ for $M_s = 1.6$.

6.1.4 Comparison of Mach Stem Height

Figure 6.5 shows the Mach stem height of the InMR prior to the transition point. Based on Figure 6.5, the inviscid CFD solver and from the recent experiment show similarly sized Mach stems. However, the GSD solutions shows how the Mach stem height asymptotes to the wall until $\tilde{h} \leq dy$. These GSD results do not agree with the experiment or CFD results.

Both the Classical and Modified CCW predictions do not predict the trend for Mach

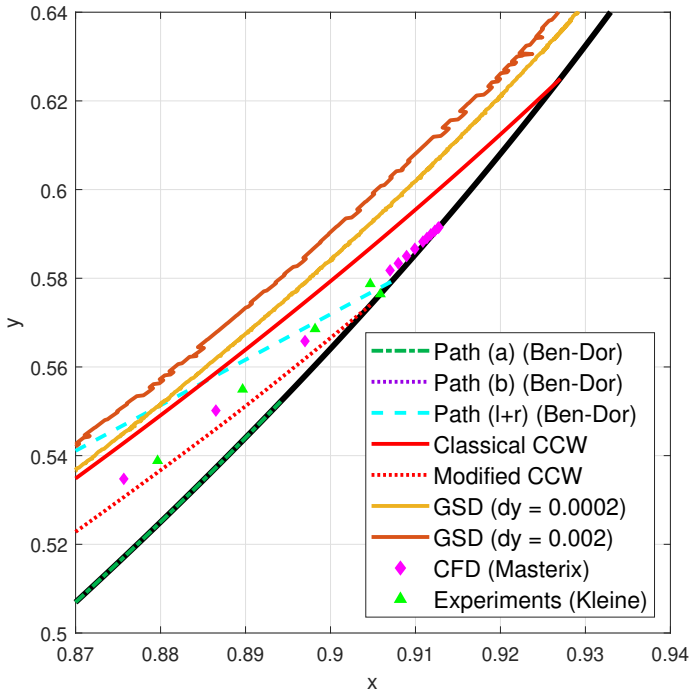

Fig. 6.4 Magnified view of the triple point trajectories of each method with $M_s = 1.6$ for the InMR on a concave cylindrical surface.

stem height for all wall angles. However, it is worth noting the transition point found for the Modified CCW, which accounts for the reflected shock and slip stream, is similar in value to the CFD and experiment transition points at $M_s = 1.6$.

CFD vs Experiment

The difference between the the CFD solution and experiment results is likely due to the shock thickness in the schlieren visualization (see Figure 6.2 (Left)). This shock thickness at $M_s = 1.6$ is about $\tau = 0.54$ mm or $\tilde{\tau} = 0.0038$ if non-dimensionalized with $R = 140$ mm. Since the measurement of the Mach stem height $\tilde{h}$ is taken from the mid-point of the incident shock, then shocks with $\tilde{h} < \tilde{\tau}/2$ cannot be measured.

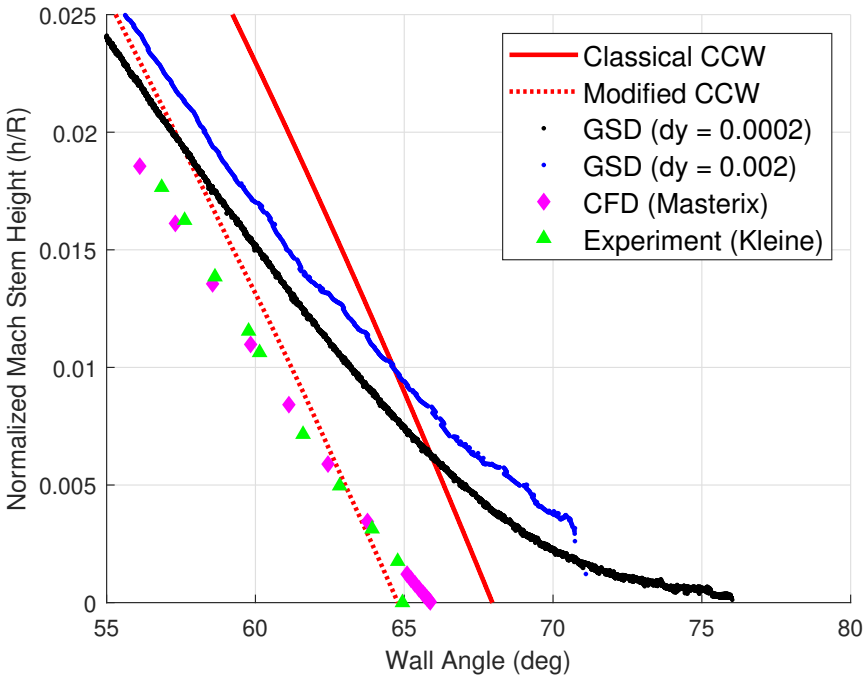

Fig. 6.5 The Mach stem height of the InMR using $M_s = 1.6$.

Figure 6.5 displays this measurement issue. The Mach stem height measured is nearly identical for the CFD and experiment values, except for the transition point. The smallest Mach stem height found from experiments was $\tilde{h} = 0.0018$, which is just smaller than half the incident shock thickness. However, using CFD, smaller Mach stems can be found. The smallest Mach stem height found using CFD at $M_\mathrm{s} = 1.6$ is $\tilde{h} = 3.24\text{x}10^{-5}$.

6.2 Overall Comparison

All the InMR-to-TRR transition points ($\theta_\mathrm{w}^\mathrm{tr}$) found from $M_\mathrm{s} > 1$ to $M_\mathrm{s} = 4$ are plotted in Figures 6.6 and 6.7 for each technique studied.

For stronger shocks ($M_\mathrm{s} > 1.1$), CFD appears to be a valid technique to find the InMR-to-TRR transition point as all three methods (WENO, ANSYS FLUENT and Masterix)

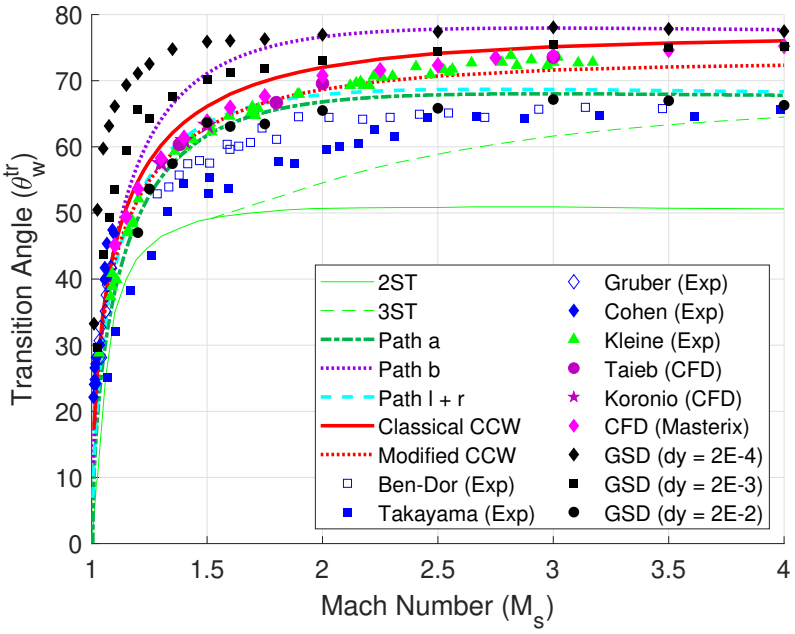

Fig. 6.6 InMR-to-TRR transition point predictions for all methods studied.

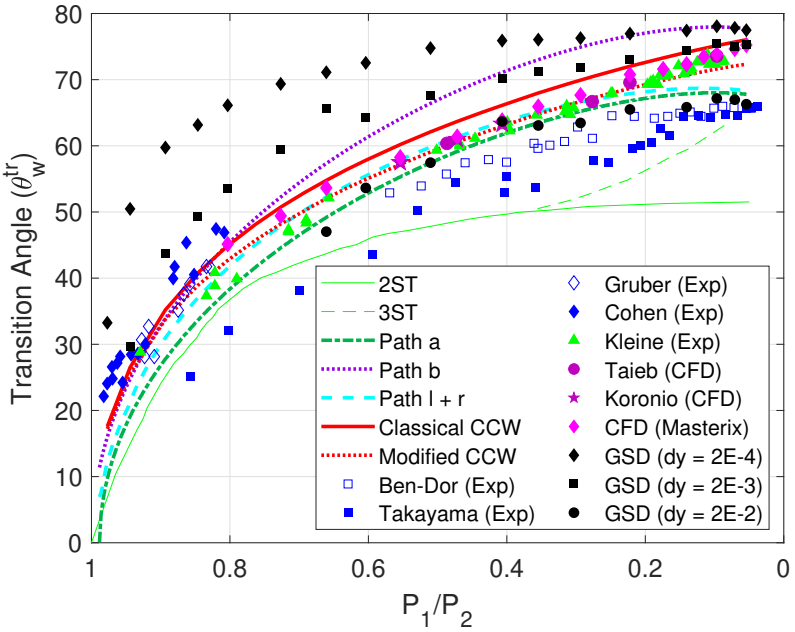

Fig. 6.7 InMR-to-TRR transition point predictions for all methods studied.

predict nearly identical transition points which are also in line with experimental results. For the current research, weak shocks with $M_s < 1.1$ were not studied using CFD. However, there appears to be good agreement between the weak shock experiments by Gruber [23] and Cohen [14] with the limited weak shock data from Kleine [22].

For analytical predictions, although it appears that the Modified CCW equation predicts an accurate transition point, this may simply be a coincidence because the evolution of the Mach stem height (Figure 6.5) does not show good agreement between the Mach stem heights of the Modified CCW equation and the CFD and experiment results.

Chapter 7

Concluding Remarks and Future Work

This thesis focused on studying unsteady shock wave reflections. Specifically, the main objective of this thesis is to find the transition point between an Inverse Mach Reflection (InMR) and a Transitioned Regular Reflection (TRR) over a concave cylindrical surface. A literature review on previous studies to find the InMR-to-TRR transition point revealed unsatisfactory agreement between analytical predictions and experimental results. Therefore, newer methods were studied in order to find a most accurate prediction of this transition point.

The in-house Computational Fluid Dynamics (CFD) flow solver, Masterix [25], was used to solve the set of 2-D Euler equations for inviscid and non-heat conducting flow over a concave cylindrical surface. Due to the dependence of the mesh size in CFD, a grid independent solution was found using Richardson extrapolation [35]. These results were found for a range of incident Mach numbers ($1.1 \leq M_s \leq 4$). These CFD results compared favorably to previous numerical studies by Taieb [24] and Koronio [15].

Although accurate InMR-to-TRR transition point predictions were found using CFD, due to computational constraints, finding a faster numerical method, while maintaining computational accuracy, is important for future work when analyzing 3-D shock wave reflections. Therefore, Geometric Shock Dynamics (GSD) was also studied to find the InMR-to-TRR transition point. GSD was chosen because it has previously been found to provide accurate estimations of shock reflections for various geometries [33]. Since the propagation of the shock reflection is found by directly relating the local geometry with the local Mach number, then the flow field behind the shock is not calculated. This decreases the computational time when compared to CFD techniques with similar grid sizes.

The GSD numerical scheme used was outlined by Ridoux [33]. Unlike the CFD flow solver Masterix, the GSD results did not provide a grid-independent solution for the InMR-to-TRR transition point. This was due to the direct relation between local area and Mach number: Continuing to refine the mesh by reducing dy, and therefore decreasing the smallest local area, resulted in a larger final M_{st} than found from the CFD prediction (see Figure 5.6). The conclusion that GSD cannot be used to accurately predict the InMR-to-TRR transition point is substantiated independently by Peton [44].

In order to judge the accuracy of the results obtained using numerical methods, the data from previous experiments needed to be found. First, results from two older experiments by Ben-Dor and Takayama [19] and Takayama and Sasaki [20] were found in literature. These experiments provided results with poor accuracy due to low optical resolution and therefore small Mach stems could not be resolved. The experiments by Kleine [22] addressed these issues by using a larger radius of curvature for the reflecting surface and using better measurement devices. These experiment results compared favorably with the results obtained using CFD.

Multiple analytical predictions were also considered in this thesis. The first predictions

are based on the four IR-to-RR transition criteria proposed by von Neumann and Hornung [2]: Detachment, mechanical equilibrium, sonic and length-scale criteria. These criteria resulted in three domains of solution: Regular Reflection, Mach Reflection and a dual-solution domain. These predictions significantly under-predict the actual InMR-to-TRR transition point found using CFD and recent experiments.

Then the analytical solutions proposed by Ben-Dor [16][28], which predicted three different pathways for the corner-generated perturbation signals, were studied. These predictions were based on the assumption that the transition point would occur once corner-generated signals could no longer catch-up with the reflection point and that the velocity of the corner generated signal is based on the flow behind the incident shock. However, CFD results have found that the corner-generated signal propagates with the speed of the Mach stem [21], which varies throughout the evolution of the shock reflection. For this reason, none of these analytical solutions provided accurate results over the entire range of Mach numbers.

Finally, the Classical and Modified CCW Equations described by Itoh [18] were studied. The Classical CCW Equation (2.17) is based on GSD. The Modified CCW Equation (2.18) added an extra term, η, to account for the flow behind the shock front. Both of these equations calculate the evolution of the Mach stem height. The transition points found using these equations appear to be reasonably accurate when compared to the recent experiments and CFD results. However, when looking at Figure 6.5, both the Classical and Modified CCW Equations provide very different Mach stem heights prior to transition.

Based on this study, it appears that numerical predictions using CFD provide the most accurate results for finding the InMR-to-TRR transition point for a wide range of Mach numbers ($1.1 \leq M_s \leq 4$) as these results are the most comparable with the recent experiment results. Despite the conclusions from this thesis, there are still some unanswered questions.

For example, weak shock results by Gruber [23] and Cohen [14] were also found in literature. Some future work would be needed to compare these results with numerical methods at low Mach numbers. Because two transition points (InMR-to-RR and RR-to-TRR) were observed in weak shock experiments, it is important to discover if numerical solutions found using a CFD solver could accurately find both of these transition points.

Further numerical studies could also be done for stronger shocks, such as detonation wave reflections. Yuan [45] has provided some preliminary work on this topic using a two-step induction-reaction kinetic model. Numerical observations showed a detonation reflection evolution similar to the shock reflection evolution described in Section 1.5 for strong shock waves: DiMR $\rightarrow$ InMR $\rightarrow$ TRR. At low wall angles, the triple point trajectory for detonation reflections was similar to that of shock reflections, but the paths diverged at higher wall angles. This results in smaller InMR-to-TRR transition angles for detonation reflections than for shock reflections. Furthermore, the transition point can be affected by the activation energy of the detonation, ϵ_r. Increasing ϵ_r increases the transition angle, $\theta_{\mathrm{w}}^{\mathrm{tr}}$.

More work could also be done in order to find an accurate analytical solution to find the InMR-to-TRR transition point. Timofeev and Previtali [21] proposed a semi-analytical solution. This analytical solution uses a similar problem setup as the Ben-Dor path (a) solution, except for using the velocity at the foot of the Mach stem instead of the constant flow velocity behind the incident shock. This method is semi-analytical because the Mach number at the foot of the Mach stem is found using the previously obtained results from CFD. Therefore, it is not yet a fully analytical prediction. Further details can be found in Appendix A.3.

Some future work would also be to study the shock wave propagation over more complex geometries. For example:

- Soni [46] and Brahmi [47] studied the shock reflection over double-concave cylindrical surfaces.
- Ram [48] and Reshma [49] studied the shock wave reflection over convex-concave cylindrical surfaces.
- Krassovskaya [50] and Koronio [15] studied the shock wave reflection over multi-faceted concave surfaces.
- Liang [51] and Gruber [23] studied the shock reflection over parabolic concave surfaces.

Appendix A

Extra Derivations

A.1 Deriving the Ben-Dor Governing Equation

This derivation is taken from [2]. The corner-generated perturbation signals travel with a speed of $V+c$, where V is the local velocity and c is the local speed of sound. The analytical solution states that the distance S, shown in Figure 2.7 as the triple point trajectory, in which the signals have propagated during the time interval from the leading edge to the transition point is given by:

$$S = \int_0^{\Delta t} (V + c)\mathrm{d}t \tag{A.1}$$

Where Δt is the time for the incident shock to travel from $x = 0$ to $x = x^{\mathrm{tr}}$. In general, both V and c will vary throughout the domain. However, because reflected shock waves near the reflecting surface are generally weak, the flow properties do not vary much, and therefore they can be assumed constant.

$$V + c = V_1 + c_1 \tag{A.2}$$

Thus the distance travelled becomes

$$S = (V_1 + c_1)\Delta t \tag{A.3}$$

Substituting in $\Delta t = \frac{x^{\mathrm{tr}}}{V_s}$, where V_s is the speed of the incident shock:

$$S = (V_1 + c_1)\frac{x^{\mathrm{tr}}}{V_s} \tag{A.4}$$

Now dividing both sides of the equation by the speed of sound of the undisturbed gas, c_0:

$$\frac{S}{c_0} = \frac{V_1 + c_1}{c_0}\frac{x^{\mathrm{tr}}}{V_s} \tag{A.5}$$

$$S\left(\frac{V_s}{c_0}\right) = (V_{10} + C_{10})x^{\mathrm{tr}} \tag{A.6}$$

$$x^{\mathrm{tr}} = S\left(\frac{M_{\mathrm{s}}}{V_{10} + C_{10}}\right) \tag{A.7}$$

Where V_{10} and C_{10} are functions of M_s given by Ben-Dor [2] as:

$$V_{10} = \frac{2(M_{\mathrm{s}}^2 - 1)}{(\gamma + 1)M_{\mathrm{s}}} \tag{A.8}$$

$$C_{10} = \frac{\gamma - 1}{\gamma + 1}\frac{1}{M_{\mathrm{s}}}\sqrt{\left(\frac{2\gamma}{\gamma - 1}M_{\mathrm{s}}^2 - 1\right)\left(M_{\mathrm{s}}^2 + \frac{2}{\gamma - 1}\right)} \tag{A.9}$$

The distance travelled by the incident shock can also be found geometrically from Figure 2.7:

$$x^{\mathrm{tr}} = R\sin\theta_{\mathrm{w}}^{\mathrm{tr}} \tag{A.10}$$

Equating both equations A.7 and A.10 yields:

$$R \sin \theta_{\mathrm{w}}^{\mathrm{tr}} = S \frac{M_{\mathrm{s}}}{V_{10} + C_{10}} \tag{A.11}$$

A.2 Detailed GSD Numerical Scheme

The TVD third-order Runge-Katta scheme to solve the $A - M$ rule is given by equations 5.23, 5.24 and 5.25. Further details for solving this scheme are provided below. This numerical scheme is based on the work by Ridoux [33].

A.2.1 Selecting $\Delta\alpha$

The time step, $\Delta\alpha$, needs to be selected. This value is restricted by the stability condition of this algorithm and by the limit on the number of points interacting with the boundary.

The first restriction on $\Delta\alpha$ is that the scheme must be stable under the Courant-Friedrichs-Lewy (CFL) condition:

$$\Delta\alpha \leq \Delta\alpha_s = d_{\min} \Delta s \ \ \min_{i=1,\ldots,N} \left(\sqrt{\frac{\lambda(M_i)}{M_i^2 - 1}}, \frac{2M_i}{k(M_i^2 - 1)} \right) \tag{A.12}$$

Where $d_{\min}$ is a parameter introduced later. This inequality must exist due to the perturbation velocities along the shock front:

$$\frac{\mathrm{d}s}{\mathrm{d}\alpha} = \pm A u(M) = \sqrt{\frac{M^2 - 1}{\lambda(M)}} \tag{A.13}$$

The second restriction on $\Delta\alpha$ is that the rays do not cross. Numerically, this means:

$$\Delta\alpha \leq \Delta\alpha_c = \min_{i \varepsilon I} \left(\frac{l_{i-1}}{M_{i-1}}, \frac{k_i}{M_i} \right) \tag{A.14}$$

$$l_{i-1} = \frac{\overrightarrow{X_{i-1}X_i} \cdot n_{i-1} - (\overrightarrow{X_{i-1}X_i} \cdot n_i)(n_{i-1} \cdot n_i)}{1 - (n_{i-1} \cdot n_i)^2} \tag{A.15}$$

$$k_i = -\frac{\overrightarrow{X_{i-1}X_i} \cdot n_i - (\overrightarrow{X_{i-1}X_i} \cdot n_{i-1})(n_{i-1} \cdot n_i)}{1 - (n_{i-1} \cdot n_i)^2} \tag{A.16}$$

$$I = i = 2, ..., \frac{N}{l_{i-1}} > 0, \quad k_i > 0 \text{ and } |n_{i-1} \cdot n_i| \neq 1 \tag{A.17}$$

Then based on the two conditions, equations A.12 and A.14, the time step, $\Delta\alpha$ is chosen:

$$\Delta\alpha = \delta \min(\Delta\alpha_s, \Delta\alpha_c) \tag{A.18}$$

Where δ is a safety coefficient between 0 and 1.

A.2.2 Finding n_i, A_i and M_i

Interpolation of Shock Surface

An interpolation of the shock surface is performed over all the data $(s_i, x_i)_{i=1,...,N}$, $(s_i, y_i)_{i=1,...,N}$ using a monotone cubic method [43]. This is done in order to avoid creating new extreme values. The unit normal vector is first calculated:

$$n_i = \frac{(Y'(s_i) - X'(s_i))^T}{\sqrt{X'(s_i)^2 + Y'(s_i)^2}} \text{ for } i = 1, ..., N \tag{A.19}$$

Where the interpolates are denoted $s \to X(s)$ and $s \to Y(s)$.

Finding the Local Area

The local area is found using a central scheme (the endpoints have a one-sided scheme). To note, $\nu = 0$ for 2D planar and $\nu = 1$ for 2D asymmetric flow.

$$A_i = \frac{\pi^\nu}{2} \begin{cases} \Delta s_2 (x_2 + x_1)^\nu & \text{if } \; i = 1 \\ \Delta s_{i+1}(x_{i+1} + x_i)^\nu + \Delta s_i (x_i + x_{i-1})^\nu & \text{if } \; i = 2, ..., N-1 \\ \Delta s_N (x_N + x_{N-1})^\nu & \text{if } \; i = N \end{cases} \tag{A.20}$$

Finding Mach Number

To find the Mach number at time $\alpha + \Delta\alpha$, the $A-M$ relation must be integrated numerically along each ray tube:

$$\log\left(\frac{A_i(\alpha + \Delta\alpha)}{A_i(\alpha)}\right) + \int_{M_i(\alpha)}^{M_i(\alpha+\Delta\alpha)} \frac{m\lambda(m)}{m^2 - 1} \mathrm{d}m + \int_\alpha^{\alpha+\Delta\alpha} H(\kappa) f(M) \left|\frac{\partial M}{\partial s}\right| \mathrm{d}\tau = 0 \tag{A.21}$$

Actually solving this integration is discussed in section A.2.4.

A.2.3 Inserting or Deleting Points

After the shock front for the next time step is calculated, new data points either need to be inserted in expansive regions to maintain sufficient resolution or deleted in compressive regions to avoid excessive data points. The point spacing should be:

$$d_{\min} \Delta s \leq \Delta s_i \leq d_{\max} \Delta s \tag{A.22}$$

Where $d_{\min} < 1$ and $d_{\max} > 1$ with commonly chosen values of 0.5 and 1.5 respectively. Therefore, if $\Delta s_i < d_{\min} \Delta s$, then the point x_i is removed from the shock front. Similarly,

if $\Delta s_i > d_{\max}\Delta s$, then a new point, $x_{i-\frac{1}{2}}$ is added using a cubic spline interpolation. This interpolation is evaluated as $\frac{1}{2}(s_{i-1}+s_i)$. To note, in these cases, the same points are added or removed from the initial shock front in order to conserve the scheme for the area ratio of $\frac{A_i(\alpha+\Delta\alpha)}{A_i(\alpha_0)}$. A smoothing procedure is applied to help dampen the errors in the shock front. After a set number of iterations n_s, which range from 10 up to 50, for $i = 2, ..., N-1$:

$$x_i = \frac{h_r}{h_l + h_r}x_{i-1} + \frac{h_l}{h_l + h_r}x_{i+1} \tag{A.23}$$

This is with $h_l = ||x_i - x_{i-1}||$ and $h_r = ||x_{i+1} - x_i||$. With a wall, boundary conditions must be applied to keep the shock locally normal to the wall. This is done by:

$$X^{'}(s_{\text{bound}}) = N_x \text{ and } Y^{'}(s_{\text{bound}}) = N_y \tag{A.24}$$

Where s_{bound} defines the shock boundary and $N = \begin{bmatrix} N_x \\ N_y \end{bmatrix}$ is the unit normal vector to the wall. The normal vector at the wall is defined by:

$$n(s_{\text{bound}}) = \begin{bmatrix} N_y \\ -N_x \end{bmatrix} \tag{A.25}$$

This ensures that the bounding point moves along the wall.

A.2.4 Integrating the $A - M$ Equation

Due to the insertion or deletion of some data points along the shock front, there may be a loss in conservativity of the numerical scheme. Without any regularization, the integration

of the $A - M$ relation could simply be done from the initial time α_0 to $\alpha + \Delta\alpha$.

$$\log\left(\frac{A_i(\alpha+\Delta\alpha)}{A_i(\alpha_0)}\right) + \int_{M_i(\alpha_0)}^{M_i(\alpha+\Delta\alpha)} \frac{m\lambda(m)}{m^2-1}\mathrm{d}m = 0 \tag{A.26}$$

With regularization, the integration needs to be split in two. Since the information at time α would already be known based on integration performed before regularization, then the second portion of the integral would be from α to $\alpha + \Delta\alpha$. For the case of simple GSD without the ad hoc modification ($H(\kappa) = 0$), this integral can be calculated:

$$\log\left(\frac{A_i(\alpha+\Delta\alpha)}{A_i(\alpha)}\right) + \int_{M_i(\alpha)}^{M_i(\alpha+\Delta\alpha)} \frac{m\lambda(m)}{m^2-1}\mathrm{d}m = 0 \tag{A.27}$$

With regularisation, this integration would not work. Instead, the following needs to be done. Assume the shock front is first regularized at $\alpha + \Delta\alpha$, resulting in the removal of point x_j, then the ray tubes indexed by $j-1$ and $j+1$ are then modified (as seen in Figure A.1) which modifies the corresponding A_{j-1} and A_{j+1}. Due to the change in the number of points, some modifications must be made.

For the following description, assume any quantities before regularization are denoted as $\tilde{\psi}$ and ψ after regularization. For instance, the deletion of a point would not modify Mach number ($M(\alpha_0) = \tilde{M}(\alpha_0)$), but the ray tube areas have changed: $A_{j\pm1}(\alpha_0) \neq \tilde{A}_{j\pm1}(\alpha_0)$. For example, at node x_{j+1}, the Mach number at $\alpha + \Delta\alpha$ can be evaluated with:

$$\log\left(\frac{A_{j+1}(\alpha+\Delta\alpha)}{A_{j+1}(\alpha)}\right) + \int_{\tilde{M}_{j+1}(\alpha)}^{M_{j+1}(\alpha+\Delta\alpha)} \frac{m\lambda(m)}{m^2-1}\mathrm{d}m = 0 \tag{A.28}$$

Using equation A.27, and knowing shock front at time α, its value must be the same with

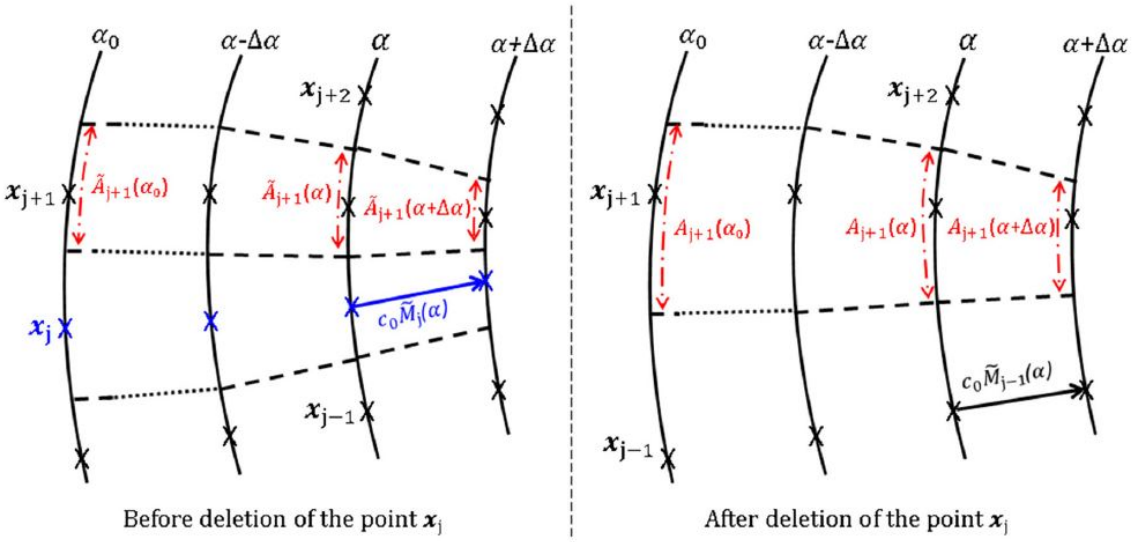

Fig. A.1 Schematic of redefining the ray tubes after a deleted point in GSD [33].

an integration from the initial time (equation A.26).

$$\log\left(\frac{A_{j+1}(\alpha+\Delta\alpha)}{A_{j+1}(\alpha_0)}\right)+\int_{M_{j+1}(\alpha_0)}^{M_{j+1}(\alpha+\Delta\alpha)}\frac{m\lambda(m)}{m^2-1}\mathrm{d}m=0 \tag{A.29}$$

The Mach number at time α is known before regularization:

$$\log\left(\frac{\tilde{A}_{j+1}(\alpha)}{\tilde{A}_{j+1}(\alpha_0)}\right)+\int_{M_{j+1}(\alpha_0)}^{\tilde{M}_{j+1}(\alpha+\Delta\alpha)}\frac{m\lambda(m)}{m^2-1}\mathrm{d}m=0 \tag{A.30}$$

Applying equation A.30 and A.28 and get:

$$\log\left(\frac{A_{j+1}(\alpha+\Delta\alpha)}{A_{j+1}(\alpha_0)}\right)+\int_{M_{j+1}(\alpha_0)}^{M_{j+1}(\alpha+\Delta\alpha)}\frac{m\lambda(m)}{m^2-1}\mathrm{d}m+\log\left(\frac{\tilde{A}_{j+1}(\alpha)}{A_{j+1}(\alpha)}\frac{A_{j+1}(\alpha_0)}{\tilde{A}_{j+1}(\alpha_0)}\right)=0 \tag{A.31}$$

This equation A.31 differs from equation A.29 due to modification of local areas. This implies a loss in conservativity of the scheme and therefore a modification is needed. Equation A.32 is the general form of the $A-M$ relation.

$$\frac{1}{A}\frac{\partial A}{\partial \alpha} + \frac{M\lambda(M)}{M^2-1}\frac{\partial M}{\partial \alpha} + R(\alpha,\beta) = 0 \tag{A.32}$$

$$R(\alpha,\beta) = H(\kappa)f(M)\left|\frac{\partial M}{\partial s}\right| \tag{A.33}$$

Deleting Points

For deleting points, Ridoux [33] proposes the following modification: If $\tilde{A}_i$ and $\tilde{M}_i$ are the area and Mach number for point X_i before regularization, then A_i and M_i are the area and Mach number after regularization.

$$\log\left(\frac{A_i(\alpha+\Delta\alpha)}{\tilde{A}_i(\alpha)}\frac{\tilde{A}_i(\alpha_0)}{A_i(\alpha_0)}\right) + \int_{\tilde{M}_i(\alpha)}^{M_i(\alpha+\Delta\alpha)}\frac{m\lambda(m)}{m^2-1}\mathrm{d}m + \int_{\alpha}^{\alpha+\Delta\alpha} R(\tau,\beta_i)\mathrm{d}\tau = 0 \tag{A.34}$$

Inserting Points

For inserting points, Ridoux [33] proposes the following modification: If A_i and M_i are the area and Mach number after regularization, and $X_{i+1/2}$ is inserted on the shock front at time $\alpha+\Delta\alpha$, then $M_{i+1/2}(\alpha+\Delta\alpha)$ can be estimated:

$$I + \int_{M_i(\alpha+\Delta\alpha)}^{M_{i+1/2}(\alpha+\Delta\alpha)}\frac{m\lambda(m)}{m^2-1}\mathrm{d}m + \int_{M_{i+1}(\alpha+\Delta\alpha)}^{M_{i+1/2}(\alpha+\Delta\alpha)}\frac{m\lambda(m)}{m^2-1}\mathrm{d}m = 0 \tag{A.35}$$

$$\begin{aligned} I = 2\log\left(\frac{A_{i+1/2}(\alpha+\Delta\alpha)}{A_{i+1/2}(\alpha_0)}\sqrt{\frac{A_i(\alpha_0)}{A_i(\alpha+\Delta\alpha)}\frac{A_{i+1}(\alpha_0)}{A_{i+1}(\alpha+\Delta\alpha)}}\right) \\ + \int_{M_{i+1/2}(\alpha_0)}^{M_i(\alpha_0)}\frac{m\lambda(m)}{m^2-1}\mathrm{d}m + \int_{M_{i+1/2}(\alpha_0)}^{M_{i+1}(\alpha_0)}\frac{m\lambda(m)}{m^2-1}\mathrm{d}m \end{aligned} \tag{A.36}$$

Calculating Mach Number

The Mach number at time $\alpha + \Delta\alpha$ is estimated by first applying equation A.34 to all points but the newly added points. Then applying equation A.35 for the inserted points.

Integrating the Transverse Term

The transverse term is:

$$f(M)\left|\frac{\partial M}{A\partial\beta}\right| = \text{sign}(f(M))\left|\frac{\partial F(M)}{\partial s}\right| \tag{A.37}$$

With $F(M) = \int f(m)\mathrm{d}m$ and $\text{sign}(f(M))$ defined as:

$$\text{sign}(f(M)) = \begin{cases} 1 & \text{if } f(M) > 0 \\ -1 & \text{if } f(M) \leq 0 \end{cases} \tag{A.38}$$

The equation can be solved with a monotone upwind scheme:

$$f(M)\left|\frac{\partial M}{\partial s}\right|_{M=M_i} \approx \text{sign}(f(M_i))\max(\Delta_l F_i, -\Delta_r F_i, 0) \tag{A.39}$$

Where the terms $\Delta_l F_i$ and $\Delta_r F_i$ are the estimated slopes of $F(M)$ on both sides of M_i:

$$\Delta_l F_i = \frac{F(M_i) - F(M_{i-1})}{s_i - s_{i-1}} \qquad \Delta_r F_i = \frac{F(M_{i+1}) - F(M_i)}{s_{i+1} - s_i} \tag{A.40}$$

When a wall boundary exists, the local shock front must be perpendicular to the wall surface. Consequently, the transverse variation of the Mach number at a shock boundary

is equal to zero:

$$\left.\frac{\partial F(M)}{\partial s}\right|_{s=s_{\text{bound}}} = 0 \tag{A.41}$$

On each ray tube, the integration of the $A - M$ relation from time $\alpha + \Delta\alpha$ is written as:

$$\begin{aligned} &\log\left(\frac{A_i(\alpha+\Delta\alpha)}{A_i(\alpha)}\right) + \int_{M_i(\alpha)}^{M_i(\alpha+\Delta\alpha)} \frac{m\lambda(m)}{m^2-1}\mathrm{d}m \\ &+ \int_{\alpha}^{\alpha+\Delta\alpha} H(\kappa_i)\text{sign}(f(M_i))\max(\Delta_l F_i, -\Delta_r F_i, 0)\delta\tau = 0 \end{aligned} \tag{A.42}$$

The first integral is calculated with Simpson's rule, while the second integral is solved with trapezoidal rule. Then, a Newton algorithm can solve the nonlinear system.

A.2.5 Finding the Local Shock Curvature

In order to solve equation A.42, the sign of the local shock curvature, κ_i at x_i, is needed:

$$\kappa_i = \frac{4\sin(\phi_i/2)}{||\overrightarrow{X_{i-1}X_i}|| + ||\overrightarrow{X_iX_{i+1}}||} \tag{A.43}$$

Where ϕ_i is the angle between $\overrightarrow{X_{i-1}X_i}$ and $\overrightarrow{X_iX_{i+1}}$. The local curvature, $\kappa_i = 0$ if the points X_{i-1}, X_i and X_{i+1} are aligned, $\kappa_i > 0$ if the points are convex (expansive shock) and $\kappa_i < 0$ if the points are concave (compressive shock).

Because the local curvature can show many small oscillations on the shock front, there is the need for a temporary coarse distribution on the shock front to evaluate the curvature - A line simplification algorithm [52]. The intermediate points are interpolated with a monotone quadratic spline [53]. The local curvature is then defined at X_i using equation A.43 at temporary points.

Near a shock-shock (or triple point) where a discontinuity occurs, the transverse term needs to eliminated in order to ensure convergence. The transverse term at node X_l, at

a distance of d_c from the point where the Mach number variation is the highest, X_c, is deactivated: $H(\kappa_l) = 0$. d_c can be commonly taken as 0.05 [33].

A.3 Semi-Analytical Prediction

This prediction was first proposed by Timofeev and Previtali [21]. Consider that the corner generated signal travels at the speed of the Mach stem along the wall (i.e. the foot of the Mach stem). Since transition occurs at t^{tr} when $x = x^{\mathrm{tr}}$, and the incident shock moves at a constant velocity of V_{s}, then $t^{\mathrm{tr}} = x^{\mathrm{tr}}/V_{\mathrm{s}}$. The foot of the Mach stem moves with a variable velocity of V_{st}. Time t^{tr} can also be found by integrating along the reflecting surface:

$$\frac{x^{\mathrm{tr}}}{V_{\mathrm{s}}} = \int_0^{s^{\mathrm{tr}}} \frac{\mathrm{d}s}{V_{\mathrm{st}}} \tag{A.44}$$

Where s^{tr} is the path along reflecting surface from the origin to the transition point. Knowing that $x^{\mathrm{tr}} = R\sin\theta_{\mathrm{w}}^{\mathrm{tr}}$ and $\mathrm{d}s = R\mathrm{d}\theta_{\mathrm{w}}$, and converting V_{s} and V_{st} to M_{s} and M_{st} respectively by dividing by the speed of sound, and after diving both sides by R, Equation A.44 becomes:

$$\frac{\sin\theta_{\mathrm{w}}^{\mathrm{tr}}}{M_{\mathrm{s}}} = \int_0^{\theta_{\mathrm{w}}^{\mathrm{tr}}} \frac{\mathrm{d}\theta\mathrm{w}}{M_{\mathrm{st}}(\theta\mathrm{w})} \tag{A.45}$$

Dividing both sides by $\theta_{\mathrm{w}}^{\mathrm{tr}}$ yields the following:

$$\frac{\sin\theta_{\mathrm{w}}^{\mathrm{tr}}}{\theta_{\mathrm{w}}^{\mathrm{tr}}} = M_{\mathrm{s}}\left[\frac{1}{\theta_{\mathrm{w}}^{\mathrm{tr}}}\int_0^{\theta_{\mathrm{w}}^{\mathrm{tr}}} \frac{\mathrm{d}\theta\mathrm{w}}{M_{\mathrm{st}}(\theta\mathrm{w})}\right] \tag{A.46}$$

Solving Equation A.47 using M_{st} values taken from CFD results yields analytical predictions of the transition point similar to that of the results found using CFD. However, because M_{st} needs to be found using CFD, this is not a fully analytical solution.

Recovering Ben-Dor Path (a) Prediction

If the square bracket in Equation A.46 were taken as an average, then:

$$\frac{\sin\theta_{\mathrm{w}}^{\mathrm{tr}}}{\theta_{\mathrm{w}}^{\mathrm{tr}}} = M_{\mathrm{s}} \left\langle \frac{1}{M_{\mathrm{st}}} \right\rangle \tag{A.47}$$

Assume $M_{\mathrm{st}} = V_{10} + C_{10}$, then Equation A.47 would become:

$$\frac{\sin\theta_{\mathrm{w}}^{\mathrm{tr}}}{\theta_{\mathrm{w}}^{\mathrm{tr}}} = \frac{M_{\mathrm{s}}}{V_{10} + C_{10}} \tag{A.48}$$

Where Equation A.48 is identical to the Ben-Dor Path (a) solution (Equation 2.5).

References

[1] P. H. Oosthuizen and W. E. Carscallen, *Introduction to Compressible Fluid Flow*. CRC Press, Taylor Francis Group, 2nd ed., 2014.

[2] G. Ben-Dor, *Shock Wave Reflection Phenomena*, vol. 2. Springer, 2007.

[3] P. Krehl and M. van der Geest, *The Discovery of the Mach Reflection Effect and Its Demonstration in an Auditorium*, pp. 443–469. Cham: Springer International Publishing, 2019.

[4] H. Reichenbach, "Contributions of Ernst Mach to Fluid Mechanics," *Annual Review of Fluid Mechanics*, vol. 15, no. 1, pp. 1–29, 1983.

[5] G. Ben-Dor, "A State-of-the-Knowledge Review on Pseudo-Steady Shock-Wave Reflections and their Transition Criteria," *Shock Waves*, vol. 15, pp. 277–294, 07 2006.

[6] P. Colella and L. F. Henderson, "The von Neumann Paradox for the Diffraction of Weak Shock Waves," *Journal of Fluid Mechanics*, vol. 213, p. 71–94, 1990.

[7] P. B. Bulat, "The History of the Study of Shock Wave's Mach Reflection from the Wedge," *International Electronic Journal of Mathematics Education*, vol. 11, p. 1151–1162, Jul 2016.

[8] E. I. Vasilev, T. Elperin, and G. Ben-Dor, "Analytical Reconsideration of the von Neumann Paradox in the Reflection of a Shock Wave over a Wedge," *Physics of Fluids*, vol. 20, p. 046101, Apr 2008.

[9] A. Defina, F. M. Susin, and D. P. Viero, "Numerical study of the Guderley and Vasilev reflections in steady two-dimensional shallow water flow," *Physics of Fluids*, vol. 20, p. 097102, Sep 2008.

[10] G. Birkhoff, *Hydrodynamics*. Princeton University Pres, 2016.

[11] K. G. Guderley, *The Theory of Transonic Flow*. Pergamon Press, 1962.

[12] G. Ben-Dor and K. Takayama, "The Dynamics of the Transition from Mach to Regular Reflection over Concave Cylinders," *Israel Journal of Technology*, vol. 23, 01 1987.

[13] M. Karzova, V. Khokhlova, E. Salze, S. Ollivier, and P. Blanc-Benon, "Mach Stem Formation in Reflection and Focusing of Weak Shock Acoustic Pulses," *The Journal of the Acoustical Society of America*, vol. 137, pp. EL436–EL442, 06 2015.

[14] A. Cohen and B. Skews, "Very Weak Shock Wave Reflection off Curved Surfaces," *Experiments in Fluids*, vol. 61, no. 8, 2020.

[15] E. Koronio, G. Ben-Dor, O. Sadot, and M. Geva, "Similarity in Mach Stem Evolution and Termination in Unsteady Shock-Wave Reflection," *Journal of Fluid Mechanics*, vol. 902, p. A1, 2020.

[16] G. Ben-Dor and K. Takayama, "Analytical Prediction of the Transition from Mach to Regular Reflection over Cylindrical Concave Wedges," *Journal of Fluid Mechanics*, vol. 158, p. 365–380, 1985.

[17] K. Takayama and G. Ben-Dor, "A Reconsideration of the Transition Criterion from Mach to Regular Reflection over Cylindrical Concave Surfaces," *KSME Journal*, vol. 3, pp. 6–9, 1989.

[18] S. Itoh, N. Okazaki, and M. Itaya, "On the Transition between Regular and Mach Reflection in Truly non-stationary Flows," *Journal of Fluid Mechanics*, vol. 108, p. 383–400, 1981.

[19] G. Ben-Dor and K. Takayama, "Streak Camera Photography with Curved Slits for the Precise Determination of Shock Wave Transition Phenomena," *Canadian Aeronautics and Space Journal*, vol. 27, pp. 128–134, June 1981.

[20] K. Takayama and M. Sasaki, "Effects of Radius of Curvature and Initial Angle on the Shock Transition over Concave or Convex Walls.," *Reports of the Institute High Speed Mechanics, Tohoku University*, vol. 46, pp. 1 – 30, 1983.

[21] E. Timofeev, F. Alzamora Previtali, and H. Kleine, "On Unsteady Shock Wave Reflection from a Concave Cylindrical Surface," in *Shock Wave Interactions* (K. Kontis, ed.), (Cham), pp. 367–383, Springer International Publishing, 2018.

[22] F. A. Previtali, E. Timofeev, and H. Kleine, "On InMR-TRR Transition on a Concave Cylindrical Reflector," in *31st International Symposium on Shock Waves 1* (A. Sasoh, T. Aoki, and M. Katayama, eds.), (Cham), pp. 751–758, Springer International Publishing, 2019.

[23] S. Gruber and B. Skews, "Weak Shock Wave Reflection from Concave Surfaces," *Experiments in Fluids*, vol. 54, no. 7, 2013.

[24] D. Taieb, G. Ribert, and A. Hadjadj, "Numerical Simulations of Shock Focusing over Concave Surfaces," *AIAA Journal*, vol. 48, no. 8, p. 1739–1747, 2010.

[25] R.B.T Consultants, *Masterix, ver 3.41*, 2003-2021.

[26] J. von Neumann, "Oblique Reflection of Shocks," *Navy Dept., Bureau of Ordnance Explosives Res. Rept.*, no. 12, 1943.

[27] H. G. Hornung, H. Oertel, and R. J. Sandeman, "Transition to Mach Reflexion of Shock Waves in Steady and Pseudosteady Flow with and without Relaxation," *Journal of Fluid Mechanics*, vol. 90, no. 3, p. 541–560, 1979.

[28] G. Ben-Dor, K. Takayama, and J. Dewey, "Further Analytical Considerations of Weak Planar Shock Wave Reflections over a Concave Wedge," *Fluid Dynamics Research*, vol. 2, no. 2, pp. 77–85, 1987.

[29] R. Kawamura and H. Saito, "Reflection of Shock Waves–1 Pseudo-Stationary Case," *Journal of the Physical Society of Japan*, vol. 11, no. 5, pp. 584–592, 1956.

[30] W. Chester, "The Propagation of Shock Waves in a Channel of Non-Uniform Width," *The Quarterly Journal of Mechanics and Applied Mathematics*, vol. 6, pp. 440–452, 03 1953.

[31] R. F. Chisnell, "The Motion of a Shock Wave in a Channel, with Applications to Cylindrical and Spherical Shock Waves," *Journal of Fluid Mechanics*, vol. 2, no. 3, p. 286–298, 1957.

[32] G. B. Whitham, "A New Approach to Problems of Shock Dynamics Part I Two-dimensional Problems," *Journal of Fluid Mechanics*, vol. 2, no. 2, p. 145–171, 1957.

[33] J. Ridoux, N. Lardjane, L. Monasse, and F. Coulouvrat, "Beyond the Limitation of Geometrical Shock Dynamics for Diffraction over Wedges," *Shock Waves*, 01 2019.

[34] T. Saito, P. Voinovich, E. Timofeev, and K. Takayama, *Development and Application of High-Resolution Adaptive Numerical Techniques in Shock Wave Research Center*, pp. 763–784. New York, NY: Springer US, 2001.

[35] C. J. Roy, "Grid Convergence Error Analysis for Mixed-Order Numerical Schemes," *AIAA Journal*, vol. 41, no. 4, p. 595–604, 2003.

[36] G. B. Whitham, "A New Approach to Problems of Shock Dynamics Part 2. Three-Dimensional Problems," *Journal of Fluid Mechanics*, vol. 5, no. 3, p. 369–386, 1959.

[37] G. Whitham, *Shock Dynamics*, ch. 8, pp. 263–311. John Wiley Sons, Ltd, 2011.

[38] W. D. Henshaw, N. F. Smyth, and D. W. Schwendeman, "Numerical Shock Propagation using Geometrical Shock Dynamics," *Journal of Fluid Mechanics*, vol. 171, p. 519–545, 1986.

[39] D. W. Schwendeman and G. B. Whitham, "On Converging Shock Waves," *Proc. R. Soc. Lond.*, vol. 413, no. 1845, p. 297–311, 1987.

[40] D. W. Schwendeman, "On Converging Shock Waves of Spherical and Polyhedral form," *Journal of Fluid Mechanics*, vol. 454, p. 365–386, 2002.

[41] J. P. Best, "A Generalisation of the Theory of Geometrical Shock Dynamics," *Shock Waves*, vol. 1, no. 4, p. 251–273, 1991.

[42] J. Ridoux, N. Lardjane, L. Monasse, and F. Coulouvrat, "Comparison of Geometrical Shock Dynamics and Kinematic Models for Shock-Wave Propagation," *Shock Waves*, vol. 28, no. 2, p. 401–416, 2017.

[43] H. T. Huynh, "Accurate Monotone Cubic Interpolation," *SIAM Journal on Numerical Analysis*, vol. 30, no. 1, pp. 57–100, 1993.

[44] N. Peton and N. Lardjane, "An Immersed Boundary Method for Geometrical Shock Dynamics," *Journal of Computational Physics*, vol. 417, p. 109573, 05 2020.

[45] X. Yuan, J. Zhou, X. Mi, and H. D. Ng, "Numerical Study of Cellular Detonation Wave Reflection over a Cylindrical Concave Wedge," *Combustion and Flame*, vol. 202, p. 179–194, 2019.

[46] V. Soni, A. Hadjadj, A. Chaudhuri, and G. Ben-Dor, "Shock-Wave Reflections over Double-Concave Cylindrical Reflectors," *Journal of Fluid Mechanics*, vol. 813, p. 70–84, 2017.

[47] N. Brahmi, A. Hadjadj, V. Soni, and A. Chaudhuri, "Analysis of Shock-Wave Diffraction over Double Concave Cylindrical Wedges. Part I: Shock Dynamics," *Acta Astronautica*, vol. 172, pp. 134–139, 2020.

[48] O. Ram, M. Geva, and O. Sadot, "High Spatial and Temporal Resolution Study of Shock Wave Reflection over a Coupled Convex–Concave Cylindrical Surface," *Journal of Fluid Mechanics*, vol. 768, p. 219–239, 2015.

[49] I. T. Reshma, P. Vinoth, G. Rajesh, and G. Ben-Dor, "Propagation of a Planar Shock Wave along a Convex–Concave Ramp," *Journal of Fluid Mechanics*, vol. 924, 2021.

[50] I. V. Krassovskaya and M. K. Berezkina, "Mechanism of Formation of Reflection Configurations over Concave Surfaces," *Shock Waves*, vol. 27, no. 3, p. 431–439, 2016.

[51] S. M. Liang, C. S. Wu, F. M. Yu, and L. N. Wu, "Numerical Simulation of Shock Wave focusing over Parabolic Reflectors," *Shock Waves*, vol. 5, no. 3, p. 139–148, 1995.

[52] W. Shi and C. Cheung, "Performance Evaluation of Line Simplification Algorithms for Vector Generalization," *The Cartographic Journal*, vol. 43, no. 1, pp. 27–44, 2006.

[53] B. I. Kvasov, "Monotone and Convex Interpolation by Weighted Quadratic Splines," *Advances in Computational Mathematics*, vol. 40, no. 1, p. 91–116, 2013.